

ANDREW JOHN VASSILIOS GRIFFITHS

EXPLORING MBE GROWTH OF QUANTUM DOTS: LOW DENSITY GROWTH
FOR QUANTUM INFORMATION DEVICES.

UNIVERSITY OF SHEFFIELD

EXPLORING MBE GROWTH OF QUANTUM DOTS: LOW
DENSITY GROWTH FOR QUANTUM INFORMATION DEVICES.

ANDREW JOHN VASSILIOS GRIFFITHS



FOR THE AWARD OF DOCTOR OF PHILOSOPHY (PHD).
DEPARTMENT OF ELECTRONIC AND ELECTRICAL ENGINEERING,
UNIVERSITY OF SHEFFIELD.

DECEMBER 2014

Andrew John Vassilios Griffiths: *Exploring MBE Growth of Quantum Dots: Low Density Growth for Quantum Information Devices.*, PhD Thesis, © December 2014

⁴Love suffereth long, and is kind; love envieth not; love vaunteth not itself, is not puffed up, ⁵doth not behave itself unseemly, seeketh not its own, is not provoked, taketh not account of evil; ⁶rejoiceth not in unrighteousness, but rejoiceth with the truth; ⁷beareth all things, believeth all things, hopeth all things, endureth all things. ⁸Love never faileth: but whether there be prophecies, they shall be done away; whether there be tongues, they shall cease; whether there be knowledge, it shall be done away.

— 1 Corinthians 13: 4-8 (Revised Version)

Dedicated to my dear grandmother, Judith Harrison.

1933–2013

ABSTRACT

This thesis concerns the growth and subsequent application of InAs/GaAs quantum dots for novel research applications including entangled photon sources, and coupled quantum well/quantum dot devices.

This thesis gives an overview of quantum dot growth and tunable parameters of quantum dots (QDs), showing a review of prior work detailing their composition and properties. Special attention is given to wavelength tuning, and optimisation of the linewidth for a target application, including analysis of post-growth annealing.

Subsequent discussion focuses on low-density quantum dot samples, both in terms of growth and application. In conjunction with Cambridge University, micro-photoluminescence results of a short-wavelength QD sample are demonstrated, showing successful use of the rotation stop growth method, with further analysis and comparisons made with photoluminescence maps and atomic force microscopy. Analysis of long-wavelength (>1300nm at room temperature) QDs is also shown, with single dot work being performed on rotation-stop growth samples in analysis of Fine Structure Splitting (FSS) of individual QDs by Heriot Watt University. Results show an unexpectedly low FSS value for samples grown at the University of Sheffield, with potential for long wavelength entangled photon emitters. Growth optimisation of both the long- and short-wavelength structures is described, with optimisation required for the longer-wavelength samples, due to a comparative lack of cross-wafer QD density variation.

A novel adjustment to photoluminescence excitation is also discussed, with polarisation analysis being performed on QD samples designed for optical emission. Results indicate that QD properties have little to no effect on the spin retention in GaAs-capped QDs: instead surrounding material has a

larger effect, indicating that spin loss happens primarily between excitation and capture.

ACKNOWLEDGEMENTS

First and foremost, thanks must go to my family for their incredible support throughout everything I've done, a special mention to my grandmother who sadly is unable to see the completion of this degree; something she wanted to do. Hope this makes her proud! My parents, Lis and Neil Griffiths, have provided me with unwavering support and belief where I lacked it, giving me the strength to overcome any hurdle.

I'd like to thank the EPSRC for the student ship and the grant that enabled me to perform my work, and gain such valuable experience in the National Centre for III-V Technologies. Thanks also to Gavin Bell at the University of Warwick for aiding with AFM analysis; to Richard Phillips' group at Cambridge for their micro-PL analysis, and to Brian Gerardot and group at Heriot Watt (with a special mention to Luca Sapienza) for your FSS work. Without the indispensable Matthew Taylor and Peter Spencer from Imperial College, I would not have the fifth chapter of this thesis; a massive thank you to them and all at Imperial College for accommodating for a breakthrough two weeks.

A huge thank you to the people that I worked with- Edmund Clarke, without you I wouldn't have a degree, MBE experience, or in-depth knowledge of random football teams and bands! Thank you doesn't quite cover your invaluable insight and help. Thanks also to Peter Houston for your support academically and with the nitty-gritty of the PhD, your knowledge and insight have been indispensable. Richard Hogg deserves a special mention and huge thank you for 8 years of putting up with me and my pitfalls, both academically and alcoholically! Trips to Revolucion de Cuba and Menzels wouldn't have been quite so fun. A similar thanks to Dave Childs, Kenneth Kennedy, Ben Stevens, Nasser Babadazeh, Omar Ghazal, Saurabh Kumar and Richard Taylor for their support/sarcastic put downs throughout! A

huge thank you to Richard Frith for enduring the constant barrage of break-ages that I put him through, and also the random food packages that would mysteriously appear on my desk.

Last, but not least, a huge thank you to all of my friends that have kept me (almost) sane over the years. Alix Dietzel, you've been an inspiration and perpetual source of help, our meals, runs and random excursions have always been a pleasure. Charis Lestrangle, without you I wouldn't have been able to return to Sheffield, and since I did, you've been my rock, particularly when it came to caffeine consumption! Thanks also to Emily Thew, Nicola Laing and Kate Geller who have helped keep me sane over lunch/coffee breaks! This thanks section would be far far too long if I was to list everyone that has been there for me over the years, but although your name isn't here in print, your contribution to my life has still been invaluable to me. A special mention to SURLFC, who have kept me in a permanent state of injury for the past 6 years. You've made those years incredible. Back yourself.

CONTENTS

I	THESIS	1
1	INTRODUCTION	3
1.1	Background	3
1.2	Thesis Overview	6
1.3	References	8
2	PRACTICAL WORK	11
2.1	Molecular Beam Epitaxy (MBE)	11
2.1.1	Growth Apparatus	12
2.1.2	Pumping	13
2.1.3	Pressure Measurement	15
2.1.4	Substrate Heating and Temperature Measurement	16
2.1.5	Material Sources	17
2.1.6	The Growth Process	23
2.1.7	Growth Modes	29
2.1.8	RHEED Oscillations	30
2.1.9	Altering the Electrical Properties of a Grown Film	31
2.2	Semiconductor Characterisation	32
2.2.1	Photoluminescence Spectroscopy (PL)	32
2.2.2	Photoluminescence Excitation Spectroscopy (PLE)	34
2.2.3	Atomic Force Microscopy (AFM)	34
2.2.4	Doping Measurement	36
2.2.5	X-Ray Diffraction (XRD)	41
2.3	References	48
3	AN INTRODUCTION TO QUANTUM DOT GROWTH	51
3.1	Light Emission from Quantum Dots	53
3.1.1	Bimodality of quantum dot ensembles.	61
3.2	Quantum Dot Growth	64

3.2.1	Wavelength Control: Indium Coverage Control	64
3.2.2	Wavelength Control: Indium Flush	68
3.2.3	Wavelength Control: DWELL/InGaAs Capping	70
3.2.4	Wavelength Control: Post-Growth Annealing	71
3.3	Conclusion	83
3.4	References	84
4	LOW DENSITY QUANTUM DOT GROWTH	91
4.1	Rotation-Stop Growth Method	97
4.1.1	Short-Wavelength Rotation-Stop Quantum Dots	97
4.1.2	Long-Wavelength Rotation-Stop Quantum Dots	103
4.2	Applications for Low-Density Quantum Dots	105
4.2.1	Entangled Photon Sources at Telecoms Wavelengths	105
4.2.2	Fine Structure Splitting (FSS)	107
4.2.3	Minimising FSS at Telecom Wavelengths	109
4.3	Conclusion	113
4.4	References	114
5	SPIN POLARISED PLE ANALYSIS OF QUANTUM DOT OPTICAL SAMPLES	117
5.1	Experimental Setup	118
5.2	Theory	120
5.2.1	Selection Rules	120
5.2.2	Spin Loss Mechanisms	122
5.2.3	Analysis of the Spin PLE Plot	124
5.3	Practical Results	127
5.3.1	“Standard” QD Samples	128
5.3.2	Indium Coverage Samples	131
5.3.3	In-Flush QD Samples	136
5.3.4	Coupled QD/QW Samples	140
5.4	Conclusion	148
5.5	References	151
6	CONCLUSION	159
6.1	Further Work	161
II APPENDIX		163
A	APPENDIX: POLARISATION OF IN-FLUSH QDS	165

A.1 Conclusion 168

LIST OF PUBLICATIONS

1. **A J V Griffiths**, E M Clarke, J S Ng, C H Tan, Y L Goh, J P R David, P A Houston. *Growth and optimisation of 1300nm GaInNAs Avalanche Photodetectors*. COST Training School: Novel Gain Materials and Devices Based on III-V-N Compounds, April 2012.
2. **A J V Griffiths**, Z Zhang, E M Clarke, M Hugues, P A Houston *Growth and characterisation of quantum dots for single QD applications from 950-1300 nm*. UK Semiconductor Conference, July 2012.
3. **A J V Griffiths**. *Low-Density Quantum Dot Growth for Telecom-Wavelength Applications*. MBE Workers Party Meeting, March 2013.
4. **A J V Griffiths**, E M Clarke, M Hugues, P A Houston, R Parras, P Spencer, M Taylor, R Murray. *Spin dynamics during carrier capture in InAs/GaAs Quantum Dots and Coupled Nanostructures*. UK Semiconductor Conference, July 2013
5. L Sapienza, R N E Malein, C E Kuklewicz, P E Kremer, K Srinivasan, **A J V Griffiths**, E M Clarke, M Gong, R J Warburton, and B D Gerardot. *Exciton fine-structure splitting of telecom-wavelength single quantum dots: Statistics and external strain tuning*. Physical Review B, 88(15):155330, October 2013.
6. **A J V Griffiths**. *Spin dynamics during carrier capture in InAs/GaAs Quantum Dots and Coupled Nanostructures*. Yet to be published.

Part I

THESIS

INTRODUCTION

1.1 Background

III-V compound semiconductors have been an area of intense research since the first GaAs laser diodes were demonstrated in 1962[8–10, 18], with growth techniques paving the way for theoretical devices becoming a reality: Kroemer [16] theorised a number of solutions to inherent problems found in the first devices (namely extremely large threshold current density). His solution was that of a heterojunction laser, with different materials required to present a variation in band-gap throughout a grown device. This led to the invention of Liquid Phase Epitaxy (LPE) in 1963 at RCA Laboratories, a process that enabled easy growth of heterostructures, and yielding a number of successful results, including low-threshold, room-temperature, continuous-wave lasers at the end of the 1960s[1, 12, 19], a feat recognised by the award of the 2000 Nobel Prize for Alferov and Kroemer. However, the LPE technique had limitations- namely the materials to be deposited, the number of layers and the substrate size, and as a result, two alternative techniques emerged in 1968: MBE[3, 11, 21] and MOVPE[5], with both being used in tandem ever since. MBE is typically used more in research, with MOVPE being better suited to industrial applications.

These new techniques provided the option for more materials to be included in heterostructures, as well as finer layer control, and no theoretical upper limit on the number of layers to be grown. A number of authors in the early 1970s[2, 6] put forward the idea of the manipulation of carriers in semiconductors by creating structures comprised of very thin (\sim nm scale) layers of semiconductors with different band-gaps. It was proposed that these structures would confine carriers in the lower band-gap material,

creating a lower dimensional material, now described as “quantum wells” (QW).

Creating materials with decreased dimensionality is attractive as it alters the density of states (DOS), therefore altering the amount of energy required to populate the energy states in a given material. Bulk semiconductors have a density of states that is proportional to the square root of the energy, a two dimensional material (Quantum Well) has a density of states proportional to a constant, a one dimensional material (Quantum Wire) to the reciprocal square root, and a zero-dimensional material (Quantum Dot) provides an atomic-like discrete delta function representation of the density of states. This is represented in figure 1.1.1. This change in the density of states at each level of confinement provides increasing optical efficiency for each reduction in dimensional freedom.

Quantum wells are the easiest of the aforementioned structures to grow, needing an abrupt change in composition of the grown material. Provided the two materials grown have a differing band gap, and that the quantum well is thin enough (close to the de Broglie wavelength of a carrier), carriers will be confined. Quantum wires have no easy method of manufacture-patterned substrates or post-growth processing is required.

The initial purpose behind the concept of the quantum dot was that of improving existing quantum well lasers. Arakawa and Sakaki[7] proposed a laser that improved upon the aforementioned lasers, by reducing dimensionality to 0D in what they termed “Quantum Boxes”. The hypothesis was that the lower dimensionality of the material would lead to temperature invariance and a significantly lowered threshold current. The confinement in this initial paper was achieved by the application of magnetic fields on a QW sample. Since that experiment, the foremost source of 0D materials in GaAs-based solid state structures is from an exploitation of the Stranski-Krastanow (SK) growth mode when growing InAs on GaAs under particular conditions- known as quantum dots. Although improvements to lasers have been made through this discovery, the relative ease of growth of these quantum confining structures has led to an increase in applications for them. Foremost among the applications is that of quantum computing, due to the relative ease of optical addressing of the quantum dots, provided that the

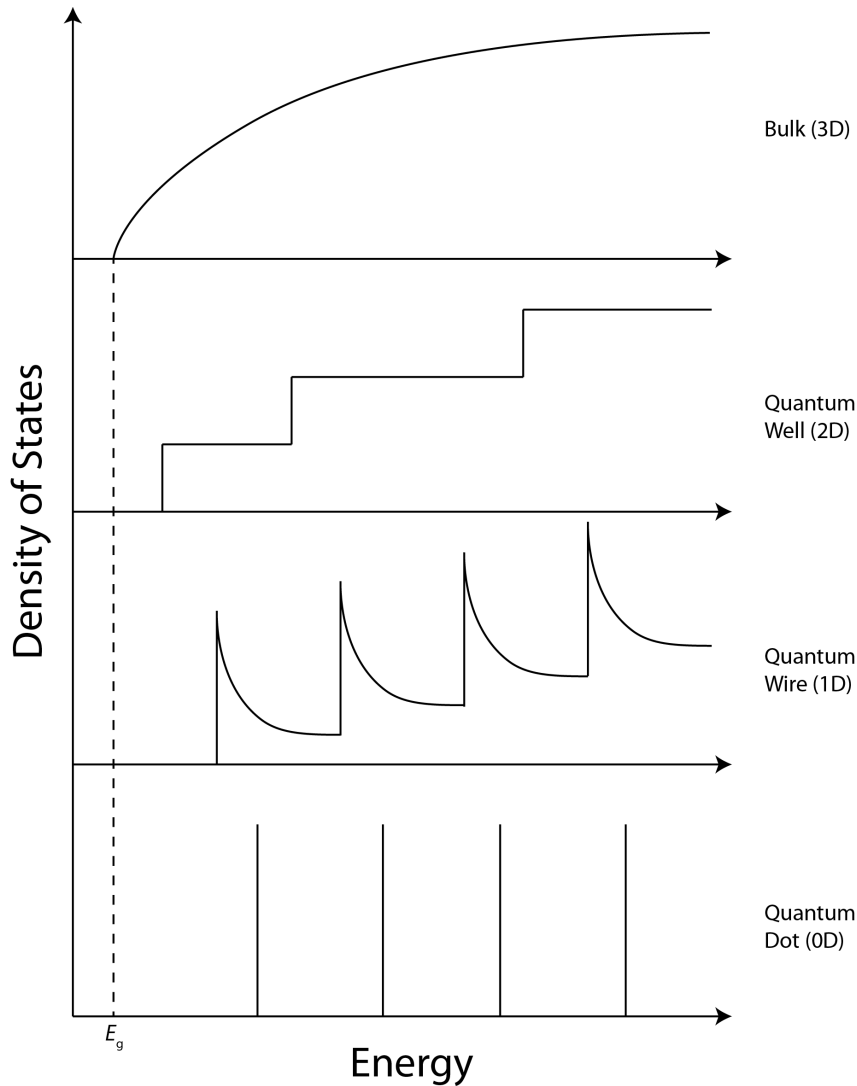


Figure 1.1.1: Representation of the density of states in confined systems (freedom of carriers given in brackets). Based on a figure from Mark Fox' book[13].

quantum dot density is low enough, a requirement of QD growth that is discussed in later chapters.

Current research on quantum dots is wide-ranging, with applications from medical research using colloidal quantum dots, to improving the efficiency of photovoltaics. This thesis looks at the complications of growth of low density quantum dots, with research of the grown material being of particular interest, as mentioned previously. The atomic-like spectra of individual quantum dots is ideal for single photon detectors and, by extension, entangled photon sources amongst other varying applications.

Using QDs for quantum information devices requires the manipulation of carriers and/or light from individual quantum dots. As such, the number

of quantum dots per unit area needs to be sufficiently low so that they can be spatially resolved. This requires fine tuning of the indium growth rate in the case of InAs/GaAs QDs, with the growth rate being the main factor in determining the density[20], with growth temperature also being crucial. When growing such samples, the density required is $\lesssim 1 \mu\text{m}^{-2}$, often meaning that the growth rate of $< 10^{-3}$ ML/s is needed[14]. At this deposition rate, the indium flux is not much higher than background measurement in an MBE reactor, meaning that precise repeatable growths are difficult. As a result, this thesis looks at methods of repeatable low-density growth methods.

Assuming the low density criteria has been met, a number of other requirements follow. The most important characteristic is usually the emission wavelength, determined by the physical size and composition of the QD and capping material. Variation in emission from InAs/GaAs QDs has been demonstrated from 900 nm to 1400 nm, with further demonstration in this thesis. The difficulty comes in fine tuning the emission characteristics such as the fine structure splitting (FSS), which is a requirement when using the biexciton-exciton cascade as a method for emitting entangled photons[4]. This thesis presents evidence of long-wavelength (< 1300 nm) quantum dots grown with FSS values suitably low enough for strain-tuning[15], contrary to previous assumptions which stated that increasing the wavelength of InAs/GaAs QDs with a strain-reducing layer led to an overall increase in the FSS[17]. Given that quantum information systems often look at the manipulation of the spin of carriers, the optimal environment for the reduction of spin loss in solid state structures is also required.

1.2 Thesis Overview

This thesis will discuss the optical properties of self-assembled InAs/GaAs quantum dots grown by MBE at the National Centre for III-V Technologies in Sheffield. The National Centre has been at the forefront of semiconductor growth research for a number of years, with its expansion incorporating three MBE reactors and three MOVPE reactors providing the country with high-quality bespoke samples, allowing the UK to benefit from world-

leading semiconductor research. The following work describes the growth and subsequent research on quantum dot structures in the centre, grown by MBE.

Chapter 2 describes the practical work performed in the remainder of the thesis, including the finer points of MBE, and also the characterisation performed on the samples grown. Chapter 3 describes QDs in greater detail, describing the methods of growth when trying to meet certain criteria, including wavelength of QD emission and QD density. Chapter 4 describes the methods undertaken to provide low-density quantum dot growth, and the effects seen in individual quantum dots when sufficiently low density is achieved. Chapter 5 describes the attempt to characterise spin loss in optical QD samples, incorporating a circularly polarised PLE experimental setup, with an attempt at describing the main factors that contribute to the loss of carrier spin in QD samples.

1.3 References

- [1] I. Hayashi, M. Panish, and P. Foy, "A low-threshold room-temperature injection laser," *IEEE Journal of Quantum Electronics*, vol. 5, pp. 211–212, Apr. 1969.
- [2] R. Dingle, W. Wiegman, and C. H. Henry, "Quantum States of Confined Carriers in Very Thin $\text{Al}_x\text{Ga}_{1-x}\text{As-GaAs-Al}_x\text{Ga}_{1-x}\text{As}$ Heterostructures," *Physical Review Letters*, vol. 33, no. 14, pp. 827–830, 1974.
- [3] A. Y. Cho and J. R. Arthur, "Molecular beam epitaxy," *Progress in Solid State Chemistry*, vol. 10, pp. 157–191, 1975.
- [4] O. Benson, C. Santori, M. Pelton, and Y. Yamamoto, "Regulated and entangled photons from a single quantum dot," *Physical Review Letters*, vol. 84, pp. 2513–2516, Feb. 2000.
- [5] R. D. Dupuis, "Metalorganic Chemical Vapor Deposition of III-V Semiconductors," *Science*, vol. 226, pp. 623–629, Nov. 1984.
- [6] L. Esaki and R. Tsu, "Superlattice and Negative Differential Conductivity in Semiconductors," *Ibm Journal of Research and Development*, vol. 14, no. 1, pp. 61–64, 1970.
- [7] Y. Arakawa and H. Sakaki, "Multidimensional Quantum Well Laser and Temperature-Dependence of Its Threshold Current," *Applied Physics Letters*, vol. 40, no. 11, pp. 939–941, 1982.
- [8] M. I. Nathan, W. P. Dumke, G. Burns, F. H. Dill, Jr, and G. Lasher, "Stimulated emission of radiation from GaAs p-n junctions," *Applied Physics Letters*, vol. 1, no. 3, pp. 62–64, 1962.
- [9] N. Holonyak, Jr and S. F. Bevacqua, "Coherent (visible) light emission from Ga ($\text{As}_{1-x}\text{P}_x$) junctions," *Applied Physics Letters*, vol. 1, no. 4, pp. 82–83, 1962.
- [10] T. M. Quist, R. H. Rediker, R. J. Keyes, and W. E. Krag, "SEMICONDUCTOR MASER OF GaAs," *Applied Physics . . .*, 1962.
- [11] A. Y. Cho, "Film Deposition by Molecular-Beam Techniques," *Journal of Vacuum Science & Technology*, vol. 8, no. 5, pp. S31–S34, 1971.

- [12] Z. I. Alferov, V. M. Andreev, E. L. Portnoi, and M. K. Trukan, "Alas-Gaas Heterojunction Injection Lasers with a Low Room-Temperature Threshold," *Soviet Physics Semiconductors-Ussr*, vol. 3, no. 9, pp. 1107–&, 1970.
- [13] M. Fox, *Optical Properties of Solids*. Oxford University Press, Mar. 2010.
- [14] B. Alloing, C. Zinoni, V. Zwiller, L. H. Li, C. Monat, M. Gobet, G. Buchs, A. Fiore, E. Pelucchi, and E. Kapon, "Growth and characterization of single quantum dots emitting at 1300 nm," *Applied Physics Letters*, vol. 86, no. 10, p. 101908, 2005.
- [15] L. Sapienza, R. N. E. Malein, C. E. Kuklewicz, P. E. Kremer, K. Srinivasan, A. Griffiths, E. M. Clarke, M. Gong, R. J. Warburton, and B. D. Gerardot, "Exciton fine-structure splitting of telecom-wavelength single quantum dots: Statistics and external strain tuning," *Physical Review B*, vol. 88, p. 155330, Oct. 2013.
- [16] H. Kroemer, "Theory of a Wide-Gap Emitter for Transistors," *Proceedings of the Institute of Radio Engineers*, vol. 45, no. 11, pp. 1535–1537, 1957.
- [17] E. Goldmann, S. Barthel, M. Florian, K. Schuh, and F. Jahnke, "Excitonic fine-structure splitting in telecom-wavelength InAs/GaAs quantum dots: Statistical distribution and height-dependence," *Applied Physics Letters*, vol. 103, no. 24, p. 242102, 2013.
- [18] R. N. Hall, R. O. Carlson, T. J. Soltys, G. E. Fenner, and J. D. Kingsley, "Coherent Light Emission From Gaas Junctions," *Physical Review Letters*, vol. 9, no. 9, pp. 366–&, 1962.
- [19] Z. I. Alferov, "The Nobel Prize in Physics 2000 Zhores I. Alferov, Herbert Kroemer, Jack S. Kilby,"
- [20] P. B. Joyce, T. J. Krzyzewski, G. R. Bell, T. S. Jones, S. Malik, D. Childs, and R. Murray, "Effect of growth rate on the size, composition, and optical properties of InAs/GaAs quantum dots grown by molecular-beam epitaxy," *Physical Review B*, vol. 62, no. 16, pp. 10891–10895, 2000.

- [21] J. R. Arthur, "Interaction of Ga and As₂ Molecular Beams with GaAs Surfaces," *Journal of Applied Physics*, vol. 39, no. 8, pp. 4032-4038, 1968.

PRACTICAL WORK

This chapter will give an overview of the practical methods used over the course of this PhD, focusing on III-V crystal growth by MBE as the most prominent aspect, followed by characterisation of the grown material.

2.1 Molecular Beam Epitaxy (MBE)

Epitaxy is a form of crystal growth that relies on the underlying substrate to form a template for the continued material deposition, which enables the growth of structures that remain in a uniform crystalline state for optimal electrical and optical properties.

The advantages of using MBE for epitaxy over alternative methods of semiconductor growth include:

- Low, controllable growth rate enabling compositional or dopant changes to be made on a sub-nanometre scale.
- Compared with CVD, MOVPE etc., growth temperature is low ($< 650^\circ\text{C}$ for GaAs).
- The Ultra-High Vacuum (UHV) environment allows diagnostic techniques to be performed in-situ, such as surface analysis by RHEED¹.
- Sequential deposition can also be done in-situ.
- Ultra-high purity material growth can be achieved.
- Provision of source material is independent of substrate temperature, as opposed to MOVPE where the substrate temperature influences

¹ UHV is characterised as being a pressure less than 10^{-9} mbar

metal-organic compound cracking. This allows for a much wider substrate temperature operating range.

The vast majority of growth undertaken for this degree was III-As based, using predominantly GaAs (100) substrates. It therefore follows that the best example of III-V growth to use is GaAs, particularly as, barring slightly more exotic alloys, the majority of III-V MBE follows similar patterns.

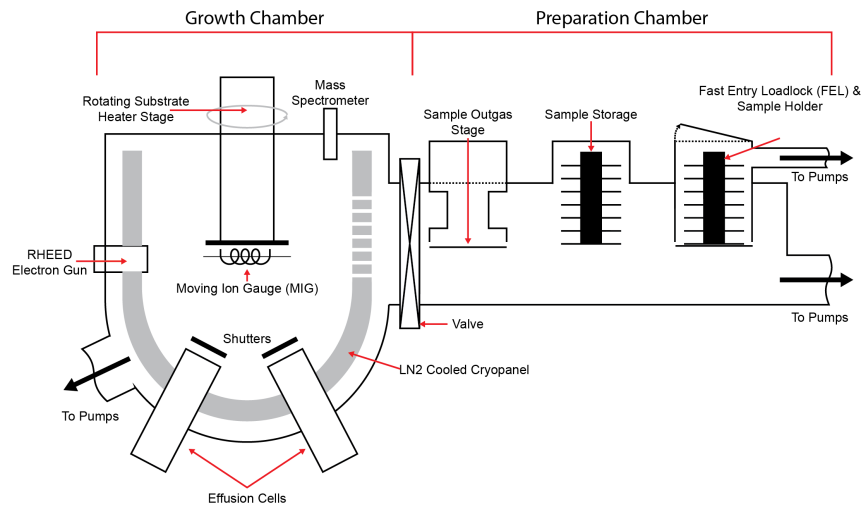


Figure 2.1.1: Basic schematic of a typical MBE reactor including sample preparation and loadlock.

2.1.1 Growth Apparatus

The reactors used for growth over the course of this PhD were based in the EPSRC National Centre for III-V Technologies, each manufactured by VG Semicon, with two V90 series reactors, and one V80 series reactor. All three reactors follow the overall basic schematic shown in figure 2.1.1, the main differences between each reactor are listed in table 2.1.1:

The V90 series of reactor is designed as a low-level production reactor and is larger in size and capacity compared to the smaller V80-series, which is designed for research and development. All reactors are primarily solid source, although “solid source” is something of a misnomer, with a number of the materials requiring temperatures hot enough to melt/sublime in order to provide a molecular flux. Nitrogen is the exception to this rule, with

	V80	V90-1	V90-2
Group III Cells	Gallium, Aluminium, Indium	Gallium (2), Aluminium (2), Indium (2)	Gallium (2), Aluminium, Indium
Group V Cells	Arsenic, Antimony, Bismuth, Nitrogen (Plasma Source)	Arsenic, Phosphorus	Arsenic, Antimony, Nitrogen (Plasma Source)
Dopant Cells	Silicon, Beryllium	Silicon, Beryllium	Silicon, Beryllium, Tellurium
Sample Manipulation	Manual	Automatic, Batch Processing	Automatic, Batch Processing
Max. Sample Size	2-Inch	4-Inch/3x 2-Inch	4-Inch/3x 2-Inch

Table 2.1.1: An overview of the MBE reactors in the NC in Sheffield. This table shows the materials and sample handling capabilities.

the N_2 gas being converted to a plasma for monatomic nitrogen incorporation into dilute nitride films (see section 2.1.5).

In order for the reactors to reach and maintain UHV, specialist materials and pumps are required. Materials that readily oxidise are avoided due to the surface area roughening and presenting a larger surface area for the adsorption of unwanted materials. In this vein, stainless steel is typically used for the bulk of the construction. In order to further avoid the increase of surface area, threaded surfaces are only located externally, copper gaskets are used to keep a simple seam between components, glues are typically not used, and different soldering and welding techniques are required, with welding potentially forming unwanted gas pockets.

2.1.2 Pumping

A variety of pumps are used for MBE, both for different applications and as a failsafe in case an individual pump fails, with four different pumps employed on the reactors used in the NC as follows:

2.1.2.1 Turbomolecular Pump (TMP)

This pump is often operated with a backing rotary-vane or diaphragm pump to provide forepumping. It is comprised of rotor/stator pairs mounted in series, similar in structure to a turbine. The backing pump is required as

the mean free path of molecules at atmospheric pressure (approximately 70 nm) is far too low for the blades of the TMP to clear, causing it to stall. The rotor/stator pairs operate at very high speed (up to 50 000 rpm), applying kinetic energy to gas molecules in the chamber, forcing their exit into an exhaust. Heavier molecules are more readily pumped with this method, Magnetic bearings are used to avoid the use of oil, and to minimise friction during operation. A TMP can provide a vacuum up to 10^{-10} mbar, and is typically employed to evacuate the loadlock and provide a background pressure in both the growth chamber and preparation chamber.

2.1.2.2 *Ion Pump*

This pump will only work with an existing vacuum (typically $< 10^{-6}$ mbar), usually provided by the TMP. The operation of an ion pump is based on the application of a strong electric potential (up to 7 kV), which ionises gases present in the chamber using clouds of electrons within Penning cells, and accelerates them into a solid chemically active cathode, pumping the ions from the chamber by chemisorption, or, for lighter and inert gases, physisorption. The rate of pumping depends on the molecules being pumped from the cell and the material of the cathode. The benefit of such a pump is that there are no moving parts and therefore it requires no oil, creates no vibration and is relatively low maintenance. An ion pump can attain a pressure approaching 10^{-11} mbar, and is used to maintain the base pressure in both the preparation and growth chambers.

2.1.2.3 *Cryopump*

There are two different types of cryopump employed on each of the machines, one in close proximity to the substrate manipulation stage in the growth chamber (referred to as the cryoshroud or cryopanel) and the other as an external pump similar to that of the ion pump or TMP. Both work on the principle of condensing gases and vapours on a cryogenically cooled surface, where they reside until the pump is regenerated. For lighter gases, such as hydrogen, a different mechanism called cryotrapping comes into play, whereupon a gas molecule's residence time on the surface of the pump is significantly increased due to the reduced temperature, removing it, al-

be temporarily, from the chamber. The external cryopumps employed in the NC are kept on a closed loop helium compressor, with the temperature of the pump reaching 10 K. The cryopanel is on a separate loop providing liquid nitrogen as the cryogenic coolant due to the larger physical size of the area to be cooled, typically approaching 77 K. Cryopanel is used as a form of secondary pumping in the near vicinity of the substrate in order to reduce unwanted impurities being incorporated into the grown crystal, also preventing build up of source elements.

2.1.2.4 Titanium Sublimation Pump (TSP)

This pump is used primarily after the vacuum chamber has been exposed to air, or a particularly reactive material, and is employed only when the chamber is already at a vacuum. It operates by subliming Ti from a filament, which coats the chamber walls and getters reactive molecules from within the chamber (both preparation and growth chamber). This pump is periodically used and cannot be used during growth as the Ti would incorporate into a growing film, causing unwanted contamination.

2.1.3 Pressure Measurement

In order to ensure a stable operating environment within the growth chamber, vacuum gauges are needed to monitor the pressure. A number of gauges are required to do this, especially when measuring the system at low vacuum during pumping/venting.

2.1.3.1 Atmosphere to Low Vacuum

In order to measure pressure close to atmosphere, a number of gauges can be used, including the baratron, which uses the changing capacitance of metal plates in close proximity, and cannot measure pressures much below 1 torr (≈ 1.3 mbar). A pirani gauge measures from around 0.5 mbar to 10^{-4} mbar by measuring the cooling of a heated filament due to any surrounding gas: If there is more gas surrounding the filament, there is more chance that a gas molecule will collide with it, thus slightly cooling it. The resistance of the wire is measured due to the change of resistance when a

wire is heated, or the wire is kept at a constant temperature and the amount of current is varied, both of which can give a pressure readout.

2.1.3.2 *Low to High Vacuum*

At $\sim 10^{-2}$ mbar and below, the most suitable gauge is a Penning gauge, or cold cathode gauge, which uses electric and magnetic fields to create a DC discharge between two electrodes. The DC discharge relies on the ionised gas to provide the current: as the pressure falls, so does the available gas which can provide current. Measuring this current provides a pressure reading. A Penning gauge has a range of 10^{-2} mbar to 10^{-8} mbar, but is reliant on the knowledge of the gas that it is measuring. For lower pressures, a hot-filament ion gauge is used. This works by creating an electron current from a heated element, which is attracted to a helical grid which is positively biased- typically at around 150 V. En route to the grid, the electrons encounter, and ionise, atoms in their path. These ions are then attracted to a negatively biased collector. This causes a current to be generated in the collector, which can then be given as a pressure. The limits of this gauge are 10^{-4} mbar to 10^{-11} mbar.

The hot filament gauge can also be used as a measure for material flux; it is positioned between the substrate and the beam sources, and the shutter of the material to be measured is opened. The measurement of the current is directly proportional to the beam equivalent pressure (BEP), which can then be used to determine the growth rate of a particular substance. This gauge is known as the Movable Ion Gauge, or “MIG”.

2.1.4 *Substrate Heating and Temperature Measurement*

Substrate heating is undertaken on the aforementioned VG machines by an element made from a refractory metal, which is situated behind the substrate. The basic principle behind heating the substrate in this manner is that of black body radiation, governed by the Stefan-Boltzmann law. This law allows the power emitted from a black body to be expressed in terms of its temperature:

$$\frac{P}{A} = \sigma T^4 \quad (2.1.1)$$

Where P is the net radiated power, A is the radiative area, σ is Stefan's constant ($5.6703 \times 10^{-8} \text{ W m}^{-2} \text{ K}^{-4}$) and T is the temperature in Kelvin. Rearranged, this can be used to find the substrate temperature, assuming the heater temperature is known (in an ideal situation).

$$\begin{aligned}\sigma(T_H^4 - T_S^4) &= \sigma T_S^4 \\ T_H^4 &= 2T_S^4 \\ \frac{1}{2}T_H^4 &= T_S^4 \\ \frac{1}{\sqrt[4]{2}}T_H &= T_S\end{aligned}$$

The measurement of the substrate temperature is a contentious issue, particularly within growth literature, not least because of the variety of measurement equipment, and the inherent inaccuracies of each of them. The machines in the NC are equipped with a thermocouple positioned behind the substrate. Due to its position, it more closely measures the temperature of the heating element rather than the substrate itself, therefore the value attained is used as a reference for a particular machine. Typically, RHEED (section 2.1.6.2) and foreknowledge of the temperature-based surface change is used to calibrate the thermocouple reading. Any growth temperatures listed hereafter refer to the thermocouple temperature of the machine being used.

2.1.5 *Material Sources*

For solid-source MBE, effusion cells are used to provide a molecular flux. In order to create this flux, the elemental source material is heated so that the condensed phase of material is kept at equilibrium with the vapour phase, and the evaporation process at high vacuum is exploited by means of an aperture into the growth chamber, and given freedom in one direction only towards the substrate. This evaporation process is known as Knudsen effusion, although in order to provide practical growth rates and coverage across an entire wafer, the aperture into the chamber is rather larger than it would be for ideal Knudsen effusion. The flux emitted is primarily controlled by the temperature of the respective cell, which are designed with

precise temperature control in mind. A typical effusion cell (Figure 2.1.2) comprises a crucible that is chemically inert and able to withstand high temperatures (e.g. pyrolytic boron nitride (pBN)), and is heated by a refractory metal element (usually tantalum or tungsten), with the feedback for temperature control being provided by a thermocouple, often made of a refractory tungsten-rhenium alloy.

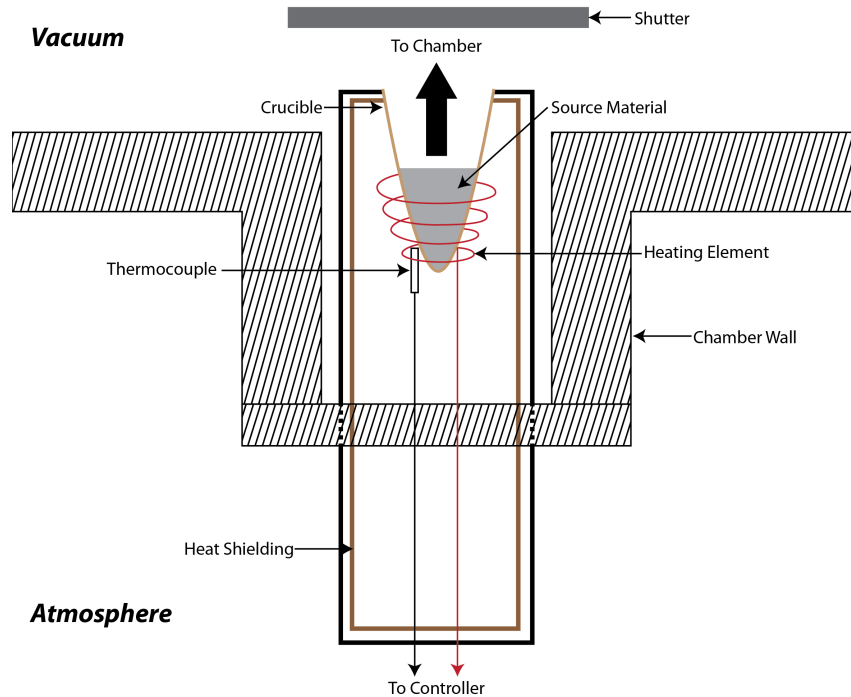


Figure 2.1.2: Basic Schematic of an Effusion Cell as it would be fitted on an MBE reactor

2.1.5.1 Group III Sources

Table 2.1.1 refers to the different cells on the machines in the NC, with the group III elements being similar across the range, albeit with different quantities on each reactor. Each of the materials' cells needs to operate at a significantly higher temperature than their respective melting points (table 2.1.2) to provide a flux that yields a significant enough growth rate (usually $> 0.5 \text{ ML/s}$).

	Gallium	Indium	Aluminium
Melting Point (At atmosphere)	29.8 °C	156.6 °C	660.3 °C
Rest Temperature	400 °C	400 °C	850 °C
Typical Operating Temperature	> 800 °C	> 700 °C	> 1000 °C

Table 2.1.2: Properties of group III materials used on the NC MBE reactors.

The liquid nature of the sources provides unique problems in each case. Molten aluminium has a tendency to “creep” up the sidewalls of a pBN crucible, wetting the surface and the crystal planes of the material via capillary action. The edge of an aluminium crucible needs to be kept cool to stop the molten material from exiting the cell and potentially causing damage within the chamber or cell, particularly the heating element of the cell. The difference in the thermal expansion rates of pBN and Al creates a secondary problem from the wetting process, as rapid cooling can cause the pBN crucible to break. This is prevented, or at least mitigated by controlled slow cooling of an Al cell, with the crucibles being changed after a cooling process, unless the cell is empty. Another method of averting this problem is to have a double-walled crucible so the internal pBN wall is damaged in place of the full crucible.

Gallium and indium suffer from uneven heating in a basic effusion cell, with a large aperture leading to heat loss, and in the worst cases, causing unpredictable re-condensation of material which leads to liquid spitting at the substrate. This is countered by either increasing the number of turns of the heater element, or to provide a separate heating element at the chamber end of the crucible, which ensures a more controllable heating of the material- these cells are known as “hot-tip” cells.

Gallium presents a further problem due to a reduction in density when freezing, meaning that the solid material expands compared to the melt. This is a particular problem as the top of the molten material will cool first, limiting the space of the underlying material, meaning that further cooling will potentially crack the crucible, although the relatively low melting point of gallium means that the material can be kept as a liquid, above 30 °C (usually 50 °C).

2.1.5.2 Group V Sources

This thesis primarily deals with arsenide-based growth, although a small amount of phosphides and dilute-nitrides were grown. As such, the operation of the bismuth and antimony sources will not be discussed in this thesis, despite being present on the reactors. Arsenic does not have a melting point below a vapour pressure of ~ 36 bar, instead subliming at 614°C at standard atmospheric pressure, although the operating temperature of arsenic in an MBE system is lower again (due to the reduced vapour pressure) at temperatures ranging from 300°C to 450°C . At this temperature, the arsenic vapour is a tetramer, As_4 , which is largely unsuitable for the III-V growth performed in this thesis, and, in particular, devices that require high electron mobilities[14]. The temperature required to evaporate As_2 instead of As_4 also produces a flux that is far in excess of that required for stoichiometric growth for typical MBE growth rates ($< 2\text{ML/s}$), with the increased evaporation rate also reducing the lifetime of the arsenic charge, which would ideally last in excess of a year. As a result, a two-stage dissociation or “cracker” cell is used, with the arsenic charge being held in a crucible in a similar manner to the group III materials, and the aperture of the crucible leading to a second heating stage that is kept at a temperature that is sufficient to “crack” the As_4 tetramers to As_2 (Figure 2.1.3). Large charges are typically used ($> 350\text{g}$), meaning that any change in the temperature of the bulk material is inefficient. As a result, the bulk arsenic is not returned to a rest temperature like the group III source materials, but remains at operating temperature, with the outgoing flux being controlled by a needle valve, providing a repeatable value that is easily varied over the course of a growth run.

Phosphorous behaves in a similar manner to arsenic in its evaporation into the chamber- P_4 is converted to P_2 using a cracker cell, but with an additional complication. High-purity phosphorus is only commercially available in significant quantities in the red allotrope, with the best allotrope for growth being white phosphorus. Most phosphorus cells provide in-situ conversion, with two “zones” for each allotrope. Red phosphorus is converted by heating the red zone and allowing the evaporated material to condense in the white zone, forming a charge of white phosphorus, ready for growth.

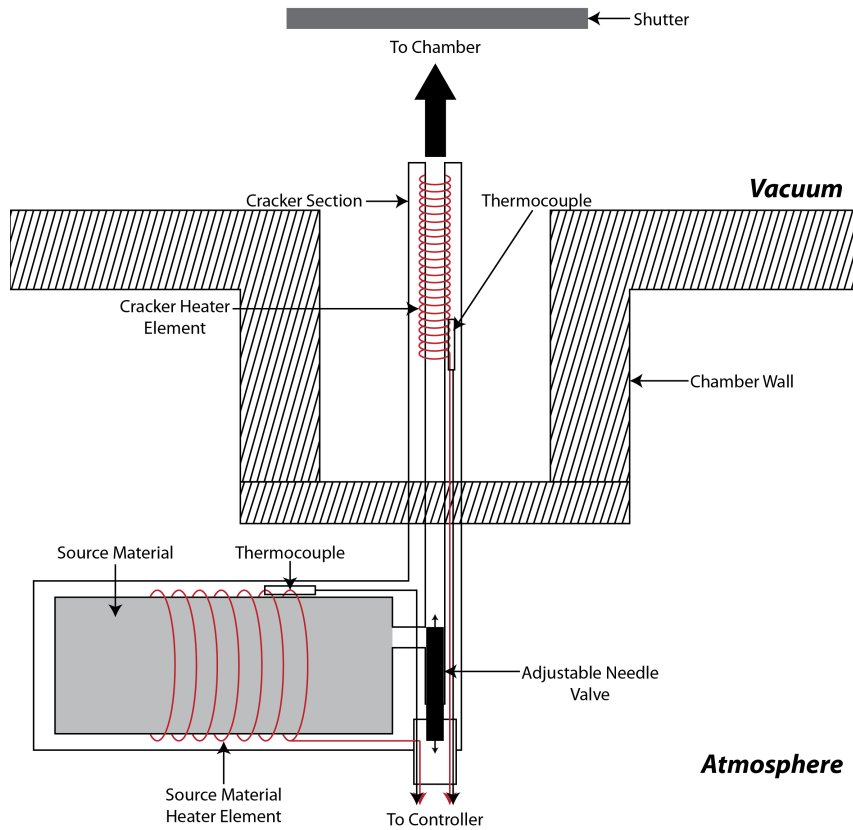


Figure 2.1.3: Basic Schematic of a Cracker Cell as used on an MBE reactor

This process can be reversed in the event that a phosphorus charge is not fully depleted and an MBE system requires venting. Phosphorus recovery is necessary when venting a reactor, as white phosphorus is highly reactive in an oxygen atmosphere, pyrophoricity creating a fire risk. Phosphorus recovery systems are integrated into the growth system, ensuring any lingering phosphorus is either pumped away safely, isolated or reacted with safely. The NC has the option for easy pumping of excess phosphorus thanks to the MOVPE systems in the growth laboratory, which enables safe evacuation of hazardous waste materials.

An alternative to a pure phosphorus cell is using gallium phosphide, although the cost of the source material is considerably higher, and the presence of a possible background Ga flux reduces the range of potential growth materials, meaning the GaP source is less desirable.

Nitrogen provides a unique set of problems in III-V MBE- the introduction of a gas into a vacuum chamber being the most fundamental, although

this is mitigated with the use of high-precision mass flow controllers (MFC) and efficient pumping. The unreactive nature of the N_2 molecule, and the strength of the bonds between the nitrogen atoms within that molecule is another hurdle to overcome. In this case, an RF plasma source is used to solve this problem. The nitrogen plasma cell contains a coil that surrounds an antechamber (to the growth chamber), which is excited by RF energy. As the RF energy excites the N_2 supply, the gas begins to break down and ionise, eventually reaching a stable state of electrons, N^+ ions and monatomic nitrogen. The cell is purpose built to ensure that the ions emitted toward the substrate are minimised compared to the atomic nitrogen being released, as the high-energy ions can damage the substrate and growing film. The material grown for this thesis only uses this technique for dilute nitride materials, i.e. films that contain less than 5% nitrogen as a group V element.

The flux emitted from a nitrogen plasma cell is not measured by the MIG due to the significant change in pressure after the introduction of the nitrogen gas (typically up to 6 orders of magnitude pressure change). Instead an optical power meter is used to determine the brightness of the plasma, which is dependent on the gas flow rate and RF power used to excite the gas into a plasma state. Nitrogen incorporation is dependent on the bulk crystal growth rate: in order to ascertain the amount of nitrogen incorporated into a grown film (for simplicity's sake, let's use GaAs, with the grown film being GaN_xAs_{1-x}), the best method is to use post-growth characterisation techniques, particularly XRD (section 2.2.5).

Prior to GaN_xAs_{1-x} growth, the nitrogen cell must be calibrated, ascertaining the flow rate and RF power at which the plasma can be struck and remain stable, with the optical power being the measurement taken to quantify any change in the plasma. Figure 2.1.4 shows the nitrogen plasma cell calibration, with the variation of optical output plotted against the nitrogen gas flow rate- the flow listed is the percentage of a 1 sccm mass flow controller (MFC). The flow was varied at each power listed, with 0.1 sccm (10%) being the optimal flow rate.

Assuming the Ga growth rate is known, with optimised As flux, prior to the GaN_xAs_{1-x} growth, the optimal N_2 flow for the plasma is ascertained first, and an RF power is chosen based on the desire for high or low nitrogen

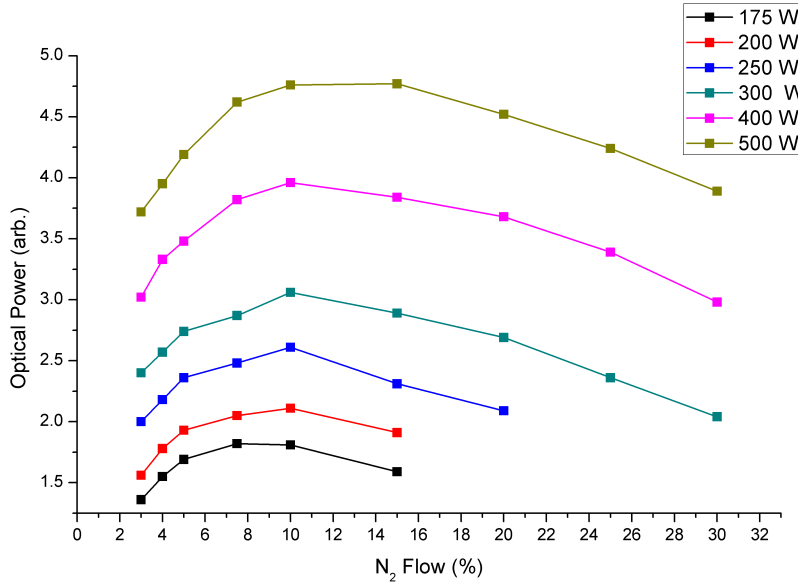


Figure 2.1.4: Example of data used for nitrogen cell calibration, looking at optical power vs. N₂ flow.

content. With this in mind, a range of samples are grown, usually varying one parameter until either the desired composition is achieved or the limits of the parameter in question are met.

2.1.6 The Growth Process

Practical results and all growth performed for this thesis were based on GaAs (100) substrates. For future growth description, GaAs will be the material used, unless otherwise specified, corresponding to Ga being described as the group III element, and As as the group V element.

2.1.6.1 Sample and Growth Preparation

Thanks to improved semiconductor wafer production, sample preparation now takes place almost entirely in the MBE reactor, and can be automated. This is largely due to “epiready” substrates, which provide a near-atomically flat surface and that only the native oxide remains on the surface of the wafer. These epiready wafers only require two heating processes before growth can commence, the first of which ensures adsorbed materials such as water vapour are removed prior to the introduction of the sample to the growth chamber, to avoid potential contamination. This process heats the

sample to a temperature above 200 °C (usually > 350 °C), on the out-gas stage in the preparation chamber (figure 2.1.1).

Epitaxy requires the underlying substrate's crystalline structure to provide a foundation for subsequent growth, meaning that the native oxide that naturally forms on the surface of a wafer must be removed. This process is usually done immediately prior to growth, and uses the substrate heater stage in the growth chamber due to the preferential desorption of arsenic from the substrate. In GaAs (100) substrates, this preferential desorption occurs at a similar temperature to that of the oxide desorption (585 °C ± 10 °C [9]), and therefore requires an overpressure of arsenic when operating above this temperature.

Prior to a growth run, the growth rates of the source materials need to be ascertained, measured by placing the movable ion gauge (MIG) in the path of the material flux. Upon opening the shutter of a desired source material, the current read out from the MIG changes in proportion to the rate of flux effusion from the respective cell. Unfortunately, due to the difference in chamber geometry from system to system, the difference in ion gauges/-controllers as well as the variation between the materials used, there isn't a hard and fast current-to-growth-rate conversion, although for individual cells and chambers, there is a relationship between the flux measured by this method, and the growth rate. Provided this relationship is known, the effusion cell in question (i.e. Ga) is adjusted in temperature until the desired flux is attained, after which the group V (i.e. As) flux is measured, although the bulk temperature is kept constant during a growth run, the valve position is adjusted to change the As flux.

The ion gauge itself measures the density of the surrounding atoms, with its sensitivity being described as follows:

$$S = 0.038N + 0.468 \quad (2.1.2)$$

Where N is the atomic number. As can be seen, the larger the atom being measured, the more sensitive the ion gauge: in particular, the more current is generated the larger the molecule/atom being measured by the ion gauge. The ion gauge's sensitivity can also be affected by a build up of growth on the instrument itself.

2.1.6.2 Growth

III-V growth is dictated by the group III element's flux; an excess or dearth of the group V element results in a film that is grown at the same rate, but is respectively rich or deficient in the group V element. In GaAs, one can determine the correct III:V ratio by means of the in-situ measuring technique known as Reflection High Energy Electron Diffraction (RHEED). This technique provides real-time analysis of the surface structure of the substrate/grown film by firing a high-energy electron beam at a glancing angle of the substrate ($< 5^\circ$), penetrating the surface layer of atoms of the sample, thus allowing diffraction of the electrons through the crystalline structure, the electrons then collide with a phosphor-coated screen, providing a visual representation of the surface structure through the constructive/destructive interference patterns. The energy of atoms on the surface of a sample determine the manner in which they are arranged, as well as the crystal orientation and the manner in which the crystal has been prepared.

A surface is essentially the abrupt termination of a stable periodic structure, and the lack of completion of a lattice results in the surface atoms having "dangling bonds"; where a bond is represented by two spin-paired electrons, and the dangling bond contains less than two. If the surface were to remain directly comparable to the bulk crystal, the free energy of the system would not be at a minimum[13], and as a result the surface atoms rearrange themselves to form new bonds (As-As and Ga-Ga) that would normally be unfavourable. This results in a periodic surface reconstruction which is temperature, and particularly in the case of polar materials like GaAs, orientation based. Assuming a GaAs substrate that has an arsenic-stabilised surface of (001) orientation and is kept at a suitable arsenic overpressure, the reconstruction would be (2×4) at growth temperature (post-oxide removal). If we introduce gallium and commence growth at the appropriate temperature, the reconstruction should remain (2×4) if there is a sufficient arsenic flux. To determine a precise 1:1 As:Ga ratio, it is necessary to determine the point at which the arsenic flux is low enough so that the surface reconstruction changes to a (4×2) pattern- this represents the 1:1 As:Ga flux ratio. Assuming prior knowledge of the arsenic flux at this point, it is

necessary to increase the ratio of As:Ga to 1.6:1 to maintain good quality growth for the purposes of optical devices[14].

Below 650 °C, the sticking coefficient of Ga approaches 1, however, the sticking coefficient of As is close to zero without a Ga adatom present at temperatures above 300 °C. For this reason, the Ga flux dictates the growth rate. In a typical (and idealised) situation, a Ga atom reaches the substrate and adsorbs and desorbs from various sites until reacting with impinging As molecules, leading to stoichiometric growth, as excess As atoms are desorbed. This holds until the temperature known as the congruent evaporation temperature, at which the kinetic energy of the reactant Ga atom is too high, meaning the rest time of the Ga on the substrate surface is too short and reducing the sticking coefficient to much lower than 1, typically above 625 °C[3].

Substrates used in MBE are not perfectly atomically flat. As a result there are many atomic step edges across a substrates surface. These step edges provide sites of low potential, meaning that the impinging adatoms are more likely to remain. Layers of growth are formed by these step edges extending perpendicular to the growth plane, completing an individual layer when the step edges overlap, known as step-edge propagation.

2.1.6.3 *Homoepitaxy*

Growth itself can be split into two simple sub-sections, homoepitaxy and heteroepitaxy. The former refers to crystal growth whereupon the grown epilayer is identical to the substrate, e.g. GaAs grown on GaAs. Heteroepitaxy is the opposite, that is the growth of a material that differs from the substrate e.g. AlAs on GaAs, InGaAs on GaAs etc.. III-V homoepitaxy can be idealised to a degree as 2D growth as described above, with no considerations needed for strain or other such difficulties due to the matching epilayer and substrate.

2.1.6.4 *Heteroepitaxy*

The main consideration when attempting heteroepitaxy is the difference between crystal lattice constants, the lattice constant being the dimension of the unit cell of a crystalline material. The difference between the lattice

constant of a grown layer (epilayer) and substrate can greatly influence the quality of growth, and in some cases the electronic properties of a grown structure. Epitaxial growth is based on the underlying substrate; the grown layer fits itself to the crystalline structure it is growing upon (figure 2.1.5). If there is a significant difference between the epilayer and substrate lattice constants, mechanical strain will build up due to compression or tension of the crystal, leading to a build-up of energy that reaches a critical point after prolonged growth at which the grown crystal deforms. These deformations are known as “dislocations” and are dependent on the type of material grown, with the critical thickness being dependent on the lattice mismatch and Young’s modulus of the grown material. This critical thickness is important when considering the growth of semiconductor devices, as crystal dislocations cause unwanted effects, particularly in optical devices. Figure 2.1.5 shows a basic schematic of heteroepitaxy, with the squares representing a 2D approximation of a unit cell, and the effects of strain being exaggerated for each case. Tensile strain causes a material to stretch itself to accommodate the underlying material, resulting in the unit cell being stretched perpendicular to growth and compressed in the direction of growth, whereas compressive strain is the opposite case, with extension in the direction of growth and compression perpendicular to growth.

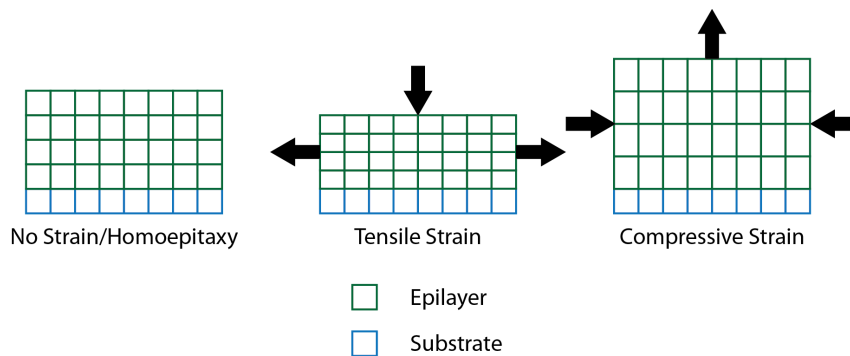


Figure 2.1.5: Demonstration of the effect of strain on a pseudomorphic crystal lattice in heteroepitaxial growth

In order to grow a binary substance that differs from the substrate, the process is much the same as described for GaAs growth, albeit with potential problems arising with lattice mismatch and strain release. In essence, the group III material dictates the growth rate, and the group V material is in excess. It becomes only slightly more complex when growing a ter-

tiary or quaternary substance such as $\text{In}_{1-x}\text{Ga}_x\text{As}$ or $\text{In}_{1-x}\text{Ga}_x\text{As}_y\text{P}_{1-y}$ where x and y refer to the proportion of the element suffixed. Mixed group V compounds cause further complications due to exchange reactions, and preferential incorporation. The energetic preference of group V termination of a crystal interface (in a superlattice for example) may also present a problem. This thesis does not deal with mixed group V compounds, excepting dilute nitrides, and as such, the growth process of mixed group Vs will not be discussed.

Using $\text{Al}_{1-x}\text{Ga}_x\text{As}$ as an example, the group III and group V elements are once again considered separately in terms of their composition, but the growth rate of each of the group III elements must be combined, with the ratio of the two growth rates on a given substrate conveniently being the ratio of the compound itself (for a typical III-V semiconductor) e.g. for an $\text{Al}_{0.25}\text{Ga}_{0.75}\text{As}$ compound, the growth rate could be 0.25 \AA/s and 0.75 \AA/s for Al and Ga respectively. The group V's flux is adjusted to accommodate the total group III growth rate accordingly.

AlGaAs is a convenient compound when growing on GaAs due to the similarity between the lattice constants of AlAs and GaAs, and the fact that the two materials can be grown at similar temperatures. Other compounds, such as InGaAs, require a different growth temperature due to the different behaviour of the adatoms, with the large lattice mismatch also adding potential problems for the indium-containing arsenide compounds on GaAs.

Heteroepitaxy is used to take advantage of the interaction between different materials in a crystalline structure. More often than not, the structures require abrupt interfaces, and MBE is particularly suited to achieve this task, thanks to precise growth rate control, as well as shuttered material sources. Typically, MBE growth rates are less than 1 ML/s . As the time for a shutter to open or close is much less than a second, crystals can be grown to sub-monolayer precision.

2.1.7 Growth Modes

As well as dislocations, strain caused by lattice mismatch can cause different types of growth, as described by Ernst Bauer[2]. The three types identified are described as follows:

2.1.7.1 Frank-van der Merwe (FM) Growth[6]

FM growth is 2D, layer-by-layer growth, often the ideal growth type for most semiconductor devices (provided that the grown crystal contains a lack of dislocations), as often only a 2D layer design is required. This growth is attained by lattice matching and staying below the critical thickness, and it occurs when the following is observed: $\Delta\gamma = \gamma_A + \gamma_i - \gamma_B \leq 0$ [5] for the growth of substance *A* on substance *B*, and where γ_A and γ_B are the surface free energies of *A* and *B* respectively and γ_i is the interfacial free energy. The function describes the necessity of the interfacial free energy and the free energy of the the grown substance being smaller than the surface energy of the substrate (or underlying layer), that is; it must be more energetically favourable to adhere to the growth surface rather than the other adatoms so that layer-by-layer growth can occur without 3D islands of material forming.

2.1.7.2 Volmer-Weber (VW) Growth[1]

This occurs for the opposite situation as presented for ideal FM growth, i.e. the free energy of the adatoms is much higher than that of the substrate surface. In this case, fully relaxed islands find sites and cluster together, bearing little resemblance to the substrate. This growth mode is typically the least desirable.

2.1.7.3 Stranski-Krastanow (SK) Growth[19]

This is almost a combination of the two above growth modes, and isn't dependent simply on the free energies at the interface, but additionally as a function of the growth thickness, which increases strain energy. The film will form what is known as a wetting layer, a layer of pseudomorphic 2D growth, and then, in order to relieve stress, the growth will become 3D in nature, creating islands on the wetting layer. SK growth was initially dis-

missed as problematic, but has since been seen as a valuable growth mode when growing self-assembled quantum dots- discovered in 1985[11]. This growth has a critical thickness in a similar manner to that of misfit dislocations, as there is a critical thickness before which the growth assumes a 2D behaviour. The shift into 3D growth is also a manner of strain relief as it is more energetically favourable to form the islands than to continue growing layer by layer. There remains, however, an inbuilt strain within this growth that can dislocate after the 3D growth has started. This makes it all the more difficult to approximate the critical thickness of a material which behaves in this manner, without having prior experience of the material in question (such as InAs on GaAs). Guha et al.[12] discuss the increase in the critical thickness of misfit dislocations in InAs on GaAs after SK growth occurs; they note that free-energy considerations imply that island formation in SK growth shows a propensity toward dislocation after the transition to 3D growth is made, although the islands are initially coherent. Although this is the case, a fifty-fold increase in critical thickness after island formation is observed, indicating a degree of strain reduction in the 3D growth, yet not complete elimination, as dislocations still occur.

2.1.8 RHEED Oscillations

In situations where 2D FM growth occurs, RHEED can be used to determine the growth rate during growth. The specular reflection of the electron beam through the sample surface varies in brightness according to the progress of growth of a single monolayer. As a monolayer forms on a crystal surface in MBE, adatoms adhere to existing atomic step edges, causing small islands to form and expand laterally across the surface until the layer is completed. The formation of these islands causes a larger scattering of the impinging electrons from the RHEED electron gun, thus reducing the intensity. As a full monolayer is completed, the brightness of the specular electron beam increases. This oscillation of brightness (known as RHEED oscillations) allows the determination of growth rate, as the periodic change in intensity is representative of the time it takes to grow one monolayer (Figure 2.1.6 [17]).

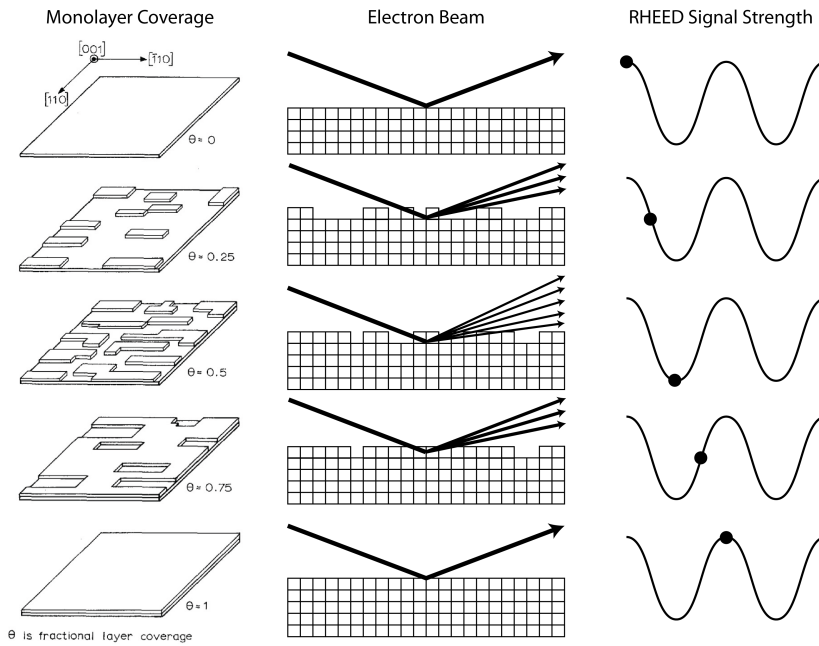


Figure 2.1.6: Basic Overview of 2D Monolayer Growth and the Effect on the RHEED Signal adapting a figure from [17]

2.1.9 Altering the Electrical Properties of a Grown Film

MBE is noted for on the purity of the material that it produces, but there are occasions when impurities are desired. This is certainly the case when attempting to make a semiconductor film more conductive, where the introduction of impurities is known as doping. There are two different types: n-doping, which introduces a “supervalent dopant” or “donor” into the crystal, and p-doping, which introduces an “aliovalent dopant” or “acceptor”. The impurity atom substitutes itself into the crystal lattice, with the difference in bonding to the surrounding lattice, introducing a carrier that is more mobile than one would find in an intrinsic semiconductor. For n-doping, this takes the form of an extra electron, whereas for p-doping an extra hole is introduced. In III-V semiconductors, a typical donor material is silicon, and a typical acceptor material is beryllium.

Similar to growth, the incorporation of dopant impurities is dependent on a molecular flux, but the flux is too small to be measured in the same way as the constituent materials of the grown crystal. Instead, the relationship between the dopant concentration and growth rate need to be known with respect to the temperature of the dopant cell. This is typically an exponen-

tial relationship and doesn't tend to alter significantly over the lifetime of the charge held in the dopant cell. Like the bulk material sources, dopant flux is controlled by mechanical shutters, allowing the sub-monolayer precision that is characteristic of MBE growth. Doping of an MBE-grown film is limited by the background impurities, and compensation at the low and high end of the dopant incorporation scale respectively.

2.2 Semiconductor Characterisation

In order to determine the properties of a sample grown by MBE it is necessary to characterise the material. This enables confirmation of the crystal quality, growth rate and other such properties that is not immediately obvious when faced with a sample straight from an MBE reactor. The most frequently used and preferred techniques are optical due to their (usually) non-destructive methods, such as PL and PLE. Unfortunately, there are times when the sample needs to be altered physically to determine various properties- be it simply cleaving for size-limited apparatus, or even the process being destructive, such as CV profiling.

2.2.1 Photoluminescence Spectroscopy (PL)

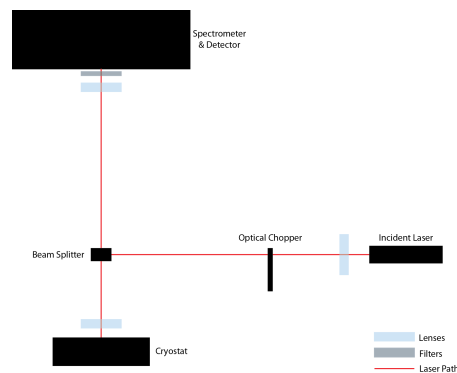


Figure 2.2.1: A basic overview of a typical PL experimental setup.

PL is used to characterise the emission of a spectrum of a device by the excitation of photocarriers by an external light source. More specifically, the source, usually a laser, with an emission energy greater than that of the band gap of the device, causes interband absorption, thereby promoting an electron from the valence band to the conduction band[15]. This electron pro-

motion also creates a "hole", and the electron hole pair typically lose energy through thermal and scattering processes, before recombining near the

valence and conduction band edges. This recombination can either be radiative or non-radiative, the likelihood of this depending upon a material-dependent property known as the luminescent efficiency; direct band gap semiconductors have high luminescent efficiency, with quantum-confined structures having much higher luminescent efficiencies, making PL an ideal method for their investigation.

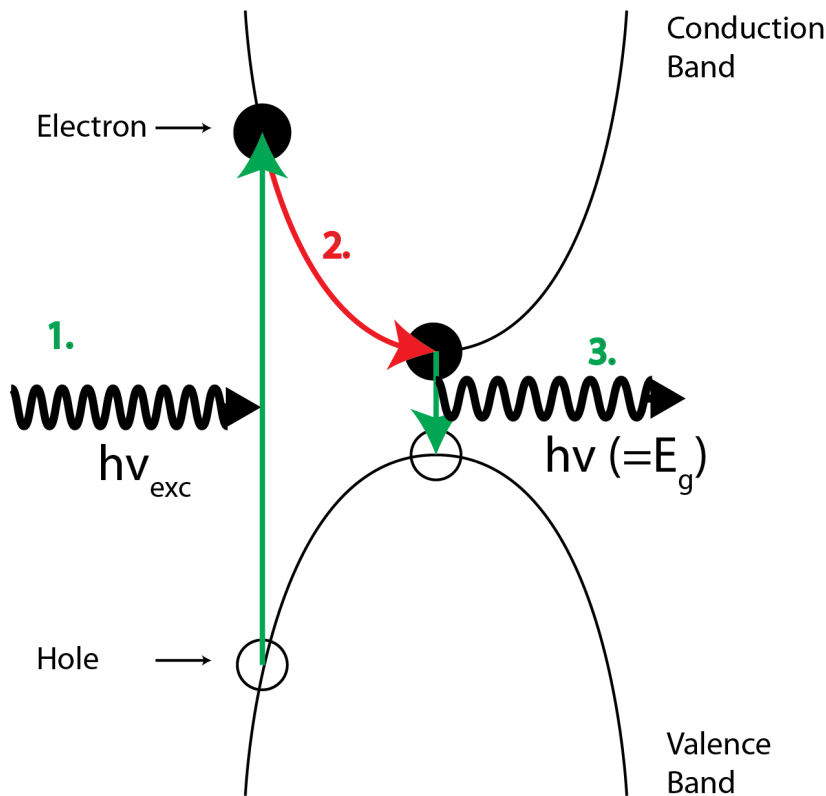


Figure 2.2.2: Simple overview of carriers being excited (1), relaxing to the conduction band minimum (2) and recombining to emit a photon (3) in a direct band gap semiconductor.

Direct band gap semiconductors are those that have a minimum state in the conduction band and a maximum state in the valence band at the same point in k -space (Figure 2.2.2). This means that exciting a carrier from the conduction band requires no change in momentum, simply a change in energy. As a result, carriers can be excited by photons alone. Although the semiconductors discussed in this thesis have a direct band gap, defects and impurities in the grown crystal can create non-radiative recombination centres, meaning that the luminescent efficiency is reduced, as the energy

from an electron-hole recombination is not guaranteed to be emitted as a photon.

The peak wavelength of the emitted spectrum indicates the typical energy of the recombined e-h pairs, which allow an approximate value for the energy of the ground state emission of a material to be calculated using the Planck relationship $E = hc/\lambda$, where E is the photon energy (approximately equivalent to the band gap, or at least the energy of the recombined e-h pair), h is the Planck constant, c is the speed of light and λ is the wavelength of the emitted light.

A typical example of PL apparatus involves an incident laser of suitable energy focused on the sample to be analysed, with the emitted light being collected by a detector suitable for the desired wavelengths, usually through a tuneable monochromator, diffraction gratings and, often, filters, unless the detector is an array of photosensitive devices which are able to take a snapshot of a large range of incoming wavelengths at once.

2.2.2 *Photoluminescence Excitation Spectroscopy (PLE)*

PLE is a variant of PL, as the name suggests: it also analyses the emission from a grown structure after being excited by an external light source. However, whereas PL excites a structure with a single wavelength and analyses an emitted spectrum, PLE varies the excitation wavelength and analyses the intensity of a selected wavelength (or, depending on the detector, an averaged selected spectrum). The emission spectrum will not change in its shape or wavelength, assuming the temperature is kept constant and the sample is uniform, allowing for any spatial deviations. It can therefore be assumed that the intensity of the peak of the emission is proportional to the carrier density, which, itself, is determined by the absorption coefficient. This means that the absorption coefficient at the exciting wavelength is proportional to the intensity[15]. This measurement technique is explored in more detail in chapter 5.

2.2.3 *Atomic Force Microscopy (AFM)*

AFM is a type of scanning probe microscopy that is able to measure at the nanometre-scale, allowing 3D analysis of the surface of samples, which is especially useful for the analysis of quantum dots (QDs). In basic terms, a cantilever with a sharp tip (typically with a tip width in the order of nanometres) raster scans the surface, with the

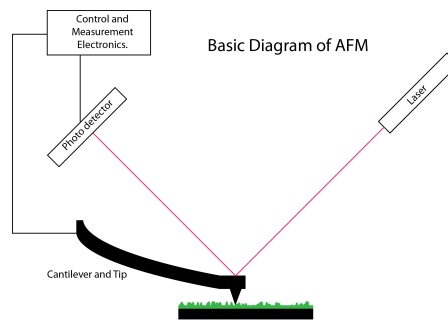


Figure 2.2.3: A basic overview of an atomic force microscope.

movement of the cantilever in reaction to the contour of the surface being relayed back to a computer, which then puts together an image of the scanned surface. The cantilever's movement is measured by piezoelectric sensors, or, more commonly, a laser dot focused on the top surface of the cantilever, which is reflected into a sensor that detects the movement of that reflection. A basic schematic diagram of an AFM setup is shown in figure 2.2.3.

AFM presents numerous advantages over similar measurement techniques:

- Little or no sample preparation required- AFM can be performed on a sample immediately after extraction from an MBE reactor.
- An accurate 3D surface image.
- Comparatively inexpensive due to the lack of need for vacuum environments, or high-voltage e-beam in electron-based microscopes.

Disadvantages typically involve the nature of image collection- as the micrograph is based on a raster-scanning technique, high-resolution images can take several hours, with the possibility of image artifacts or sample drift rendering such a scan useless. It may be noted that an AFM image does not fully represent the true sample surface topography, but rather the tip's interaction with the surface. Different tips mean that the interaction with surface features can be inaccurate, with the lateral size of an AFM tip potentially preventing lateral distance being accurately measured (figure 2.2.4). The AFM tool used was a Veeco/Digital Instruments Dimension V, and all analysis performed by this author was performed using WSxM software[4].

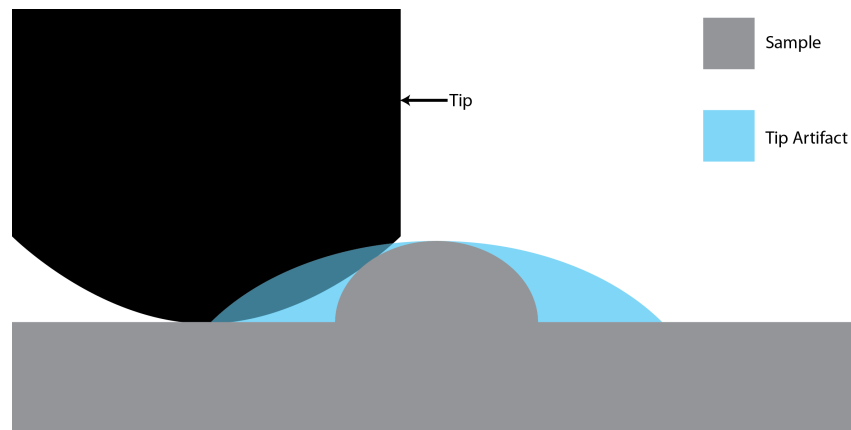


Figure 2.2.4: Simple Diagram Showing the Potential Inaccuracy of AFM, Depending on Tip Size

2.2.4 Doping Measurement

Although PL can be used as a method of determining the doping level within a grown film, there are more accurate and tailor-made measurements for the doping concentration.

2.2.4.1 Hall Measurements

Hall effect measurements are the simplest to perform, with the van der Pauw method[16] allowing for quick and easy measurement, after minor sample preparation. The measurement requires a volt meter, a current source and a magnet, usually with a bespoke sample holder to ensure repeatable measurements and easy calculation. The simplicity of the Hall measurement is also its downfall- foreknowledge of the thickness of the epilayer is required, only semi-insulating substrates can be used, and a single concentration doping layer can be used. This measurement is typically used for doping cell calibration, whereupon a thick doped layer, usually GaAs, is grown, keeping the dopant cell temperature constant.

In order to measure the dopant concentration in such a sample, it must be cleaved into a square, with contacts affixed to the corners and mounted on to a sample holder, as is shown in figure 2.2.5a. The resistances, R_V (“vertical” resistance) and R_H (“horizontal” resistance) are found by measuring the voltages (figure 2.2.5a) from a constant current being injected into opposing corners, with each measurement being reversed to ensure the sample is

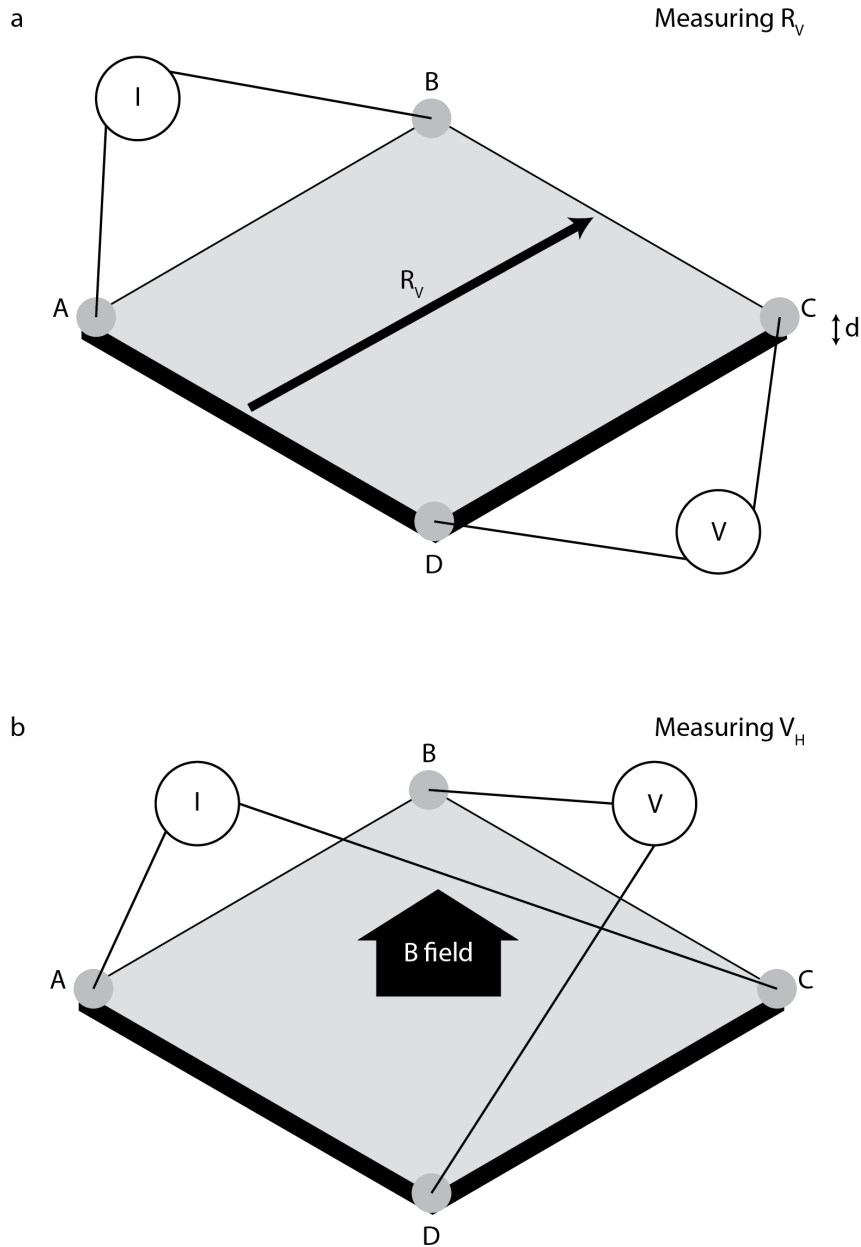


Figure 2.2.5: a. Example of the measurement of the “vertical” resistance, R_V on a square sample.

b. Example of the measurement of the Hall voltage, V_H on a square sample.

uniform. As an example (figure 2.2.5a), using R_V , current is first injected into points AB , with the voltage being measured across points DC , and then the measurements reversed (Current through BA , voltage measured across CD). The process is then repeated with the current through CD and voltage measured across AB , with the voltage measurements expected to be equal for a uniform sample. R_H is measured in a similar fashion. Once these

values are calculated using Ohm's law, the sheet resistance (R_S) is calculated numerically from equation 2.2.1:

$$\exp(-\pi R_V/R_S) + \exp(-\pi R_H/R_S) = 1 \quad (2.2.1)$$

From this, the resistivity and conductivity can be calculated:

$$\rho = \frac{1}{\sigma} = R_S d \quad (2.2.2)$$

With knowledge of R_S , further measurements can be made to determine the Hall voltage and thus the carrier density. This is done in a similar manner to the determination of the horizontal and vertical resistances, but with measurement of voltage across the diagonal of the sample, in the presence of a magnetic field, i.e. repeated for positive and negative magnetic field, voltages V_{DB} , V_{BD} , V_{AC} , V_{CA} are measured with the constant current injected through the respective points I_{AC} , I_{CA} , I_{BD} , I_{DB} (figure 2.2.5b). The reason for the repeated measurement at each point, with differing magnetic field polarity, is to negate the variation to asymmetry of the sample, or contact placement. The polarity of the sum of the difference of the measurements is then used to determine whether the sample is n - or p -type- $V_1 = V_{DBP} - V_{DBN}$, $V_2 = V_{BDP} - V_{BDN}$, $V_3 = V_{ACP} - V_{ACN}$, $V_4 = V_{CAP} - V_{CAN}$, where the suffixes N and P refer to the polarity of the magnetic field, with the polarity of the sum $V_1 + V_2 + V_3 + V_4$ yielding the sample type, and halving the average of these values yielding the average Hall voltage. The sheet carrier density, n_s , is determined thusly (in m^{-2}):

$$n_s = \frac{IB}{e|V_H|} \quad (2.2.3)$$

Where I is the current, B is the magnetic field and e is the electronic charge. The bulk carrier density is calculated by dividing the sheet carrier density by the thickness of the grown layer, giving a value of carriers per unit volume, and usually converted to cm^{-3} . The Hall mobility can also be calculated:

$$\mu_H = \frac{1}{qn_s R_S} \quad (2.2.4)$$

It should be noted that this measurement is temperature and light-sensitive, meaning that the measurement apparatus should be constructed in such a fashion that it ensures a repeatable process.

2.2.4.2 *Electrochemical Capacitance-Voltage (ECV) Profiling*

As the majority of device samples require a varying dopant concentration, occasionally an alternative to Hall is required to measure the doping in a grown film. One such measurement is the destructive method of ECV profiling in a lot of cases because, despite the disadvantage of the alteration of the sample, detailed analysis can be done throughout the profile of the sample. This method measures the ions within a grown crystal, instead of the free carriers, meaning that the output doesn't only take into account dopant atoms, but rather any and all ionic impurities incorporated into the film. This measurement is preferred over Hall when the sample is non-uniform in its doping, has a differing material structure throughout, or has a doped substrate.

ECV profiling uses an electrolyte to etch into the material being measured, so that measurements of the doping levels can be made at different depths into the material, thus creating a profile of the dopant concentration vs. the depth. The doping levels are measured by applying a bias across the electrolyte-semiconductor junction (which acts as a Schottky junction), thus creating a depletion region, forming a capacitance, meaning that any electrically active impurities, i.e. dopant atoms, will determine the width of the depletion region as a function of the applied bias. From Ambridge and Faktor[7], we can use the capacitance to calculate the number of dopant atoms within the grown layer:

$$C = \left(\frac{(qn\epsilon_0\epsilon)}{2} \right)^{1/2} \cdot \psi^{-1/2} \cdot A \quad (2.2.5)$$

Where q is the electronic charge, n is the net donor concentration, ψ is the barrier height potential, A is the area and ϵ_0 and ϵ are the permittivity of free space and relative permittivity of the semiconductor respectively. The depletion width is given by:

$$W_D = \frac{\epsilon_0 \epsilon A}{C} \quad (2.2.6)$$

This means that, assuming that ψ , ϵ and A are known, n can be calculated by using the following:

$$n = \frac{2\epsilon_0 \epsilon}{q} \cdot \frac{\delta V}{\delta(W_D^2)} \quad (2.2.7)$$

This is done automatically at set intervals during the etch of the semiconductor, by measuring the voltage and capacitance. The etch rate is controlled by altering the etch voltage to provide a suitable current within the electrolyte to etch the semiconductor. Problems arise in this technique if the etch is uneven, and instead of etching the surface, pits begin to form thus meaning that the capacitance of a range of depths is measured, resulting in inaccurate data. Figure 2.2.6 shows a typical CV profile measurement, performed on a silicon doping staircase sample, whereupon the temperature of the silicon is altered for set growth thicknesses. The inconsistency at around $1.6 \mu\text{m}$ is due to the etch reaching an AlGaAs barrier layer.

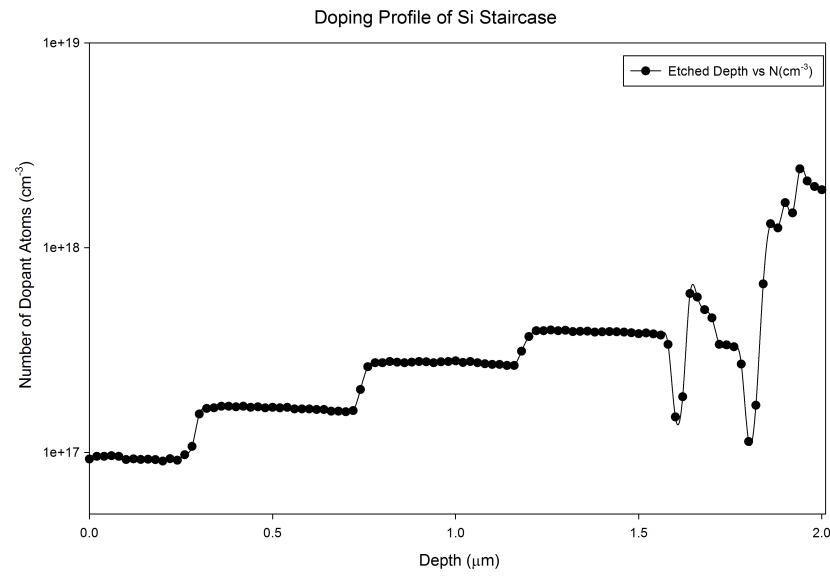


Figure 2.2.6: CV Profile of a Doping "Staircase" Sample.

2.2.5 X-Ray Diffraction (XRD)

XRD enables the measurement of the physical parameters of the grown crystal. This is particularly useful for heterostructures whereupon the lattice constant of the deposited material varies depending on the composition of both the epilayer and substrate. The advantage of x-rays for this measurement is the similarity of the wavelength to that of atomic dimensions (the assigned range of wavelengths for x-rays in the e-m spectrum is from 0.01 Å to 100 Å). XRD uses copper sources for x-ray generation, with $K_{\alpha} = 1.5406 \text{ \AA}$, compared to the lattice constant, a , of GaAs, $a = 5.65 \text{ \AA}$ - when using a copper tube source, the emission is so sharp that it is assumed to be monochromatic. Heterostructures require the growth of materials with different lattice constants, with compressive or tensile strain (figure 2.1.5) altering the structure of the grown film compared to the bulk material, as it is having to match itself to the underlying substrate. As a result, the change in the lattice constant in the vertical direction is a measure of the composition and strain of the grown material.

Diffraction occurs when every object in a periodic array scatters radiation coherently, producing interference when the aforementioned radiation is coherent and monochromatic. A crystal is a highly ordered periodic array of atoms, with each atom being excellent coherent scatterers of x-rays. For coherent, monochromatic light, the Bragg diffraction peak occurs for planes within a FCC crystal which are unmixed, with (hkl) needing to be all odd or even numbers². The lowest integer case for where this is true is the (111) plane, and is the typical reflection used in XRD.

Unfortunately, with heteroepitaxy, one cannot assume perfect epitaxy, where the grown film is in perfect registry with the substrate, with zero defects, particularly if the difference in lattice constants is large, but the substrate and film layers will produce separate plane waves as a result of the diffraction from their respective crystalline structure, meaning that any peaks in x-ray detection outside of the expected substrate peak can be assigned to the epilayer. Despite the knowledge that the epitaxy is unlikely to be perfect, most films grown for this thesis are assumed to be pseudomorphic, so

² This thesis does not deviate from FCC Zinc-Blende materials, with the majority of III-V materials adhering to this crystal structure

that essentially the overall lateral lattice parameter remains constant, and the lattice parameter in the growth direction distorting as a result. This type of strained growth will continue for varying amounts depending on the lattice mismatch between substrate and epilayer, but will eventually dislocate and relax, meaning the lateral lattice parameter of the epilayer will assume that of the natural bulk crystal. Aside from quantum dot growth (explored in later chapters), all epilayers are kept below this critical thickness, leaving the x-ray crystallography relatively simple (particularly due to the symmetrical nature of the FCC crystal type).

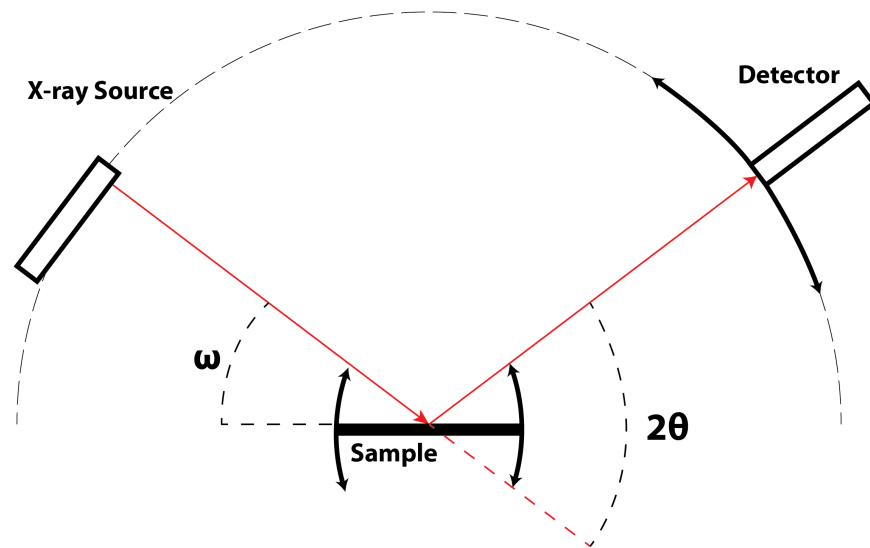


Figure 2.2.7: Diagram showing XRD Geometry including relevant experimental angles

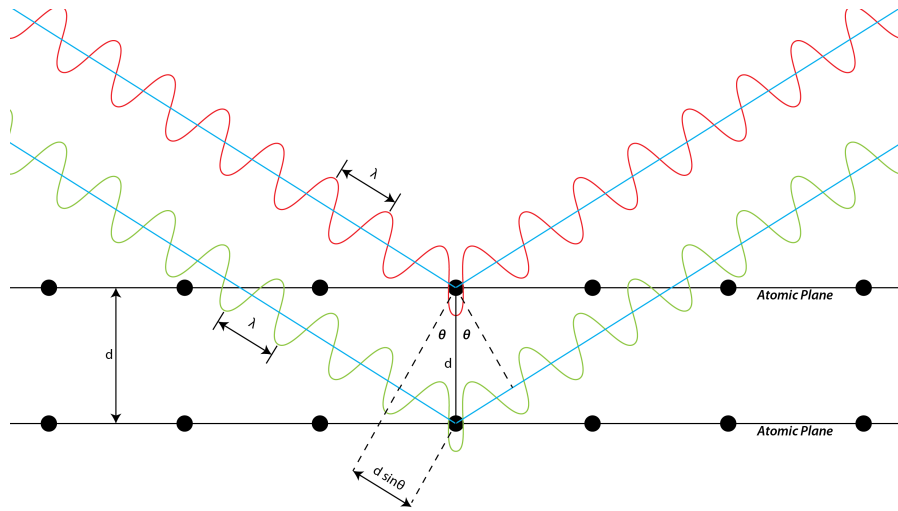


Figure 2.2.8: A diagram to aid the explanation of Bragg's Law (equation 2.2.8)

Figure 2.2.7 shows a basic overview of a typical XRD experimental set up. The detector is moveable, as is the substrate stage, with the angle between the substrate and x-ray source (ω) and the angle between the detector and x-ray source (2θ) being the values most relevant to the analysis required in this thesis. Although XRD can be used for extremely detailed crystallographic mapping techniques, a basic requirement for epitaxy is the identification of the composition of a grown film, alongside the thickness of that film, both of which allow for a precise determination of the growth rate of a substance if RHEED or other techniques are not forthcoming. Although a scan based on ω (rocking curve) or 2θ (detector scan) is useful, a coupled omega-2theta scan is used to measure the Bragg diffraction angle, which is a plot of the intensity of the scattered x-rays vs. 2θ , with ω changing linked to 2θ so that $\omega = 1/2 \cdot 2\theta + \text{offset}$. This scan allows analysis of layer composition, thickness, lattice mismatch, relaxation and superlattice period, as each of these properties affect the position of the Bragg diffraction peak. As more than one of these parameters is usually unknown, modelling is usually required to aid analysis- as an example, if the growth rate is not fully known, the composition *and* the thickness of a grown film will be uncertain. Bragg's law dictates the conditions for x-ray interference in a crystal, as is shown in figure 2.2.8, as described by the following equation:

$$n\lambda = 2d \sin \theta \quad (2.2.8)$$

Where n is an integer, λ is the x-ray's wavelength, d is the interplanar spacing and θ is the incident angle.

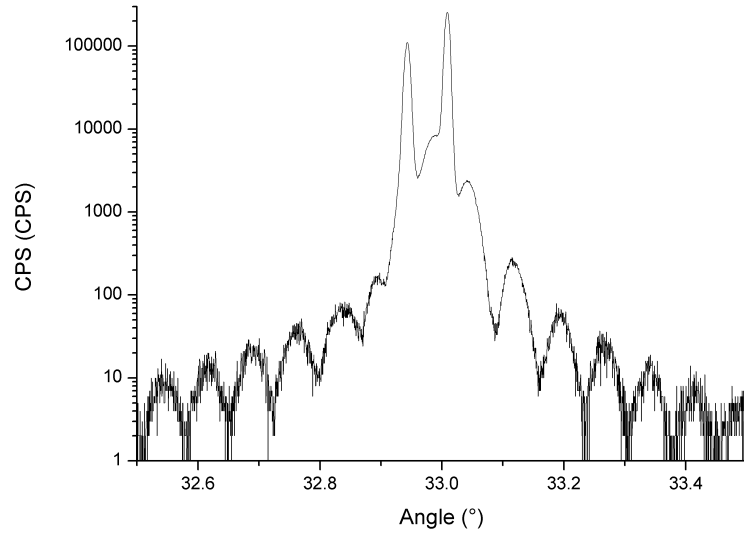


Figure 2.2.9: Example of an XRD Omega-2Theta scan on a heteroepitaxial sample

The relative peak spacing in a coupled scan informs us of the lattice parameter in the growth direction, which in turn provides information about the composition, strain or relaxation, whereas the intensity of the peak and associated “thickness fringes” giving us information regarding the thickness of the grown film. Looking at figure 2.2.9, there are two clear peaks, with the higher intensity narrow peak belonging to the substrate, with position ω_s . The other, broader and less intense peak, is due to the slightly strained epilayer. The mathematics of the calculation of the thickness, composition etc. is usually left to modelling and fitting software, due to the necessary calculations being time-consuming and complex, although the use of Vegard’s law[8, 18] allows for the calculation of the composition based on the assumption that the grown film is pseudomorphic:

$$a_L^R(x) = xa_A + (1 - x)a_B \quad (2.2.9)$$

Where $a_L^R(x)$ is the relative lattice constant of the film A_xB_{1-x} , a_A and a_B are the lattice constants of material A and B respectively, with x representing the fraction of the material in the alloy.

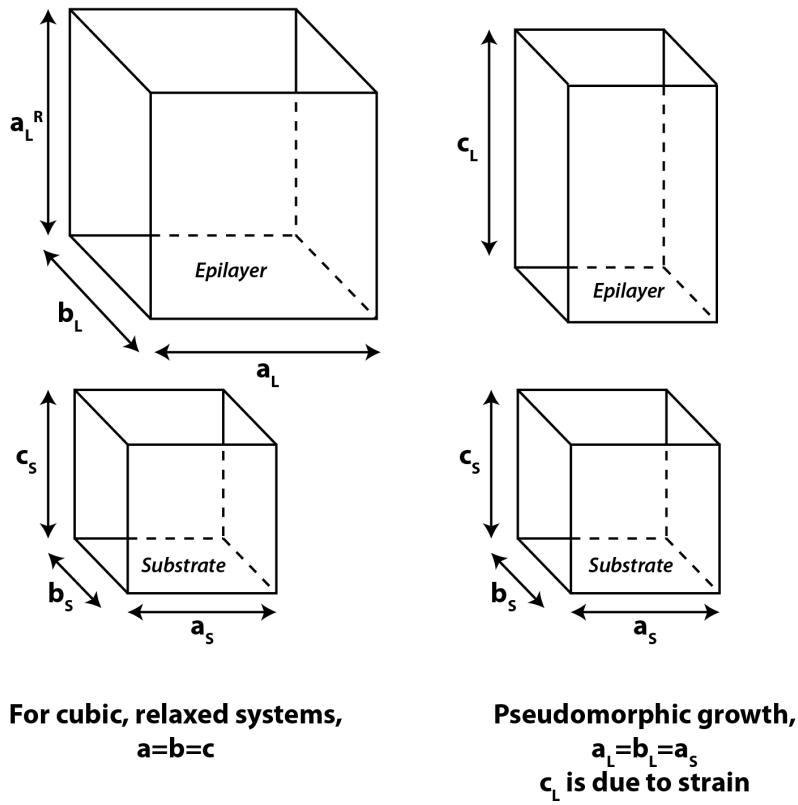


Figure 2.2.10: 3D example of the effect of strain on a unit cell, and the corresponding terminology.

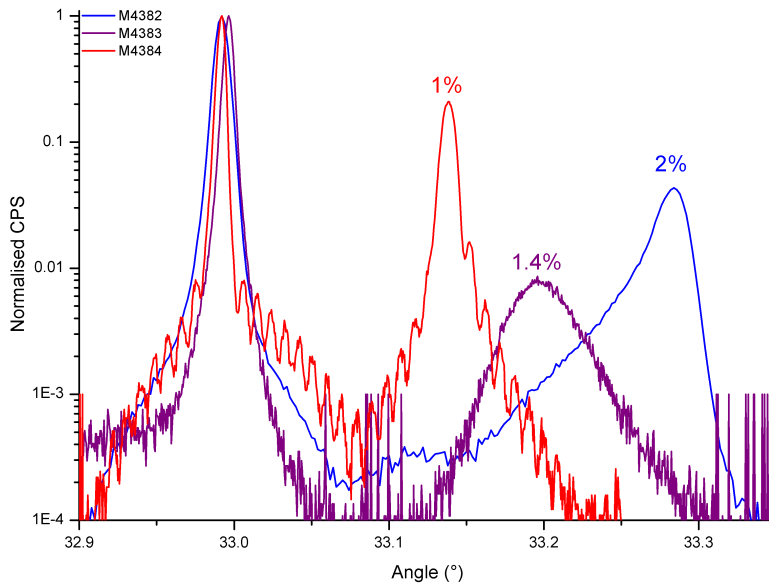


Figure 2.2.11: Nitrogen composition

Figure 2.2.11 shows the compositional analysis of a range of $\text{GaN}_x\text{As}_{1-x}$ samples grown in an attempt grow a film containing 1% nitrogen. The sample was grown on the VG Semicon V80 reactor, and the XRD measurement was performed on a Bruker D8 Discover tool. The crystal quality varied when growing as a result of the N_2 cell not-being properly calibrated; the first sample grown yielded the 1.4% result, which is particularly poor quality. As the lattice constant of GaN is rather smaller than that of GaAs, a GaAs layer containing nitrogen will be under tensile strain due to a reduction in the lattice constant, with the epilayer's x-ray peak appearing on the right of the substrate peak as a result of the compression of the lattice in the growth direction. Using values from figure 2.2.11, it is possible to calculate the composition.

The mismatch [10] is described as

$$m = \frac{a_L^R - a_S}{a_S} \quad (2.2.10)$$

Where a_L^R is the relative lattice constant as used in Vegard's law (equation 2.2.9), and a_S is the lattice constant of the substrate. However, in omega-2theta measurements, only the mismatch in the growth direction is measured, so altering equation 2.2.10, we find the following:

$$m_{\perp} = \frac{c_L - a_S}{a_S} = \left(\frac{\Delta a}{a_S} \right)_{\perp} = \frac{\Delta d}{d} = \frac{\sin \theta_S - \sin \theta_L}{\sin \theta_L} \quad (2.2.11)$$

Where the subscript L represents the grown layer and S represents the substrate, a is the lattice constant, d is the interplanar distance as described by Bragg's law (equation 2.2.8), and θ is the scattering angle, in this case using values from the data in figure 2.2.11. The mismatch can also be described as follows:

$$m = \left(\frac{1 - \nu}{1 + \nu} \right) m_{\perp} \quad (2.2.12)$$

Where ν is the Poisson ratio ($\nu_{\text{GaAs}} = 0.31$). Rearranging Vegard's Law (equation 2.2.9) and substituting in the appropriate values, we can find the composition:

$$m = \frac{a_L^R - a_S}{a_S}$$

$$a_L^R = a_S(m + 1)$$

Substituting into equation 2.2.9,

$$x = m \left(\frac{a_S}{a_L - a_S} \right) \quad (2.2.13)$$

Therefore, using the data from figure 2.2.11, composition for each sample is calculated and shown in table 2.2.1.

Sample	θ_S	θ_E	m_{\perp}	m	x
M4382	32.992	33.284	-0.007772	-0.004094	-0.020
M4383	32.996	33.197	-0.005362	-0.002824	-0.014
M4384	32.992	33.138	-0.003921	-0.002065	-0.010

Table 2.2.1: X-ray calculation using values from figure 2.2.9.

These values are backed up by simulation/fitting software used with the XRD measurement software, represented by the values in figure 2.2.11. The difference between each of these samples is the RF power exciting the nitrogen gas, with the optical power varying for each. Although figure 2.1.4 in section 2.1.5.2 shows the optimal optical power occurring at the flow rate of 10% (0.1 sccm), it was found that the N incorporation was far too high, and the flow rate was halved. Further reduction in RF power was required in order to attain the desired composition of $\text{GaN}_{0.01}\text{As}_{0.99}$, with the samples described in both figure 2.2.11 and table 2.2.1 using RF powers of 150 W, 100 W and 75 W for M4382, M4383 and M4384 respectively.

2.3 References

- [1] K. Oura, M. Katayama, A. V. Zotov, V. G. Lifshits, and A. A. Saranin, *Surface Science*, ser. Advanced Texts in Physics. Berlin, Heidelberg: Springer Berlin Heidelberg, 2003. [Online]. Available: <http://link.springer.com/10.1007/978-3-662-05179-5>
- [2] E. Bauer, "Phänomenologische Theorie der Kristallscheidung an Oberflächen. I," *Zeitschrift für Kristallographie*, vol. 110, pp. 372–394, 1958. [Online]. Available: http://adsabs.harvard.edu/cgi-bin/nph-data_query?bibcode=1958ZK....110..372B&link_type=EJOURNAL
- [3] C. T. Foxon, J. A. Harvey, and B. A. Joyce, "The evaporation of GaAs under equilibrium and non-equilibrium conditions using a modulated beam technique," *Journal of Physics and Chemistry of Solids*, vol. 34, no. 10, pp. 1693–1701, 1973. [Online]. Available: <http://www.sciencedirect.com/science/article/pii/S0022369773801350>
- [4] I. Horcas, R. Fernández, J. M. Gómez-Rodríguez, J. Colchero, J. Gómez-Herrero, and A. M. Baro, "WSXM: A software for scanning probe microscopy and a tool for nanotechnology," *Review of Scientific Instruments*, vol. 78, no. 1, p. 013705, 2007. [Online]. Available: <http://scitation.aip.org/content/aip/journal/rsi/78/1/10.1063/1.2432410>
- [5] E. Bauer and J. H. van der Merwe, "Structure and Growth of Crystalline Superlattices - From Monolayer to Superlattice," *Physical Review B*, vol. 33, no. 6, pp. 3657–3671, 1986. [Online]. Available: <http://journals.aps.org/prb/abstract/10.1103/PhysRevB.33.3657>
- [6] F. C. Frank and J. H. van der Merwe, "One-dimensional dislocations. I. Static theory," *Proceedings of the Royal Society of London. Series A. Mathematical and Physical Sciences*, vol. 198, no. 1053, pp. 205–216, 1949. [Online]. Available: <http://rspa.royalsocietypublishing.org/content/198/1053/205.short>
- [7] T. Ambridge and M. M. Faktor, "An automatic carrier concentration profile plotter using an electrochemical technique," *Journal of Applied*

- Electrochemistry*, vol. 5, no. 4, pp. 319–328, 1975. [Online]. Available: <http://link.springer.com/article/10.1007/BF00608796>
- [8] A. R. Denton and N. W. Ashcroft, “Vegard’s Law,” *Physical Review A*, vol. 43, no. 6, pp. 3161–3164, 1991. [Online]. Available: <http://gateway.webofknowledge.com/gateway/Gateway.cgi?GWVersion=2&SrcAuth=mekentosj&SrcApp=Papers&DestLinkType=FullRecord&DestApp=WOS&KeyUT=A1991FD04500063>
- [9] A. Guillen-Cervantes, Z. Rivera-Alvarez, M. Lopez-Lopez, E. Lopez-Luna, and I. Hernandez-Calderon, “GaAs surface oxide desorption by annealing in ultra high vacuum,” *Thin solid films*, vol. 373, no. 1-2, pp. 159–163, 2000. [Online]. Available: <http://www.sciencedirect.com/science/article/pii/S0040609000011263>
- [10] F. C. Frank and J. H. van der Merwe, “One-dimensional dislocations. II. Misfitting monolayers and oriented overgrowth,” *Proceedings of the Royal Society of London. Series A. Mathematical and Physical Sciences*, vol. 198, no. 1053, pp. 216–225, 1949. [Online]. Available: <http://rspa.royalsocietypublishing.org/content/198/1053/216.short>
- [11] L. Goldstein, F. Glas, J. Y. Marzin, M. N. Charasse, and G. Le Roux, “Growth by molecular beam epitaxy and characterization of InAs/GaAs strained-layer superlattices,” *Applied Physics Letters*, vol. 47, no. 10, p. 1099, 1985. [Online]. Available: <http://scitation.aip.org/content/aip/journal/apl/47/10/10.1063/1.96342>
- [12] S. Guha, A. Madhukar, and K. C. Rajkumar, “Onset of incoherency and defect introduction in the initial stages of molecular beam epitaxial growth of highly strained $\text{In}_x\text{Ga}_{1-x}\text{As}$ on $\text{GaAs}(100)$,” *Applied Physics Letters*, vol. 57, no. 20, p. 2110, 1990. [Online]. Available: <http://scitation.aip.org/content/aip/journal/apl/57/20/10.1063/1.103914>
- [13] G. P. Srivastava, “Theory of semiconductor surface reconstruction,” *Reports on Progress in Physics*, vol. 60, no. 5, p. 561, 1997. [Online]. Available: <http://iopscience.iop.org/0034-4885/60/5/002>

- [14] C. R. Stanley, M. C. Holland, A. H. Kean, J. M. Chamberlain, R. T. Grimes, and M. B. Stanaway, "4x10⁵ Cm²/V/s Peak Electron Mobilities in GaAs Grown by Solid Source MBE with As₂," *Journal of Crystal Growth*, vol. 111, no. 1-4, pp. 14-19, May 1991. [Online]. Available: <http://gateway.webofknowledge.com/gateway/Gateway.cgi?GWVersion=2&SrcAuth=mekentosj&SrcApp=Papers&DestLinkType=FullRecord&DestApp=WOS&KeyUT=A1991FT19000003>
- [15] M. Fox, *Optical Properties of Solids*. Oxford University Press, Mar. 2010. [Online]. Available: http://books.google.co.uk/books?id=K9YJ95okBDsC&dq=intitle:optical+properties+of+solids+inauthor:fox&hl=&cd=1&source=gbs_api
- [16] L. J. van der Pauw, "A method of measuring specific resistivity and Hall effect of discs of arbitrary shape," *Philips Research Reports*, vol. 13, pp. 1-9, Feb. 1958.
- [17] J. H. Neave, B. A. Joyce, P. J. Dobson, and N. Norton, "Dynamics of Film Growth of GaAs by MBE From Rheed Observations," *Applied Physics a-Materials Science & Processing*, vol. 31, no. 1, pp. 1-8, 1983. [Online]. Available: <http://link.springer.com/article/10.1007/BF00617180>
- [18] L. Vegard, "Die konstitution der mischkristalle und die raumfüllung der atome," *Zeitschrift für Physik A Hadrons and Nuclei*, vol. 5, no. 1, pp. 17-26, 1921. [Online]. Available: <http://www.springerlink.com/index/U186712No7000859.pdf>
- [19] I. N. Stranski and L. Krastanow, "Zur Theorie der orientierten Ausscheidung von Ionenkristallen aufeinander," *Monatshefte für Chemie*, vol. 71, no. 1, pp. 351-364, Dec. 1937. [Online]. Available: <http://link.springer.com/10.1007/BF01798103>

AN INTRODUCTION TO QUANTUM DOT GROWTH

Semiconductor advances have enabled the exploitation of quantum mechanics for desired macroscopic results, particularly when it comes to optoelectronic devices. The ability afforded by MBE to manipulate crystal growth on the monolayer scale (2.83 Å for GaAs) enables the engineering of systems to affect the behaviour of electrons and other carriers primarily by altering the band-gap of a grown structure. The appeal of this low-dimensionality is the emergence of quantum effects, which arise after a carrier is confined to a region whose dimensions are comparable to the carrier's de Broglie wavelength. These effects allow precise control over optical characteristics in a direct band gap semiconductor, as well as increasing the likelihood of electron-hole recombination, which increases luminescent efficiency in an optoelectronic system. The dimensions of confinement are defined as follows[11]: $\Delta x \approx \sqrt{\frac{\hbar^2}{mk_B T}}$, where x is the confining dimension, \hbar is the Planck constant, m is the mass of the particle, k_B is the Boltzmann constant and T is the temperature in Kelvin. This refers to a carrier being confined in an infinite potential well. This confinement leads to an uncertainty in its momentum ($\Delta p_x \approx \hbar/\Delta x$), which in turn gives it an increase in kinetic energy ($E_{Confinement} = \Delta p_x^2/2m$). Using values for GaAs ($m_e^* = 0.063m_0$), Δx is determined to be 6.84 nm at 300 K, with the increase in energy due to confinement being 12.9 meV at that value. Confinement is an essential part of this thesis due to work with quantum confining structures such as quantum dots. It forms the basis of optical emission from the samples studied throughout the thesis.

As a heterostructure, carrier confinement was first explored in the 1970s[10] in the form of quantum wells (QW)- a method of confinement that reduces the freedom of carriers from three dimensions (x,y,z), as in bulk, to two dimensions (x,y). This quantum well is, practically speaking, a thin layer of semiconductor sandwiched between another semiconductor comprised of a different material, with a comparatively larger band gap. This larger band gap means that the carriers are trapped by the potential barriers either side of the quantum well, meaning that, in the confined direction, carrier energy is limited to standing waves whose nodes are at the edges of the quantum well. This is a particularly useful method of carrier confinement due to the ease of growth (excluding cases of extreme lattice mismatch), particularly by MBE; an abrupt change in composition allows for a quantum well to be made with monolayer precision, with confinement for most carriers requiring dimensions smaller than 10nm in the growth direction, although modelling with a QW solver shows that even a very wide QW (on the order of 30nm) provides a slight confinement energy- ~ 1 meV.

The success of quantum wells lent motivation to create structures with increased confinement[1, 2], although in order to reduce the dimensionality of the system further, to 1-dimension, requires complex growth techniques, and usually some external processing- i.e. not in-situ growth. However, to achieve 0-dimensional systems, an exploitation of the Stranski-Krastanow growth mode can be employed; with un-dislocated nano-scale islands forming under certain growth conditions. Although Volmer-Weber growth provides 3D islands, it is far from ideal, as the islands created are often dislocated and by definition relaxed, and typically don't follow the underlying material's structure as a result, with defects providing non-radiative recombination centres for carriers.

Quantum dots (QDs) confine carriers in three dimensions, which has led to their moniker "artificial atoms". Systems of higher dimensionality have a continuous component of energy in the unconfined direction, meaning that the energy is not fully quantised. However, in a quantum dot system, the energy is fully quantised, reducing the density of states to a series of delta-like energy levels. The alteration of a carrier's energy by the addition of confinement energy is controllable by altering the size of the confining

feature, as well as the composition and strain of the material it is made from.

In terms of growth, self-assembled quantum dots are formed by a spontaneous energy-based process based on the free energies of the adatoms involved in the crystal growth. As mentioned in section 2.1.7, the Stranski-Krastanow mode of growth starts with a pseudomorphic 2D layer before it becomes energetically favourable to form 3D islands. As a result of this spontaneous process, the islands are not all the same size, in fact forming a standard distribution of sizes, and, as any emission from a quantum dot system is based on the size of the quantum dots, the emission follows the same distribution.

3.1 Light Emission from Quantum Dots

As carrier confinement increases the luminescence efficiency, most quantum confined structures are used for light emitting and absorbing devices. The three-dimensional quantisation provides an atom-like emission profile for individual dots, with an ensemble emitting in a representation of the standard distribution of the quantum dot sizes, known as inhomogeneous broadening.

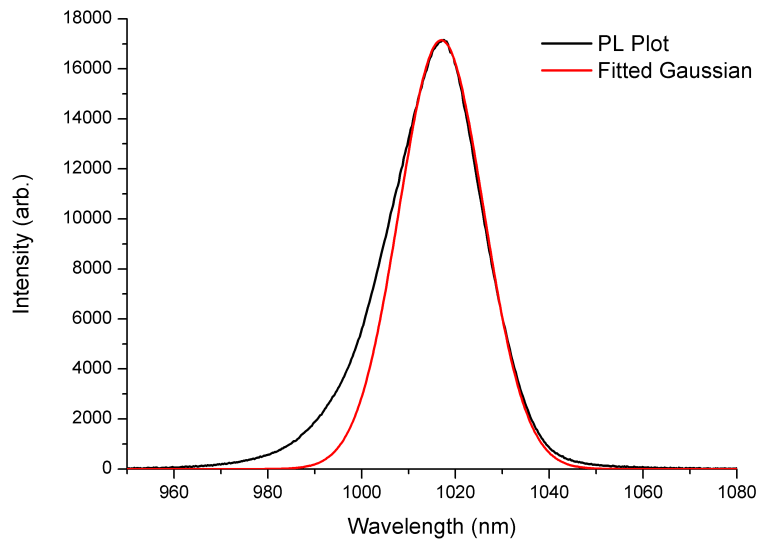


Figure 3.1.1: PL of Single-Layer Quantum Dots (black) with accompanying Gaussian fit (red).

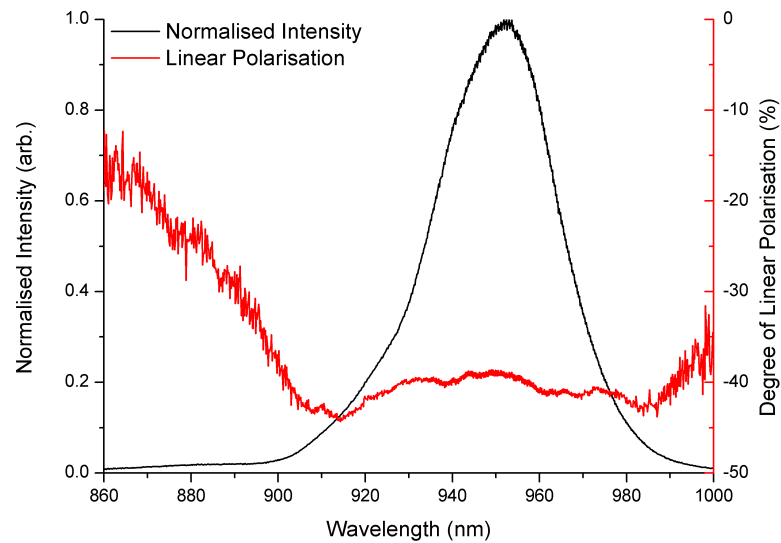


Figure 3.1.2: Edge PL of a quantum dot sample (black) with accompanying linear polarisation measurement (red)

Figure 3.1.1 shows the typical PL emission from a structure containing a single layer of dots, showing the almost-Gaussian form of the emission from the ground state of the quantum dots, which will be discussed further later in this chapter.

The ratio of dot height to the base width is typically small, with the base being up to 10 times larger. This affects the polarity of the light being emitted from such a structure, usually favouring the Transverse Electric (TE) (as opposed to Transverse Magnetic- TM) mode due to both the flattened QD structure, and the high strain field present, when considering light emitted from a direction perpendicular to the growth (figure 3.1.2). Figure 3.1.2 shows the edge PL and corresponding polarisation from a quantum dot sample. Edge PL focuses on the cleaved edge of a sample instead of the surface, otherwise the measurement conditions are identical. The polarisation shown in figure 3.1.2 refers to the horizontal-vertical linear polarisation being emitted from the QDs, with the negative value indicating the polarisation is horizontal rather than vertical (TE) mode emission. This measurement from the edge of the sample is particularly useful as light emission from the edge is a common device design (e.g. edge-emitting lasers). PL from the plan view of a sample typically yields very small amounts of polarisation, which seems to indicate that the QDs are symmetrical perpendicular to the growth direction.

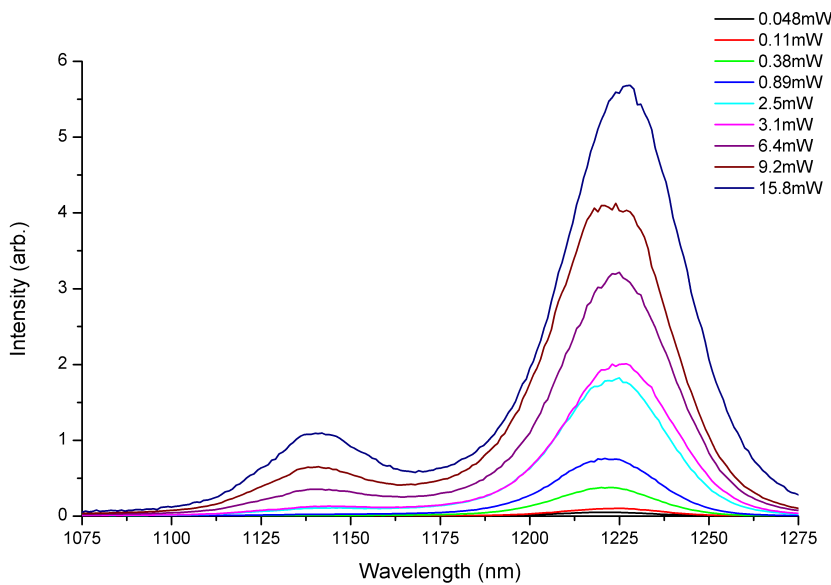


Figure 3.1.3: Power Dependent PL spectra from a single layer quantum dot sample

The power dependent PL experiment as described in figure 3.1.3 was performed at 10 K, with a laser as an excitation source whose excitation power was altered by using neutral density filters between the source and

the samples. If the power is increased, higher excited states emit at higher energies, each with a similar gaussian profile. Figure 3.1.3 shows the power-dependent emission of a quantum dot sample, with an excited state emerging as the power increases, on the short wavelength (high energy) side of the ground state peak. This happens due to the Pauli blocking, which is the manifestation of the Pauli exclusion principle, in that an electron transition is inhibited due to its destination being occupied. In other words, only a single electron can occupy any state with a particular set of quantum numbers; if an electron is introduced into a system, it is forbidden to share the same quantum numbers as another electron in that system. This means that as more electrons are excited, the quantum dots do not have sufficient occupancy in their low density of states to allow a ground state transition, and so the next state above starts to fill. This is described simplistically in figure 3.1.4. The low excitation diagram on the left of the figure shows a quantum dot that is emitting only from the ground state, as the carrier generation is not filling the ground state. The high excitation diagram shows a quantum dot whose ground state is full, and is therefore emitting from the first excited state (X1). The ground state also emits in this case, but it would have cluttered the image. If we consider a quantum dot ensemble that are excited so that the majority are emitting from the first excited state, it stands to reason that there would be two gaussian-like emission peaks centred on the ground and first excited state respectively. This is represented experimentally in the PL plot shown in figure 3.1.3.

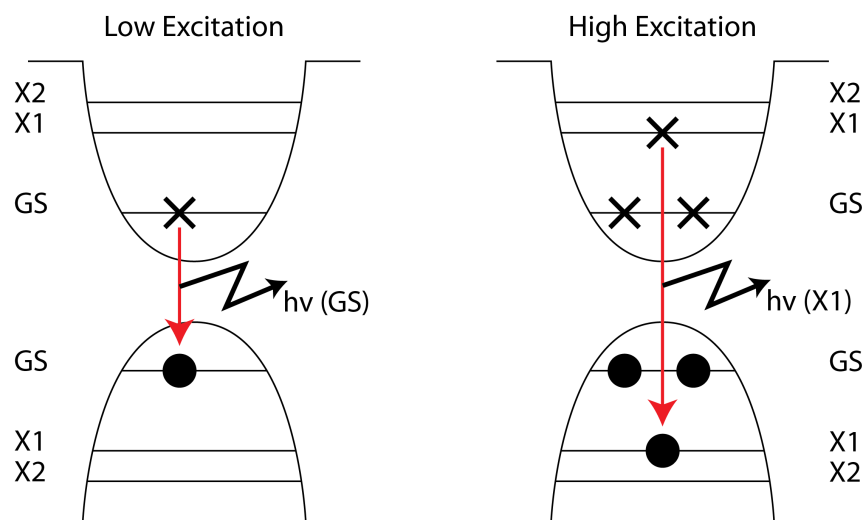


Figure 3.1.4: A basic overview of state filling in quantum dots.

3.1.0.1 Temperature Dependence

According to Varshni [40], the band gap of a semiconductor varies with temperature as described by the Varshni equation:

$$E_g(T) = E_{g0} - \frac{\alpha T^2}{T + \beta^2} \quad (3.1.1)$$

Where E_{g0} is the band-gap of the material at 0 K, and α and β are material-related constants. As the band gap and luminescence wavelength are linked, it is possible to observe the change in the band gap by altering the temperature of a sample and taking PL measurements. In the case of quantum dots, the change in emission energy does not represent the change in band gap, but instead the change in the ground state. This has a more complex response to the change in temperature, instead having a sigmoidal relationship, based on a number of factors that will not be discussed here [4]. The evidence for this is seen in temperature dependent PL experiments. Using the sample as described in figure 3.1.5, this is performed, with results seen in figure 3.1.6. The “low temperature” GaAs is grown at the same temperature as the InAs QDs at 590 °C thermocouple temperature, compared to 670 °C, which is the temperature that GaAs is typically grown at on the NC machines.

950Å GaAs
50Å Low Temperature GaAs Cap
2.4 ML InAs QDs
3000Å GaAs Buffer
GaAs Substrate

Figure 3.1.5: Sample Structure as used in Temperature Dependent PL Measurements

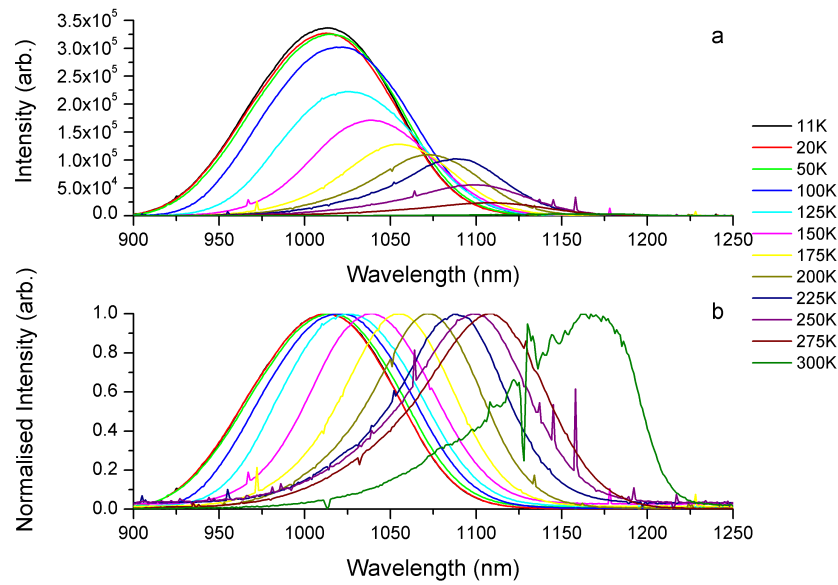


Figure 3.1.6: Graphs showing a) Temperature Dependent PL and b) Normalised Temperature Dependent PL from the sample as described in figure 3.1.5.

Figure 3.1.6a) shows the change in emission as the temperature rises from 10 K to 300 K, with not only the wavelength changing, but the intensity as well. The latter is due to the carriers' thermal energy providing sufficient energy to escape the confining structures without providing an optical recombination- with a larger temperature, more carriers are likely to escape. Figure 3.1.6b) shows the normalised intensity spectra from the same sample, so that the change in wavelength is more clear. Another temperature-related change seen in figure 3.1.6 is that of the shape of the emitted spectrum. In the low temperature emission, the shape is Gaussian, indicating a random population of carriers, compared to the higher temperature emission, which shows a propensity for the carriers to relax down to the lowest energy possible, favouring the deeper potential provided by longer-wavelength QDs. In other words, the carriers at low temperature are less affected by the energy difference found in the variation in a standard distribution of QDs. As a result, the emission from a QD ensemble resembles that of the standard distribution. As the temperature increases, the carriers have more energy, meaning that they have a higher probability of escape from a confined structure. The QDs with a deeper confining potential (and lower energy) capture

the most carriers as a result, meaning that emission is more prevalent from a lower energy.

An Arrhenius plot can also be created using the data from a temperature dependent PL experiment- using the natural log of the integrated intensity of the PL vs. the inverse of the PL temperature. Looking at InAs/GaAs QDs, there appears to be a thermal quenching above a certain temperature, which is dependent on the excitation and the capture and escape of carriers in the QDs[24]. As described in Le Ru's paper [24], QDs exhibit a standard Arrhenius plot, with three distinct regimes:

a) Low Temperature Regime, where the integrated PL remains constant. This is due to the low temperature allowing efficient carrier capture and subsequent recombination.

b) Regime of Strong Thermal Quenching, where the plot tends towards linearity, with the function of the straight line being proportional to E_a/kT (E_a is the activation energy, k is the Boltzmann constant and T is the temperature in Kelvin). This quenching is due to the thermal escape of carriers into the surrounding barriers, resulting in non-radiative recombination.

c) Intermediate Regime, where the integrated PL is between the two regimes, and can exhibit some unusual behaviour. This is the elbow as seen in figure 3.1.7, and demonstrates a reduction in integrated PL intensity, but is not yet in the exponential regime. Unusual behaviour exhibits itself in the form of kinks in the shape of the plot, attributed to many causes, such as individual carrier escape as well as the redistribution of carriers due to the preferential thermal escape from smaller, high energy QDs. Once the carriers escape the high-energy QDs, recapture into larger, emission from lower energy QDs occurs.

Regime b) allows for an estimation of the activation energy in the QDs, provided the curve has reached the linear regime. This can be determined by estimating the barrier height of the QDs, which is calculated as the difference between the band gap of GaAs and the PL emission energy. Using the results from Figure 3.1.6, it is possible to create an Arrhenius plot, in order to calculate the activation energy.

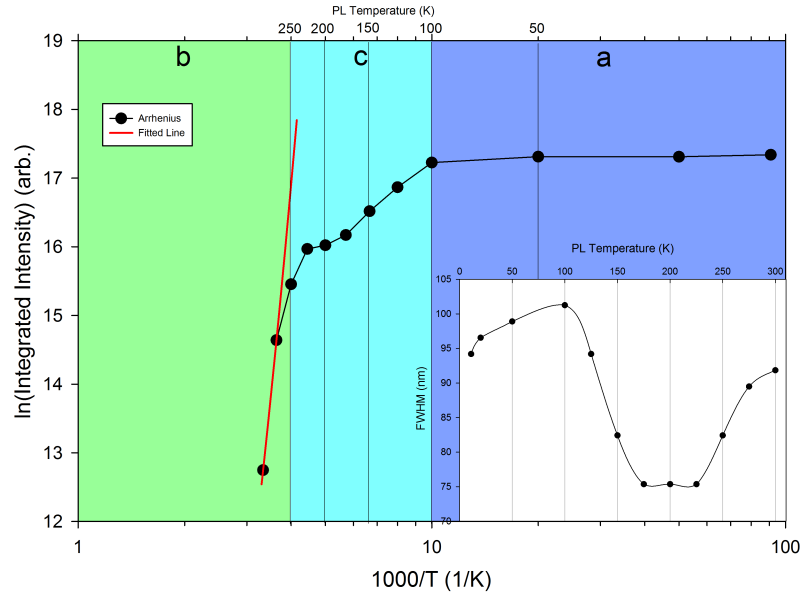


Figure 3.1.7: Arrhenius plot with fitted line for activation energy calculation. Different colour regions correspond to regimes as described in [24]. Inset plot shows the temperature dependent response of the FWHM of the QD sample.

The gradient of the fitted line as shown in figure 3.1.7 yields an activation energy of 54 meV. If this is compared to the calculated barrier height (GaAs-QD ground state energy) of 366 meV, there is nearly an order of magnitude difference between the two, meaning that the temperature of the PL was not able to accurately describe the activation energy. A number of experimental reasons contribute to this, noting that the experiment as performed, was not designed to yield the activation energy, but rather the sample's response to the change in temperature. Firstly, the excitation density is key- if the QDs are excited beyond the onset of the first excited state, Pauli blocking affects the integrated intensity of the PL emission. Also, the sample used is not ideal. Le Ru et al. [24] describe the necessity of delimiting the active region using barriers, in their case an AlGaAs/GaAs superlattice. A number of samples used in this thesis use AlGaAs barriers to enhance carrier capture, this one does not. As a result, the carrier generation from the GaAs is dependent on the diffusion of carriers, which in turn is dependent on material quality, temperature and surface quality. In addition, the temperature of the experiment may not have reached high enough temperatures- one of the samples in Le Ru's paper [24] required measurement up to 330 K. The

combination of these three uncertainties mean that the result yielded from the Arrhenius plot is expectedly inaccurate.

Note that the plot otherwise follows the shape as described by Le Ru [24], with each regime accounted for- the flat, constant area corresponds to a), the slope as measured corresponds to b), and the unusual corner with an indistinct shape corresponds to c). This corner also corresponds to the unusual behaviour of the linewidth as the temperature rises. This linewidth behaviour mimics that seen in the paper by Nee et al [33], which is attributed to thermally-enhanced carrier relaxation: as the temperature increases, carriers migrate to the WL where they are re-trapped and recombined in lower energy QDs, as mentioned previously. This process limits the size distribution of the QDs that are emitting, meaning that the FWHM is reduced. The process is described in figure 3.1.8, where GS refers to the ground state of the QDs, X_1 and X_2 are excited states in the QDs, and WL represents the ground state of the wetting layer. The process as seen- 1 represents carrier escape into the wetting layer, 2 represents carrier capture by the wetting layer, 3 represents re-capture by the deeper QD, and 4 represents recombination in the deeper QD. Note that figure 3.1.8 is simplified and certain aspects are exaggerated for clarity. The subsequent increase in the FWHM is attributed to electron-phonon scattering [44] similar to the broadening seen in QWs as a result of LO phonons [12].

3.1.1 Bimodality of quantum dot ensembles.

In each of the PL spectra shown, the shape of the spectra deviates from a gaussian shape on the high energy side. This is predominantly due to a result of 3D SK growth of InAs having two thresholds: the first is the 2D-3D growth threshold, at ~ 1.7 ML, the second is the transition between two QD shapes, which doesn't appear to have a corresponding, easily-defined, deposition-based threshold, instead relying on the individual QDs, and the chemical potential of the growing material [23]. The second transition means that there are two separate families of QDs, and as the linewidth and shape of the PL spectrum depends on the distribution of QDs, the PL spectrum is broadened.

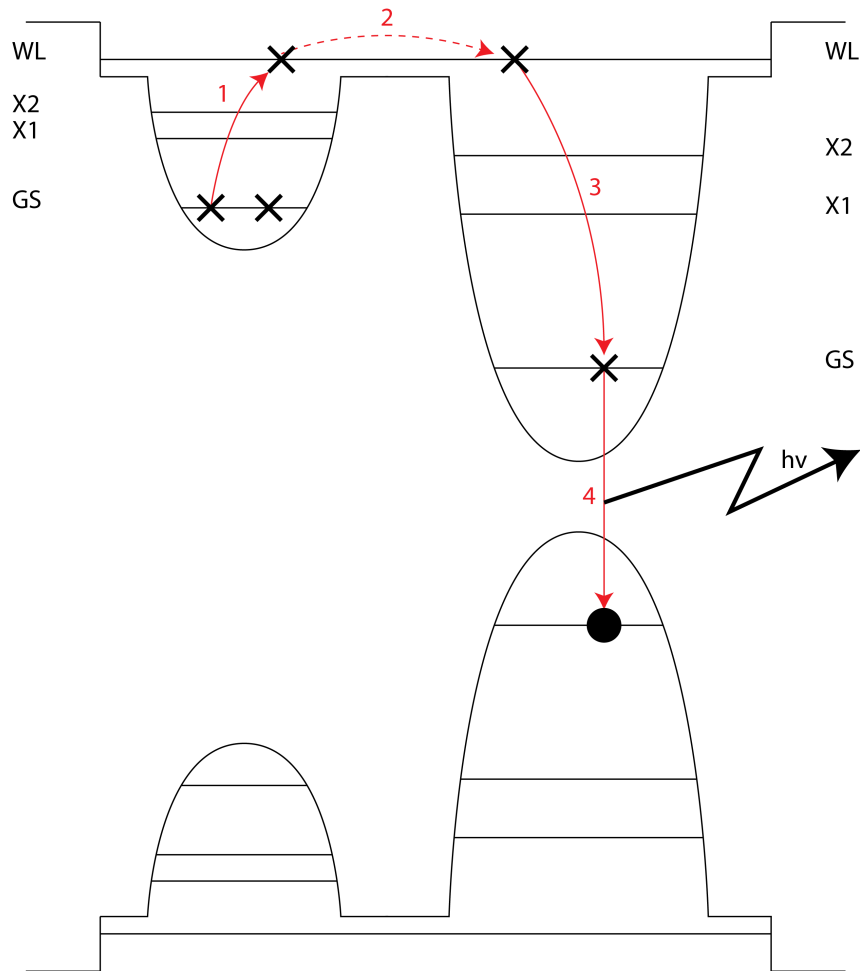


Figure 3.1.8: Simplified diagram of carrier recapture in WL and QDs.

This was first noted in the Ge/Si (1) system, with the comparatively larger QDs being extensively examined by Medeiros-Ribiero, Rastelli and Tomitori [30, 34, 38] among others. These studies found a change in the shape quantum dots, with the smaller, less mature dots being comparatively simpler, with fewer facets, resembling a square based pyramid, and the larger, domed dots having rather more complex faceting. Analysis of structure and composition of InAs QDs was met with rather more difficulty, with initial interest in multiple families of QDs being shown by Brusaferrri et al. [4]. Numerous studies follow, using AFM [17, 25, 26, 41, 42] and PL [32, 35, 41], with modelling from Daruka et al [7, 8]. Studies of note include that of Guo et al. [17], who showed that bimodality isn't limited to one crystal orientation, and Mukhametzhanov et al. [32], who compare the PL

and AFM of bimodal samples, showing that InAs/GaAs QDs come close to completing the second transition after approximately 2.5 ML of deposition.

Constantini et al. [5, 6] bridge the gap between InAs/GaAs and Ge/Si growth systems, with a thorough description of the faceting of the different shaped islands with the aid of STM. This analysis is reproduced in figure 3.1.9, adapted from [5].

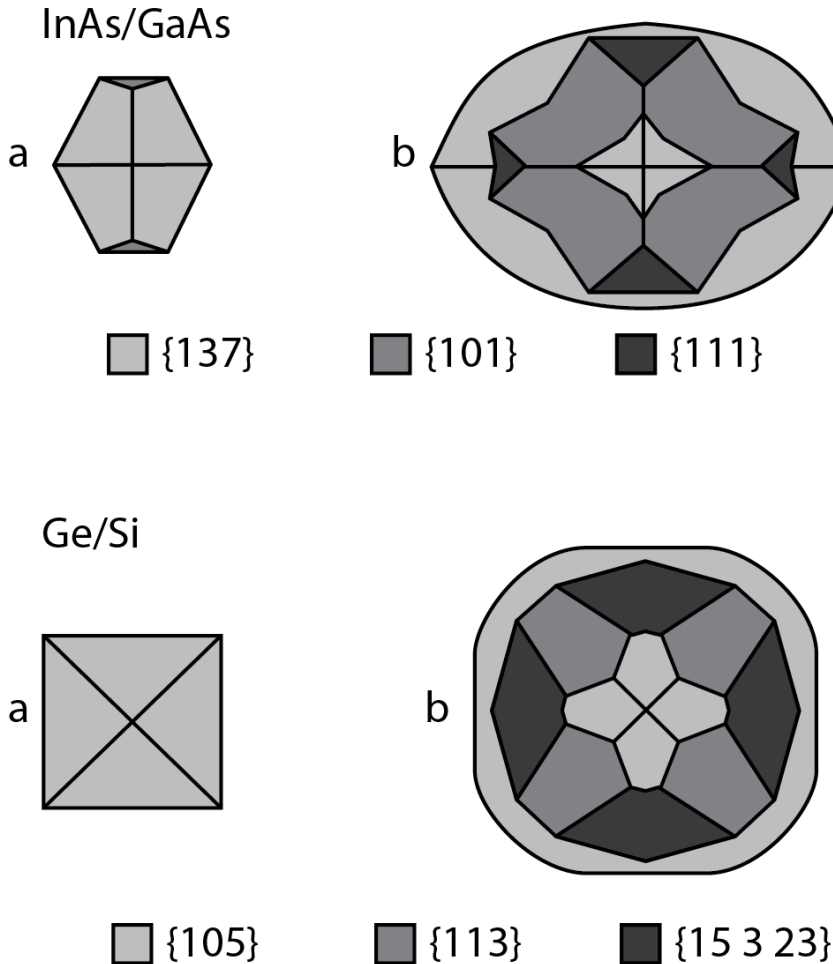


Figure 3.1.9: Bimodal QD Growth Analysis based on figures from Constantini et al[6] showing a simple graphical representation of the faceting for both material systems and different types of island. a) represents the “pyramid” shape and b) represents the “dome” shape for each material system.

In terms of the growth, Montalenti et al, Zela et al, Johansson et al and Kratzer et al. [19, 23, 31, 47] determine that, prior to dislocation, InAs QDs reach a limit in terms of base width, meaning that growth after the pyramid shape is a top-to-bottom process. Kratzer et al. [23] describes the thermodynamic stability of the growing islands determining their shape, with the smaller dots having predominantly {137} facets due to these being energet-

ically more favourable at a smaller size, with the larger dots developing a “domelike shape on top of a flat base as the island grows larger”.

This observation of two families of QDs for typical InAs/GaAs QD growth affects this thesis due to the majority of characterisation coming from PL, AFM and variants thereupon. As Mukhametzhano et al note [32], the split in the two families of QDs is reduced at approximately 2.5 ML, with most QDs having matured to domes. In order to try and reduce dislocations, however, growth performed for this thesis is typically less than 2.4 ML, meaning that a bimodal element will have to be considered.

3.2 Quantum Dot Growth

3.2.1 Wavelength Control: Indium Coverage Control

The wavelength of the emitted light is related to the dimensions of the quantum dots, with the smallest dimension defining the lowest energy state and therefore the ground state wavelength. The smallest dimension of a typical InAs/GaAs self-assembled quantum dot is the height, or rather the dimension in the direction of growth. There is a limit to the height of quantum dots before they dislocate, rendering them useless in an optical capacity. Up to this point there is an ability to control the height by controlling the growth time. This is not the most controllable method due to the material deposited not following a simple growth rate: 3 dimensions of growth must be taken into account, not simply the usual vertical direction as is the case with quantum wells, with the shape change also causing a complication in the growth rate calculation. The quantum dot base diameter is primarily related to the growth temperature [20, 21], and reaches a limit before the shape transition. It also relates to the QD density, with a large density relating to smaller dots and vice versa; and the composition of the dots also influences lateral QD size. The second transition of dot growth itself, from pyramid to dome, requires another consideration that isn't calculable from simple growth rates- with Zela, Kratzer and Johansson [19, 23, 47] describing the process of growth after pyramid formation as being top-to-bottom and slowing considerably, due to the highly compressive strain at the base

making the attachment of further InAs to the base of the QD energetically unfavourable. This two-stage growth process means that any control of QD emission using the InAs growth duration is rather more complex compared to the growth of a 2D structure.

A set of samples was grown, varying the length of the InAs deposition time for each growth run, causing the InAs deposition to range from 1.56 ML to 2.53 ML. This set of samples had an AFM layer of quantum dots for analysis as an indication of the lack of variation as In deposition changes. Figure 3.2.1 and 3.2.2 show the statistics of the heights of the quantum dots for each of the coverage samples, with figure 3.2.3 showing an example of the AFM images used for each sample. The statistics calculated use per-square-micron values, as multiple scans from different locations on the sample were used to attain the data. The increasing letters correspond to the increasing In coverage values, with A = 1.75 ML to E = 2.53 ML.

This data shows an apparent lack in change after the onset of 3D growth. There is a consistent trend through each sample, with the largest number of dots having a height of 12 nm for all but one sample (1.95 ML). As the indium coverage increases, larger dots appear with greater frequency, with the “other” column referring to “mega-dots”, which are dislocated, over-mature QDs. Examples of mega dots are shown in figure 3.2.3 c and e. It would appear, therefore, that the QDs have a tendency to settle at a height of approximately 12 nm. Extra material appears to be sparingly spread amongst the dots on the higher coverage samples, with “mega-dots” appearing in those samples, which have height values up to 50 nm, with the smaller dots slowly disappearing as the coverage increases, instead of the number of QDs increasing, or the overall QD population growing in size. This is shown by the median values- starting at 9 nm for the 1.75 ML sample, it rises steadily to 12.5 nm by the 1.34 ML sample, indicating a dearth of smaller dots. This appears to agree with Barabási’s paper [3, 9], as well as earlier descriptions of QD shape transition behaviour. One limitation of QD growth, as discussed previously, is the base size, which is limited by the very large compressive strain field at the base, making any additional material growth at this point energetically unfavourable [19, 23, 47]. In fact, Barabási [3, 9] states that the strain field lowers the energy barrier for diffusion, making “diffusive hops”

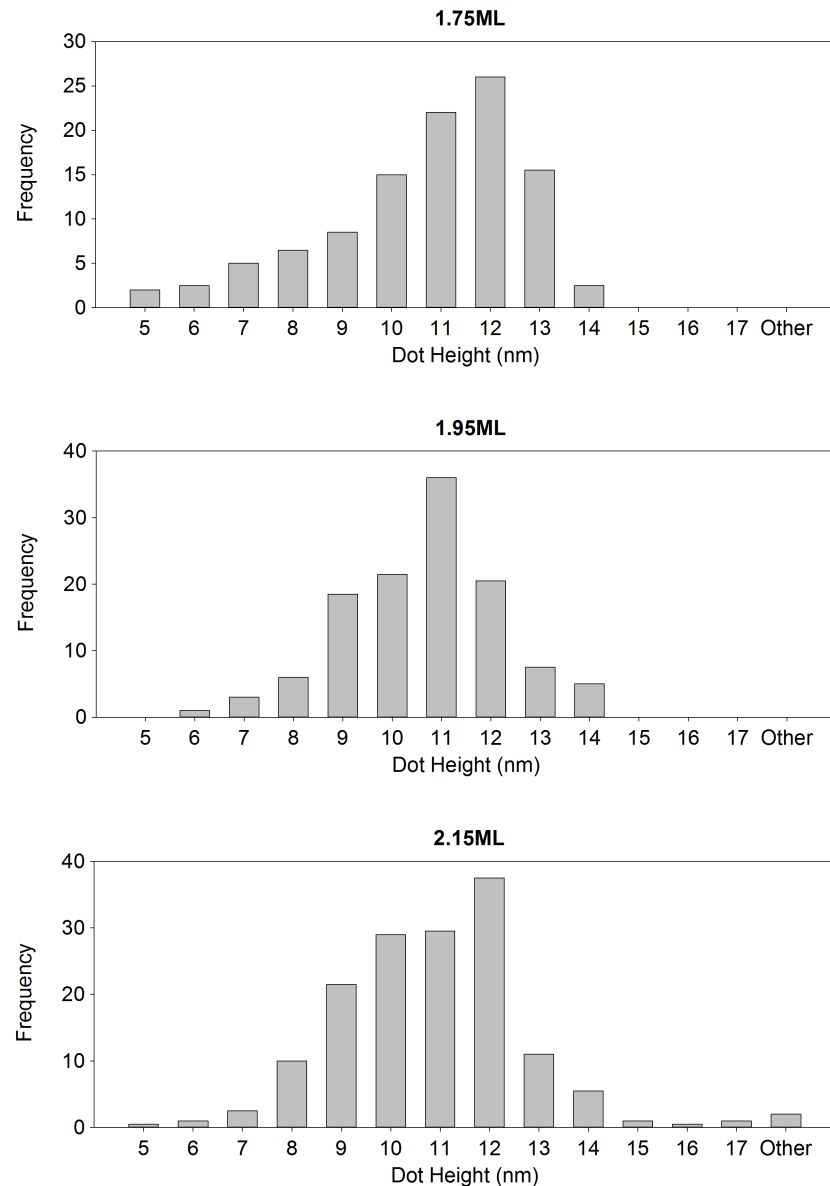


Figure 3.2.1: AFM statistics of coverage samples: Samples shown are 1.75ML, 1.95ML and 2.15ML.

more probable; that is deposited atoms are less likely to remain in an area of high strain. In addition, strain energy becomes comparable with that of the bonding energy of an atom at the edge of a growing QD, meaning that the size of QDs are homogenised laterally, and leads to islands reaching a certain size and then stopping, encouraging growth of the smaller islands. This can lead to, in ideal growth situations, a better homogeneity in dot size.

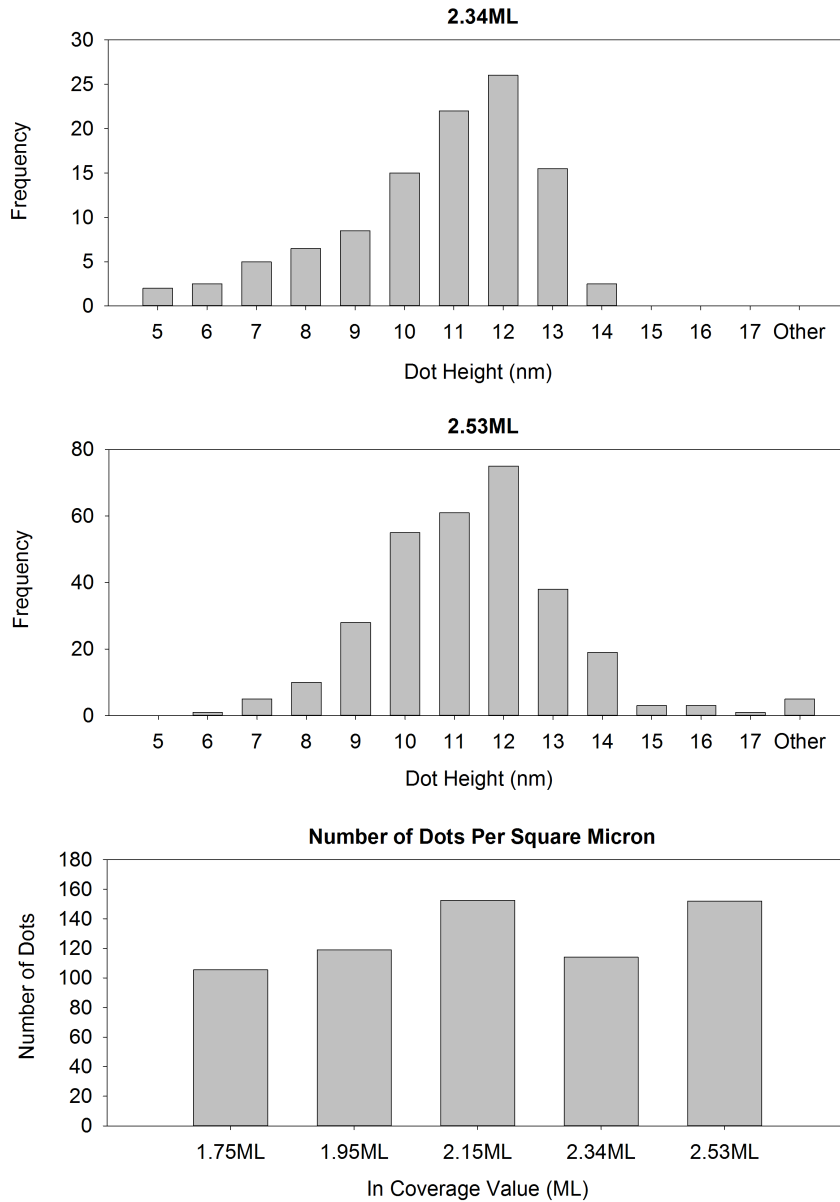


Figure 3.2.2: AFM statistics of coverage samples: Samples shown are 2.34ML and 2.53ML, with additional statistics regarding the number of quantum dots per unit area.

The dislocated “mega dots” that appear on certain scans, and increasingly in the samples with higher indium coverage, are dislocated QDs. The limiting factor of strain is removed by the dislocation in such an island, meaning that there are fewer restrictions to the base size as mentioned previously. This means that indium is much more likely to accumulate on these so-called mega dots, and that the over-ripening of QDs is limited by the in-

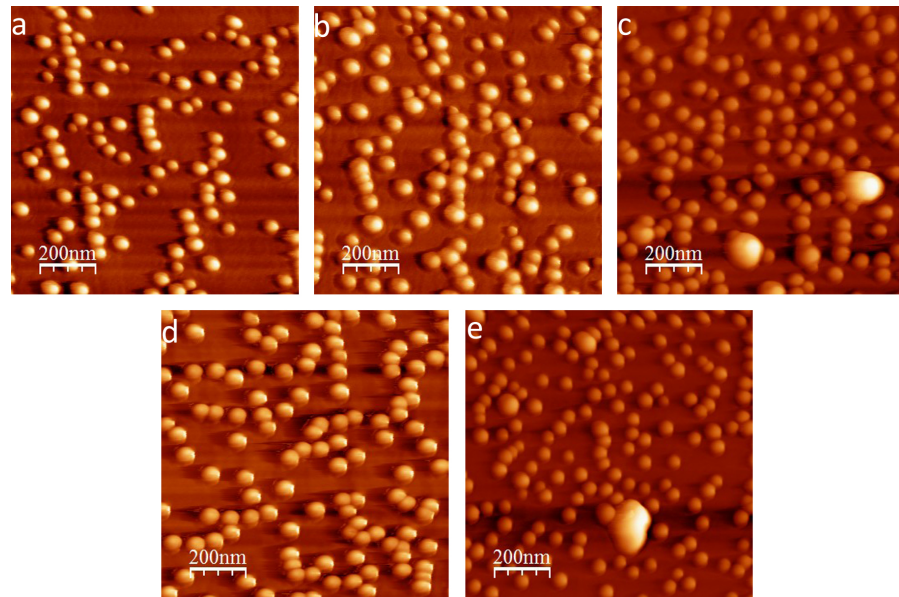


Figure 3.2.3: Example AFM of coverage samples for analysis- multiple images were used for the statistical analysis, these are representative of each sample.

dium preferring the few dislocated dots compared to the increasingly stable undislocated dots.

3.2.2 Wavelength Control: Indium Flush

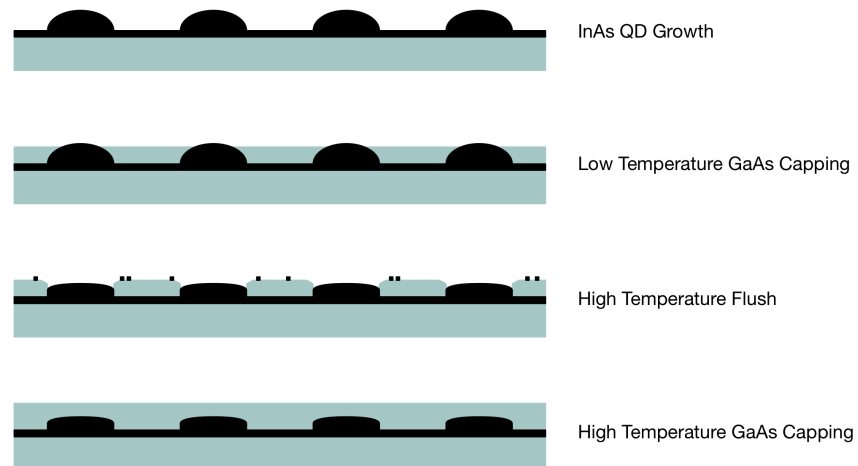


Figure 3.2.4: A step-by-step basic overview of In-flush QD growth.

A more precise method of dimension control is the indium flush growth method. This method uses the InAs/GaAs material system, partially capping the InAs islands with 2D GaAs growth- a process that is controllable to

an accuracy of Ångstroms, and takes advantage of the propensity of indium to desorb from a substrate at higher growth temperatures (typically higher than 540 °C [15]), with the typical growth temperature of GaAs (~660 °C) providing a sufficiently high temperature. In this way, other parameters such as density, or the number of QDs per unit area (based on growth rate) and dot base size (based on growth temperature) can be controlled separately to the height (and by definition wavelength control). Figure 3.2.4 shows an overview of the the In-flush technique. In greater detail, the low temperature GaAs cap after the deposition of the quantum dots is only completed to a specified height, less than that of uncapped dots (typically up to 10 nm). After this, the substrate is heated to a higher temperature, usually to that of the typical GaAs growth temperature, at which point any exposed InAs is desorbed from the surface, leaving only the InAs below the partial cap. GaAs growth is then resumed to “lock” the height-reduced QDs in place, giving a greater homogeneity of the QD height, thus reducing the linewidth. The wavelength is controlled in this way by reducing the height- the shorter the cap, the shorter the wavelength emitted. Note that the demonstration diagram in figure 3.2.4 does not show the post-capping collapse of quantum dots as noted by Garcia et al [13].

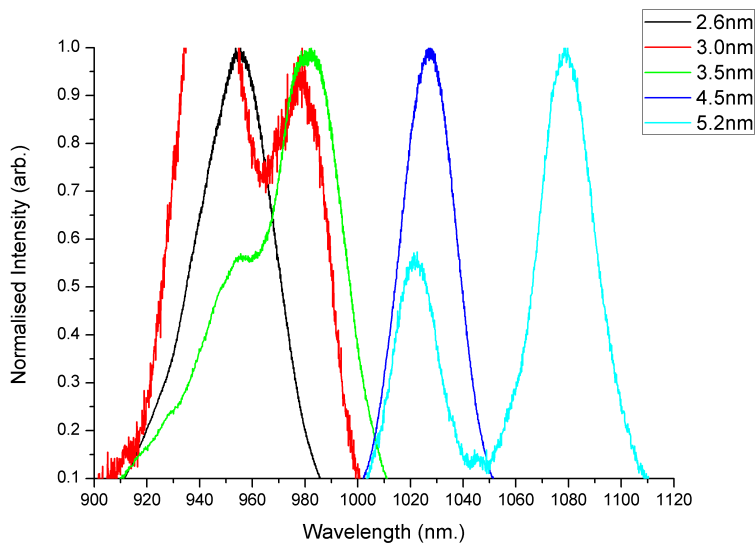


Figure 3.2.5: Comparison of samples with different GaAs cap heights

Figure 3.2.5 shows edge PL comparison of a set of samples that differ in the height of the low-temperature GaAs cap, as noted on the legend. This measurement was taken at 4 K in a liquid-helium cooled cryostat. The initial aim of the experiment was to determine the difference between the TE-TM ratio if the cap height was changed, although results showed minimal change in the TE-TM ratio between samples. The data collected can be viewed in appendix A. However, the data does clearly show the difference of 5.2 nm to 2.6 nm cap allows for a change in wavelength from ~ 1080 nm down to ~ 955 nm, with each step in cap height corresponding to a change in wavelength. The 3 nm PL peak is affected by the difficulty of the edge PL measurement- focusing not on the sample surface, but the edge, which, in this case, has led to a small number of dots being excited, leading to state filling, and the first excited state being more intense than the ground state. This is as a result of the focal point of the excitation laser being at a particular point that excites fewer dots.

This run of samples demonstrates the capability of the In flush method in controlling the wavelength between 1100 nm and 950 nm at low temperature, meaning that QDs can be tuned to wavelengths suitable for detection with high-efficiency Si detectors for single dot studies, as is demonstrated later in this chapter.

3.2.3 Wavelength Control: DWELL/InGaAs Capping

The wavelength of quantum dots grown with InAs and subsequently capped with GaAs in a GaAs based structure typically emit between 1100 nm and 1300 nm at room temperature. For telecommunications, two wavelengths are targeted- 1300 nm, corresponding to the dispersion minimum for signals propagating along standard optical fibre, and 1550 nm, corresponding to the attenuation minimum. This is outside the realm of standard InAs/GaAs QDs, which emit at around 1100 nm. In order to remedy this problem, the growth of the quantum dots is altered, again by capping, this time with InGaAs instead of GaAs, with a variant enclosing the quantum dots in an InGaAs QW, known as a DWELL structure. This variant of quantum dot growth can extend the wavelength to 1300 nm due to the surround-

ing cap/underlying layer suppressing indium segregation and reducing the high-strain field of the quantum dots which reduces the post-capping-collapse [29], maintaining the majority of the uncapped height and thus reducing the ground state energy in the QDs and causing a redshift up to approximately 1400 nm at room temperature [39]. This will be the focus of one of the main results of this thesis, presented later in this chapter, to extend the low temperature emission of single QD devices to 1300 nm, suitable for telecoms applications.

3.2.4 *Wavelength Control: Post-Growth Annealing*

Another method of wavelength control can be achieved outside of the growth chamber. Post-growth annealing is used not only to alter the wavelength, but to improve the characteristics of the emitted light- the profile of the emitted light is defined not only by the intensity of the emission, but the width of the peak, known as the line-width. For lasers in particular, it is particularly desirable to have a narrow line-width, so the ability to precisely control the wavelength and line-width is particularly useful, especially after the growth has occurred. It may be noted that this process is irreversible.

Processing a sample in this manner requires an inert atmosphere to avoid oxidation or other potential reactions, as well as a proximity cap made from a III-As material to avoid preferential desorption of Arsenic at higher temperatures. The sample to be processed is placed in a Rapid Thermal Annealer (RTA), where it is heated to a desired temperature for a desired time under a nitrogen atmosphere, whilst being sandwiched between GaAs wafers.

When annealed, emission from a quantum dot sample is not only blue-shifted, but the intensity of the emitted light increases, with the line-width being reduced also [27]. This is due to the high temperature allowing the interdiffusion of indium and gallium within the grown crystal lattice [28], which in turn causes a change in the material, and therefore strain and confinement of carriers. The increase in intensity is due to an amelioration of the crystal quality, as an example, removing interstitial defects that reduce the luminescent efficiency of such a material. There is a three-stage process

in this high temperature diffusion, the first being a rapid re-alignment of the crystal, usually correcting any defects present in the material [22], with atoms within the lattice gaining sufficient energy from the increase in temperature to rearrange themselves into a more energetically favourable position. The second stage is diffusion that adheres to the Fickian model [22], and the diffusion process is slowed in comparison to the first stage. The third stage is essentially a continuation of the Fickian diffusion but is after the limit of positive change on the structure, and results in a diminishing of the quality of the optical emission. Malik [27] and Xu [43] attribute this to a degradation of the optical material, with Xu [43] showing evidence of this by TEM. The confining layer appears to have diffused completely, meaning that there is no longer a confined structure for carriers to recombine efficiently in.

3.2.4.1 Experimental Work

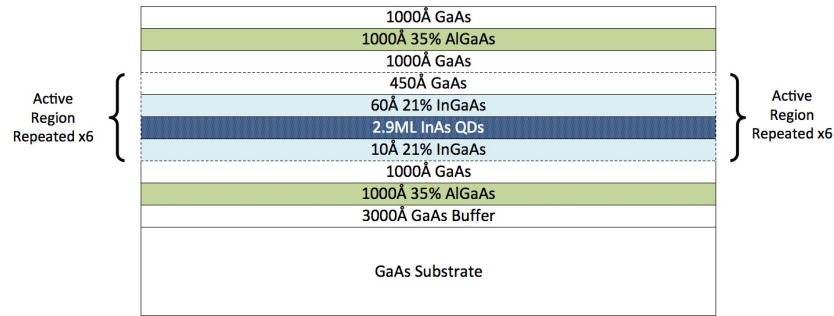


Figure 3.2.6: Initial sample structure used in annealing experiment

Time (s)	Anneal Temperature (°C)
Control	Control
30	750
30	800
30	850
60	850
90	850
120	850

Table 3.2.1: Anneal steps for initial anneal experiments

In order to tune a number of grown quantum dots samples, annealing processes were investigated to test the limits and attempt to optimise the an-

nealing process. For the first experiment, a sample whose structure is shown in figure 3.2.6 was used, due to the sample exhibiting poor linewidth and emission characteristics as a result of a very broad ensemble of QDs. Figure 3.2.7 shows the power dependent PL of the sample in question, noting that the two peaks are not only the ground and excited states, but instead two distinct families of dots- a particularly poor quality bimodal sample, as is shown in the normalised figure 3.2.7b), with the higher energy emission changing at the same rate as the lower energy emission when the power is varied, indicating the majority of emission is from the ground state of the two families of quantum dots.

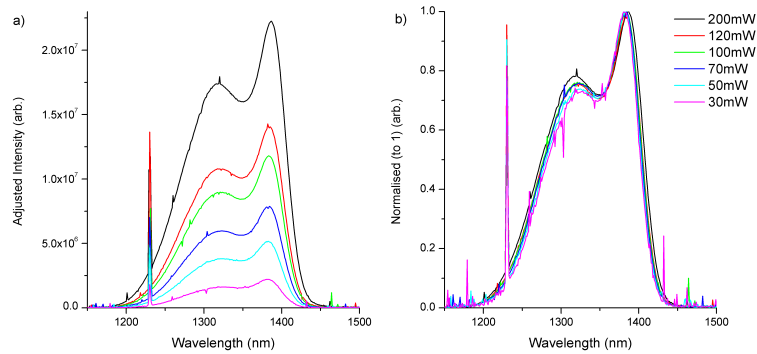


Figure 3.2.7: a) Power Dependent PL; b) Normalised Power Dependent PL

The wafer was cleaved into 5 mm square pieces and annealed as per table 3.2.1, noting that the individual pieces were annealed only once.

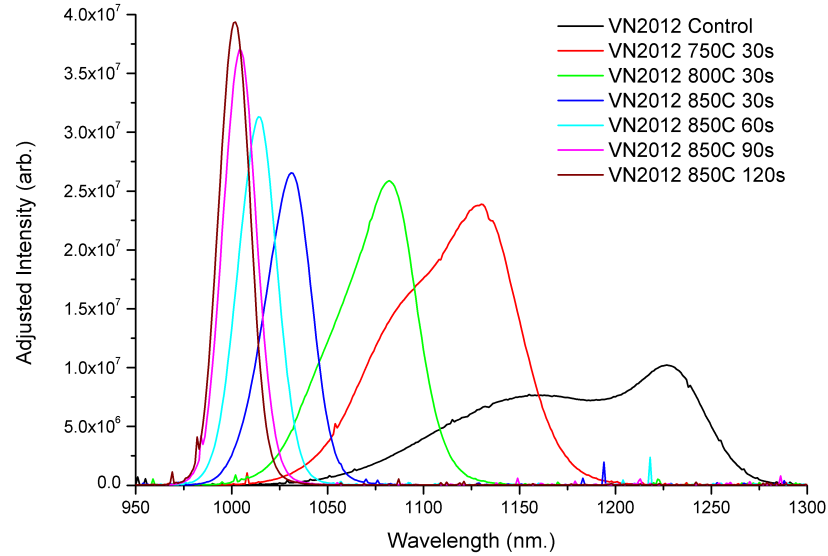


Figure 3.2.8: PL of annealed samples

Figure 3.2.8 shows the change in emission after the anneal steps. In order to quantify the change in the emission from the sample, various properties of each individual spectrum were taken, and compared in figure 3.2.9.

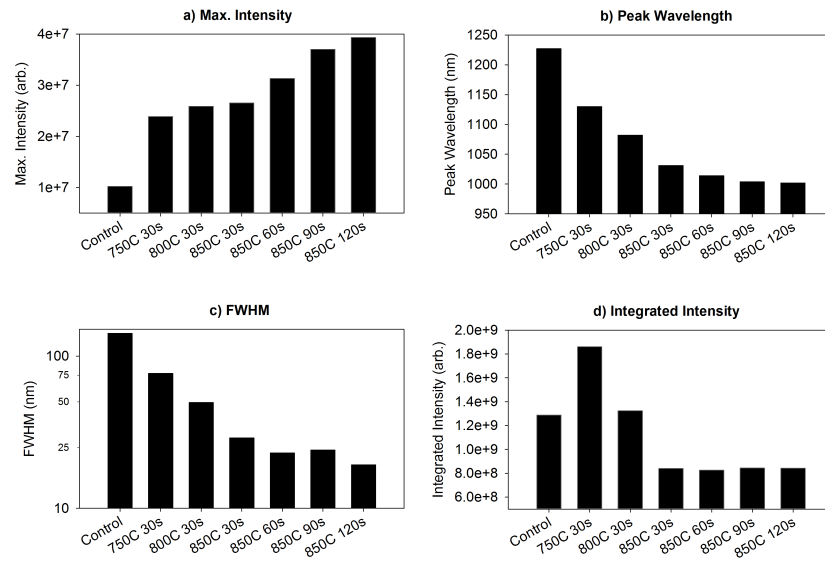


Figure 3.2.9: Statistics from the annealing of the sample described in figure 3.2.6

Figure 3.2.9 shows the change of a number of parameters, which seem to corroborate the earlier observation that there is a large change in the lower temperature anneals before tending towards a particular value. Malik et al[27] note that after a certain point, the anneal causes degradation of the

dots resulting in lower emission, but the maximum temperature and time attained in this experiment don't appear to be sufficient to cause significant adverse effects in the PL emission, with intensity continuing to rise and the FWHM continuing to narrow. The peak intensity (figure 3.2.9a)) shows a considerable increase, even after the first anneal step, although given that the unannealed sample is extremely bimodal, this is not the best comparison. After the initial rise, the rise in intensity continues, albeit at a slower rate. The wavelength (figure 3.2.9b)) appears to tend towards ~ 1000 nm, with the FWHM (figure 3.2.9c)) appearing to self-limit in a similar fashion, tending towards ~ 15 nm, a significant improvement on the initial value. The FWHM shows a consistent narrowing from the control sample through to the final anneal, again tending towards a particular value, in this case, ~ 20 nm. The initial extreme narrowing is most likely due to the sample's bimodal emission coalescing into a single mode, meaning that the combined linewidth of two families isn't taken into account. The integrated intensity of the samples is measured in the final panel (figure 3.2.9d)), with the lowest temperature anneal showing the largest value for the integrated intensity, dropping after the anneal seemingly reaches the second stage, as described by Kobayashi et al. [22].

The emission from the ground state of the quantum dots is typically Gaussian in shape, following the standard distribution of sizes of a QD ensemble (this also holds true for an individual distribution in bimodal QDs). An approximation of the FWHM (Full-Width, Half-Maximum) for the individual spectra is calculated using the Gaussian approximation for each, allowing for a quantifiable description of the change in the line-width and other properties of the lower-energy QD family (Figure 3.2.10).

As the anneal progresses, the bimodality of the sample reduces. In order to quantify this change, the proportion of the low energy gaussian to the total PL is taken. In addition, a second gaussian is fitted to the population of QDs emitting at a higher energy in an attempt to quantify the homogenising of the dots as the anneal temperature and/or time is increased (figure 3.2.11). This was done across the entire range of results, but only the results from the unannealed and first three annealed samples are shown due to the

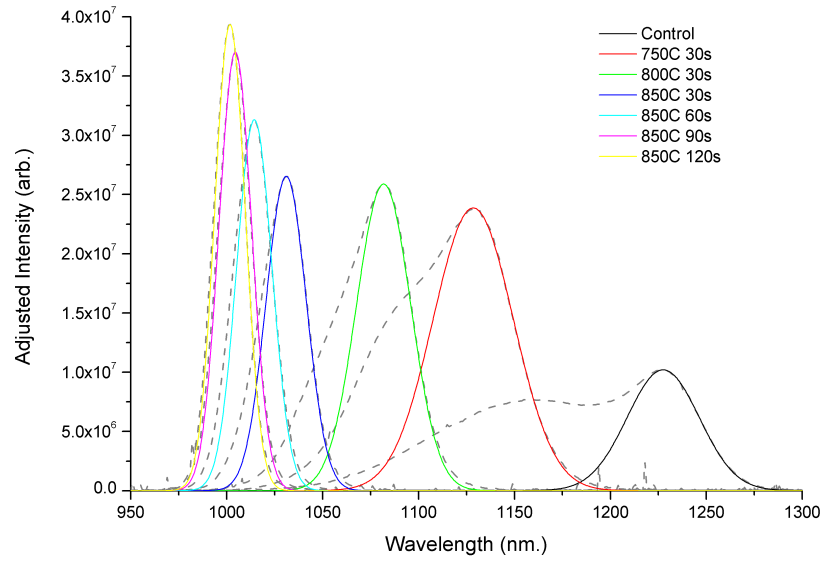


Figure 3.2.10: Fitted Gaussian Curves (colour) with PL Spectra (grey) of vn2012

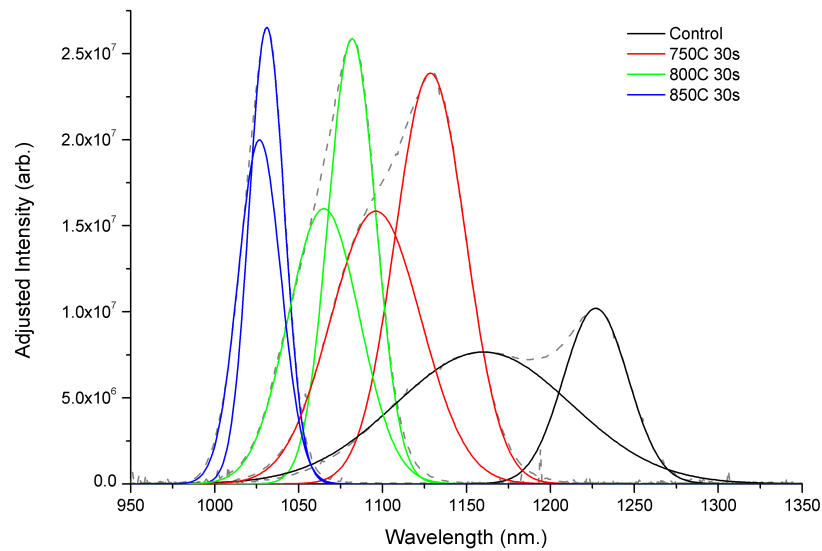


Figure 3.2.11: PL with high energy Gaussian fit

latter samples having little-to-no high energy shoulder, and the high-energy gaussian thus being made redundant.

Figure 3.2.12 shows the effects of the anneal steps on the fitted Gaussian curve of each family of QDs. The higher energy Gaussian is less accurate as the samples progress, due to the peak attributed to the higher energy dots being swallowed by the overall PL spectrum. Figures 3.2.12a) and b) are showing the FWHM of the low- and high-energy Gaussian curves. Both

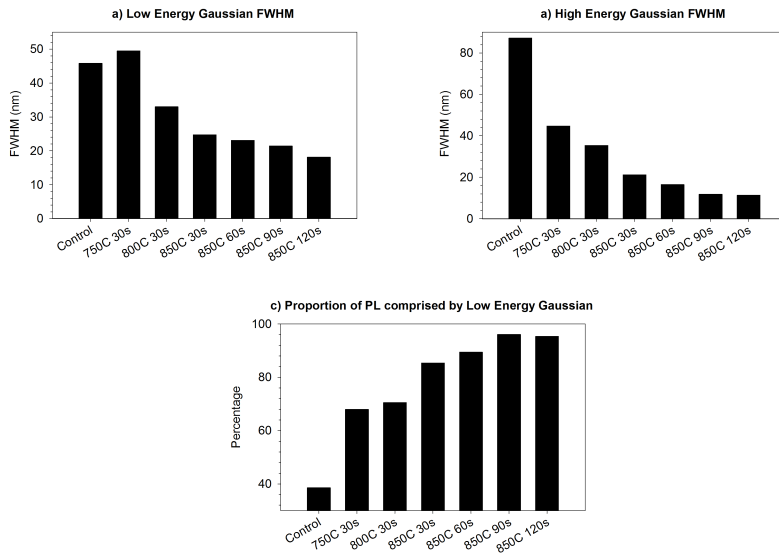


Figure 3.2.12: Statistics of high- and low-energy fitted Gaussian curves.

show an overall decrease, but the massive change in the high-energy curve indicates diminishing in the population of that family of QDs. This may be due to the larger dots having a lower In concentration, and being less ready to diffuse compared to the smaller, more concentrated dots. Figure 3.2.12c) shows the amount of the integrated PL that is comprised of the low-energy Gaussian, as an attempt to quantify the bimodality of the sample. This value appears to level out at approximately 95 %, showing a considerable improvement over the unannealed sample. This indicates that the indium layer, and indeed dot size, is homogenising, creating a more even distribution, with the increase in intensity indicating an improvement in the crystal quality.

3.2.4.2 Further Experimental Work

500Å GaAs
500Å 35% AlGaAs
150Å GaAs (VN2065) 100Å 21% InGaAs (VN2070)
2.9ML InAs QDs
150Å GaAs (VN2065) 100Å 21% InGaAs (VN2070)
500Å 35% AlGaAs
2000Å GaAs Buffer
GaAs Substrate

Figure 3.2.13: Sample Structure for VN2065 and VN2070 (Second anneal experiment)

Time (s)	Anneal Temperature (°C)
Control	Control
30	700
30	725
30	750
30	775
30	800
30	850
60	850
90	850
120	850

Table 3.2.2: Anneal steps for second anneal experiments

New samples were grown, to further investigate the anneal process, with a decision made to keep the indium deposition the same for each sample, but alter the capping material (figure 3.2.13). The samples only use single quantum dot layers, and the anneal processes were more thorough in terms of the temperature steps for annealing, to investigate the first stage of the anneal, with the linewidth of the unannealed samples significantly smaller compared to the previous bimodal sample, although vn2070 exhibited slight bimodal behaviour.

Again, each sample was cleaved into 5 mm square pieces and annealed simultaneously. Unfortunately, a harmonic of the excitation laser was coincident with the PL spectroscopy results as shown in figure 3.2.14, but the results still show a blueshift, intensity increase and line-width decrease.

Each of these PL spectra is taken at the same conditions with the same excitation source and power, at 11 K. The high energy peaks are the first and second excited states of the quantum dots, also an indicator that quantum dots remain in the structure after the anneal. This is also verified by the ratio of the ground state (GS) and first excited state (X1) being approximately constant across the samples- there is a degree of variation, but it appears to coincide with the variation of the GS/X1 ratio at different excitation powers across the annealed sample set. This also indicates that a similar number of QDs are being excited throughout the experiment, meaning that no QDs are being “lost” in the anneal process.

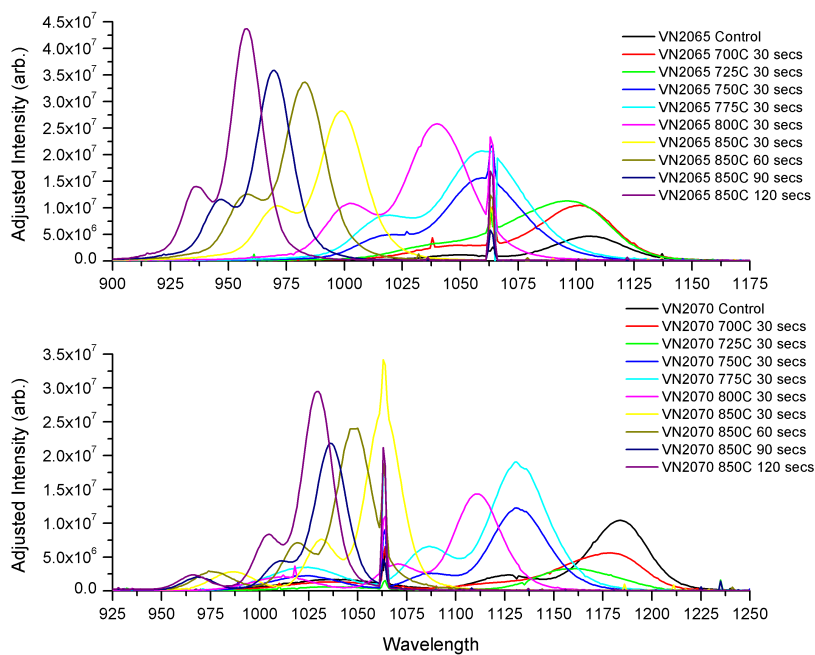


Figure 3.2.14: PL Spectra from Second Anneal Experiment

It seems that there is a gradual change in wavelength from 700 °C to 725 °C, with the peak’s main change being intensity. After that a major change occurs at the 750 °C stage, with only a ramp in intensity seen at 775 °C. The main change in peak wavelength appears to occur between 775 °C and 850 °C. This is more clearly seen in figure 3.2.17a, where the wavelength appears to change in steps, from 725 °C to 750 °C, and 800 °C to 850 °C. The change in maximum intensity appears to be a straightforward increase, when looking at the results from VN2065, but there was slight difficulty in obtaining an accurate maximum intensity value for VN2070 due

to the interference from the laser harmonic at the peak wavelength value, hence the value being attained through the fitting of Gaussian curves to the PL spectra (figures 3.2.15 and 3.2.16).

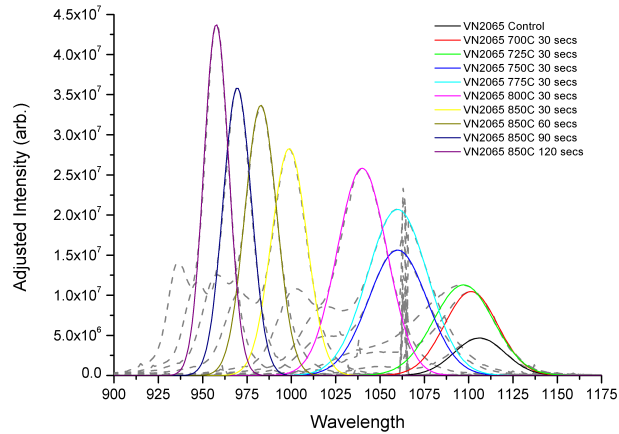


Figure 3.2.15: Fitted Gaussian Curves (colour) with PL Spectra (grey) of vn2065

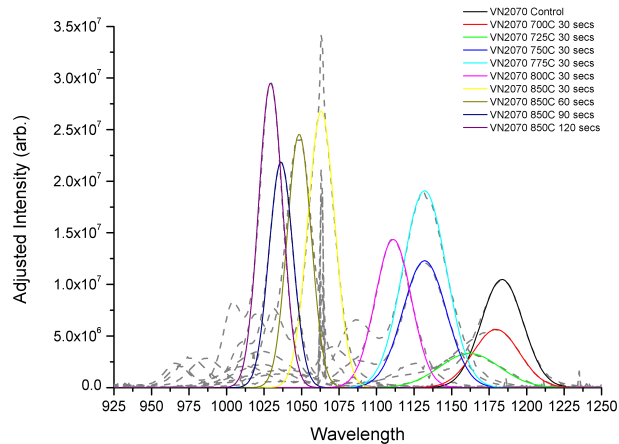


Figure 3.2.16: Fitted Gaussian Curves (colour) with PL Spectra (grey) of vn2070

There are two aspects of the anneal that are consistent for both sets of samples, being the reduction of the FWHM after an initial increase, and the blueshift of the spectrum. The reduction of the FWHM can be assumed to be as a result of the change in size of quantum dots due to the diffusion of Indium within the sample, and changes the dots in two ways: the material composition, and the size of the dots. The composition of the dots alters the emission due to the change in band gap as would be expected from

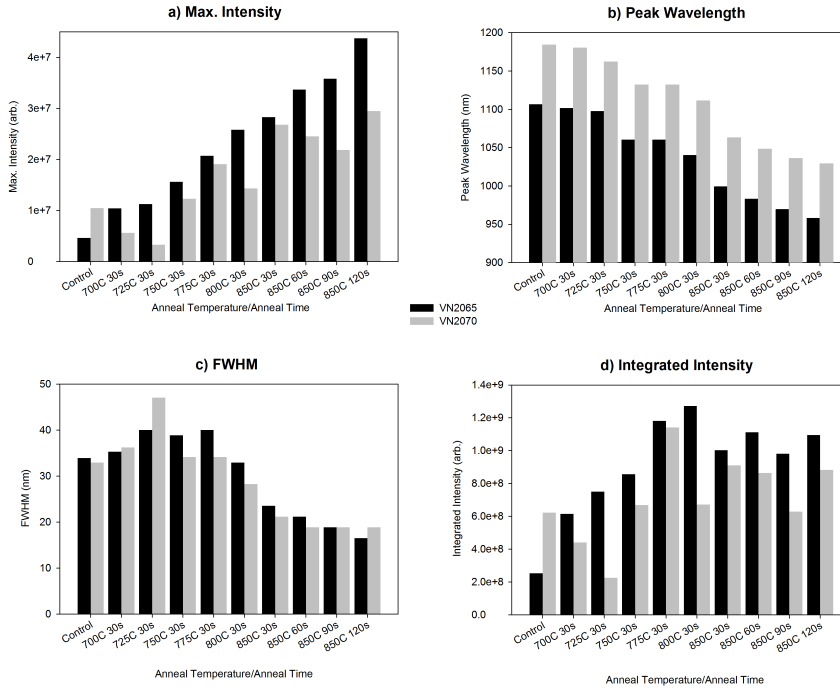


Figure 3.2.17: Statistics from the annealing of vn2065 and vn2070

a differing composition from growth. The size increase causes a change in the energy states in the dot^[36], and despite there still being a variation in the size of the dots, the overall size increase reduces the effect of the size distribution, due to the comparative similarity of the increased sizes relatively. This reduces the inhomogeneous broadening and therefore the line-width. The reason for the initial increase in line-width is may be due to the different rates at which the indium diffuses from dots of differing size and composition. As the indium diffusion evens across the dots, they reach a more uniform size/composition distribution and therefore, along with the size increase, the line-width is eventually reduced. As a result of the interference from the excitation laser, a comparison of the ratio of the fitted Gaussian to the PL would be misrepresentative.

Although a direct comparison is not possible due to the coincidence of the excitation laser harmonic and the samples' emission in the second experiment, both samples show an improvement in linewidth and intensity. The literature largely agrees with the experiments performed by this author. Overall, annealing self-assembled InAs/GaAs QDs results in an improvement in linewidth, and intensity with an overall blueshift in peak emission.

One thing that isn't shown by this work is the unusual behaviour that occurs at the lower temperature anneals, a subject that is the subject of contention between different studies. Below 750 °C, the anneal is said to undergo a mild red shift[14, 18, 37] with an initial increase in intensity, before a decrease at the 750 °C point, and where the peak wavelength starts to blueshift. There is evidence to dispute this, with different results showing a blueshift regardless of the anneal temperature[46], although the paper cited uses MOCVD-grown QDs, which are grown at a higher temperature compared to MBE-grown dots. The former results are attributed not to the interdiffusion of In/Ga, but the curing of the crystal which reduces the number of defects in the material[37]. The anneal steps taken in our experiments start at 700 °C minimum, which does not allow for a thorough investigation of this initial curing process. That being said, the InGaAs capped sample appears to show a reduction in intensity and only a small blueshift for the 700 °C anneal, an indication that it would behave as reported by Shin[37] in the initial stages. More work would need to be done to verify this, and to compare the difference between InGaAs capped and GaAs capped QDs at this early anneal stage. The bimodal samples' lowest anneal temperature was at 750 °C, therefore meaning that the potential redshift and subsequent blueshift with a degradation in intensity between 700 °C and 750 °C was not seen. Considering the large change in emission between the unannealed sample and the 750 °C anneal, it would be worthwhile investigating.

It may be noted that the InGaAs capped QDs show a slower rate of saturation for the intensity and blueshift, with the increase in both not appearing to level out even at the highest temperature/time combination. This may be due to smaller QDs having a much higher interdiffusion rate and a smaller blueshift tunability [16]. This would also explain the rapid change of the high-energy QD family in the bimodal sample, and the initial broadening and subsequent narrowing of the FWHM of the spectra. If different families of QDs are annealing at different rates, this would cause an overall broadening as the smaller QDs blueshift at a faster rate.

Strain is also said to have an effect on the diffusion process, therefore the capping material would have a large effect on the rate of interdiffusion- the

InGaAs cap would reduce the rate of interdiffusion compared to the GaAs capped QDs [45, 48].

3.3 Conclusion

This chapter demonstrates the sheer variation in QD properties that can be easily controlled by MBE growth. Demonstration of the ability to vary the growth of QDs to match various different standards, including QD density, target wavelength and line width was shown at the beginning of the chapter. Analysis on post-growth tuning techniques showed promise, with more work needed to analyse the intermediate anneal interdiffusion process, although excellent reduction in linewidth and improvement in intensity was shown.

This chapter also showed the effect of the complex InAs/GaAs SK growth mechanisms on many properties, particularly light emission. The bimodal growth and variation (or lack thereof) depending on In coverage has a strong effect on the linewidth and intensity of a QD sample. The results in this chapter also showed capability of QD growth in terms of hitting a wide range of emission wavelengths- from 900 nm for Si-based detection to 1400 nm for telecommunication-based applications¹. The following chapters demonstrate practical use of this range.

¹ Both wavelengths refer to low temperature (~10 K) emission

3.4 References

- [1] Y Arakawa and H Sakaki. Multidimensional Quantum Well Laser and Temperature-Dependence of Its Threshold Current. *Applied Physics Letters*, 40(11):939–941, 1982.
- [2] Mashiro Asada, Y Miyamoto, and Yasuharu Suematsu. Gain and the threshold of three-dimensional quantum-box lasers. *Quantum Electronics, IEEE Journal of*, 22(9):1915–1921, 1986.
- [3] Albert-László Barabási. Self-assembled island formation in heteroepitaxial growth. *Applied Physics Letters*, 70(19):2565, 1997.
- [4] L Brusafferri, S Sanguinetti, E Grilli, M Guzzi, A Bignazzi, F Bogani, L Carraresi, M Colocci, A Bosacchi, P Frigeri, and S Franchi. Thermally activated carrier transfer and luminescence line shape in self-organized InAs quantum dots. *Applied Physics Letters*, 69(22):3354, 1996.
- [5] G Costantini, A Rastelli, C Manzano, P Acosta-Diaz, G Katsaros, R Songmuang, O G Schmidt, H von Kanel, and K Kern. Pyramids and domes in the InAs/GaAs(001) and Ge/Si(001) systems. *Journal of Crystal Growth*, 278(1-4):38–45, May 2005.
- [6] G Costantini, A Rastelli, C Manzano, R Songmuang, O G Schmidt, K Kern, and H von Kanel. Universal shapes of self-organized semiconductor quantum dots: Striking similarities between InAs/GaAs(001) and Ge/Si(001). *Applied Physics Letters*, 85(23):5673, 2004.
- [7] I Daruka and J Tersoff. Existence of shallow facets at the base of strained epitaxial islands. *Physical Review B*, 66(13):132104, October 2002.
- [8] I Daruka, J Tersoff, and A L Barabasi. Shape transition in growth of strained islands. *Physical Review Letters*, 82(13):2753–2756, 1999.
- [9] István Daruka and Albert-László Barabási. Dislocation-free island formation in heteroepitaxial growth: a study at equilibrium. *Physical Review Letters*, 79(19):3708, 1997.

- [10] R Dingle, W Wiegman, and C H Henry. Quantum States of Confined Carriers in Very Thin $\text{Al}_x\text{Ga}_{1-x}\text{As-GaAs-Al}_x\text{Ga}_{1-x}\text{As}$ Heterostructures. *Physical Review Letters*, 33(14):827–830, 1974.
- [11] Mark Fox. *Optical Properties of Solids*. Oxford University Press, March 2010.
- [12] D Gammon, S Rudin, T L Reinecke, D S Katzer, and C S Kyono. Phonon broadening of excitons in $\text{GaAs/Al}_x\text{Ga}_{1-x}\text{As}$ quantum wells. *Physical Review B*, 51(23):16785, 1995.
- [13] J M Garcia, G Medeiros-Ribeiro, K H Schmidt, T Ngo, J L Feng, A Lorke, J Kotthaus, and Pierre M Petroff. Intermixing and shape changes during the formation of InAs self-assembled quantum dots. *Applied Physics Letters*, 71(14):2014, 1997.
- [14] H Ghadi, S Adhikary, A Agarwal, and S Chakrabarti. Superlattices and Microstructures. *Superlattices and Microstructures*, 65(C):106–112, January 2014.
- [15] Bernard Goldstein and Daniel Szostak. Preferential evaporation of In from $\text{Ga}_x\text{In}_{1-x}\text{As}$. *Applied Physics Letters*, 26(12):685, 1975.
- [16] O Gunawan, H Djie, and B Ooi. Electronics states of interdiffused quantum dots. *Physical Review B*, 71(20):205319, May 2005.
- [17] S P Guo, A Shen, Y Ohno, and H Ohno. InAs quantum dots and dashes grown on (100), (211)B, and (311)B GaAs substrates. *Physica E-Low-Dimensional Systems & Nanostructures*, 2(1-4):672–677, July 1998.
- [18] Byounggu Jo, Jaesu Kim, Kwang Jae Lee, Hyunjune Kim, Dongwoo Park, Cheul-Ro Lee, Jin Soo Kim, Sung Bum Bae, Won Seok Han, Dae Kon Oh, Jae-Young Leem, Jong Su Kim, Sang Jun Lee, and Sam Kyu Noh. Thin Solid Films. *Thin solid films*, 518(22):6429–6431, September 2010.
- [19] J Johansson and W Seifert. Kinetics of self-assembled island formation: Part II - Island size. *Journal of Crystal Growth*, 234(1):139–144, January 2002.

- [20] P B Joyce, T J Krzyzewski, G R Bell, T S Jones, Surama Malik, D Childs, and Ray Murray. Effect of growth rate on the size, composition, and optical properties of InAs/GaAs quantum dots grown by molecular-beam epitaxy. *Physical Review B*, 62(16):10891–10895, 2000.
- [21] I Kamiya, I Tanaka, O Ohtsuki, and H Sakaki. Density and size control of self-assembled InAs quantum dots: preparation of very low-density dots by post-annealing. *Physica E-Low-Dimensional Systems & Nanostructures*, 13(2-4):1172–1175, March 2002.
- [22] Yoshiyuki Kobayashi and Koichi Yamaguchi. Control of photoluminescence wavelength from uniform InAs quantum dots by annealing. *Applied Surface Science*, 244(1-4):88–91, May 2005.
- [23] P Kratzer, Q Liu, P Acosta-Diaz, C Manzano, G Costantini, R Songmuang, A Rastelli, O G Schmidt, and K Kern. Shape transition during epitaxial growth of InAs quantum dots on GaAs(001): Theory and experiment. *Physical Review B*, 73(20):205347, May 2006.
- [24] Eric le Ru, J Fack, and Ray Murray. Temperature and excitation density dependence of the photoluminescence from annealed InAs/GaAs quantum dots. *Physical Review B*, 67(24):245318, June 2003.
- [25] D Leonard, K Pond, and Pierre M Petroff. Critical Layer Thickness for Self-Assembled InAs Islands on GaAs. *Physical Review B*, 50(16):11687–11692, 1994.
- [26] H Y Liu, B Xu, Y H Chen, D Ding, and Z G Wang. Effects of seed layer on the realization of larger self-assembled coherent InAs/GaAs quantum dots. *Journal of Applied Physics*, 88(9):5433, 2000.
- [27] Surama Malik, Christine Roberts, Ray Murray, and Malcolm Pate. Tuning self-assembled InAs quantum dots by rapid thermal annealing. *Applied Physics Letters*, 71(14):1987–1989, 1997.
- [28] J H Marsh. Quantum-Well Intermixing. *Semiconductor Science and Technology*, 8(6):1136–1155, June 1993.
- [29] W M McGee, T J Krzyzewski, and T S Jones. Atomic scale structure and morphology of (In,Ga)As-capped InAs quantum dots. *Journal of Applied Physics*, 99(4):043505, 2006.

- [30] G Medeiros-Ribeiro. Shape Transition of Germanium Nanocrystals on a Silicon (001) Surface from Pyramids to Domes. *Science*, 279(5349):353–355, January 1998.
- [31] F Montalenti, P Raiteri, D Migas, H von Kanel, A Rastelli, C Manzano, G Costantini, U Denker, O G Schmidt, K Kern, and Leo Miglio. Atomic-Scale Pathway of the Pyramid-to-Dome Transition during Ge Growth on Si(001). *Physical Review Letters*, 93(21):216102, November 2004.
- [32] I Mukhametzhanov, Z Wei, R Heitz, and A Madhukar. Punctuated island growth: An approach to examination and control of quantum dot density, size, and shape evolution. *Applied Physics Letters*, 75(1):85, 1999.
- [33] Tzer-En Nee, Ya-Fen Wu, Chao-Ching Cheng, and Hui-Tang Shen. Carrier dynamics study of the temperature- and excitation-dependent photoluminescence of InAs/GaAs quantum dots. *Journal of Applied Physics*, 99(1):013506, 2006.
- [34] A Rastelli and H von Kanel. Surface evolution of faceted islands. *Surface Science*, 515(2-3):L493–L498, 2002.
- [35] K H Schmidt, G Medeiros-Ribeiro, U Kunze, G Abstreiter, M Hagn, and Pierre M Petroff. Size distribution of coherently strained InAs quantum dots. *Journal of Applied Physics*, 84(8):4268, 1998.
- [36] O B Shchekin, G Park, D L Huffaker, and D G Deppe. Discrete energy level separation and the threshold temperature dependence of quantum dot lasers. *Applied Physics Letters*, 77(4):466–468, 2000.
- [37] Jae Cheol Shin, Won Jun Choi, and Jeong-Woo Choe. Effect of thermal treatment on the optical and the structural properties of In_{0.5}Ga_{0.5}As quantum dots. *Journal of the Korean Physical Society*, 64(9):1375–1379, May 2014.
- [38] M Tomitori, K Watanabe, M Kobayashi, and O Nishikawa. STM Study of the Ge Growth Mode on Si(001) Substrates. *Applied Surface Science*, 76(1-4):322–328, March 1994.

- [39] V M Ustinov, N A Maleev, A E Zhukov, A R Kovsh, A Yu Egorov, A V Lunev, B V Volovik, I L Krestnikov, Yu G Musikhin, N A Bert, P S Kop'ev, Z I Alferov, N N Ledentsov, and D Bimberg. InAs/InGaAs quantum dot structures on GaAs substrates emitting at $1.3 \mu\text{m}$. *Applied Physics Letters*, 74(19):2815, 1999.
- [40] Y P Varshni. Temperature dependence of the energy gap in semiconductors. *Physica*, 34(1):149–154, 1967.
- [41] Q H Xie, J L Brown, R L Jones, and J E Van Nostrand. Shape stabilization and size equalization of InGaAs self-organized quantum dots. *Journal of electronic materials*, 28(12):L42–L45, December 1999.
- [42] Q H Xie, J L Brown, and J E Van Nostrand. Cooperative nucleation and evolution in InGaAs quantum dots in multiply stacked structures. *Applied Physics Letters*, 78(17):2491, 2001.
- [43] S J Xu, X C Wang, S J Chua, C H Wang, W J Fan, J Jiang, and X G Xie. Effects of rapid thermal annealing on structure and luminescence of self-assembled InAs/GaAs quantum dots. *Applied Physics Letters*, 72(25):3335, 1998.
- [44] Zhong-Ying Xu, Zhen-Dong Lu, X P Yang, Z L Yuan, B Z Zheng, J Z Xu, W K Ge, Y Wang, J Wang, and L L Chang. Carrier relaxation and thermal activation of localized excitons in self-organized InAs multilayers grown on GaAs substrates. *Physical Review B*, 54(16):11528, 1996.
- [45] M Yahyaoui, K Sellami, S Ben Radhia, K Boujdaria, M Chamarro, B Eble, C Testelin, and Aristide Lemaître. Effects of strain on the optoelectronic properties of annealed InGaAs/GaAs self- assembled quantum dots. pages 1–12, May 2014.
- [46] Tao Yang, Jun Tatebayashi, Kanna Aoki, Masao Nishioka, and Yasuhiko Arakawa. Effects of Rapid Thermal Annealing on the Emission Properties of Highly Uniform Self-Assembled InAs/GaAs Quantum Dots Emitting at $1.3\mu\text{m}$. *Applied Physics Letters*, 90(11):111912, 2007.
- [47] Vilma Zela, I Pietzonka, T Sass, Claes Thelander, Sören Jeppesen, and W Seifert. Unimodal dome-shaped island population of Ge/Si (001)

- by step-wise growth in UHV-CVD. *Physica E-Low-Dimensional Systems & Nanostructures*, 13(2):1013–1017, 2002.
- [48] Y C Zhang, Z G Wang, B Xu, F Q Liu, Y H Chen, and P Dowd. Influence of strain on annealing effects of In(Ga)As quantum dots. *Journal of Crystal Growth*, 244(2):136–141, October 2002.

LOW DENSITY QUANTUM DOT GROWTH

The homogeneous broadening of quantum dot ensemble emissions is often not desirable for analysis of the individual characteristics of single quantum dots, particularly the atom-like energy levels. Average QD density would be approximately $10 \times 10^{10} \text{ cm}^{-2}$ ($\sim 100 \mu\text{m}^{-2}$) at conventional growth rates, meaning that any excitation will cause many hundreds of dots to emit, again yielding a broad spectrum. With numerous applications requiring the properties of individual dots, including plasmonics, single-photon emitters, entangled photon sources and quantum information, isolation of quantum dots is needed, thus calling for a method for growing low density quantum dots.

The density of quantum dots is related to the growth rate- the lower the growth rate, the less populous a QD layer will be [8]: This can be varied from 10^5 cm^{-2} to 10^{11} cm^{-2} , although this is only controllable above 10^7 cm^{-2} . In order to isolate a quantum dot, the ideal density is typically lower than 10^9 cm^{-2} , which works out to be $1 \mu\text{m}^{-2}$, and the growth rate needed for this kind of density is very low ($< 10^{-3} \text{ ML/s}$ [1]). The desired density is usually determined by the spot size of the excitation laser for PL analysis, or otherwise by the aperture size if using masking techniques. Other applications, such as those using pillar microcavities require a density of approximately $\sim 2 \mu\text{m}^{-2}$ [2].

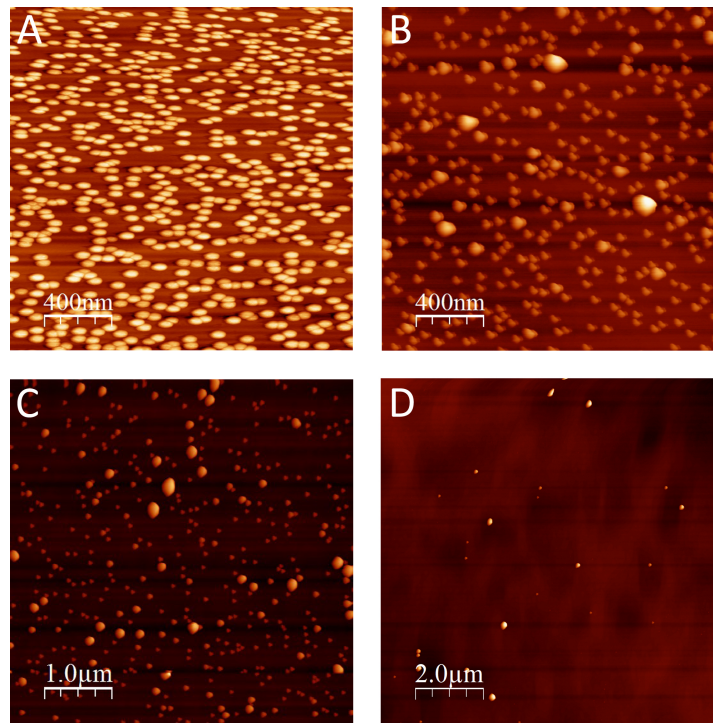


Figure 4.0.1: AFM of Varying Growth Rate Samples

In order to consider the correlation between growth rate and QD density, a series of samples were grown varying the indium growth rate, but otherwise ensuring growth parameters were the same, in particular the growth temperature of the QDs. Figure 4.0.1 shows the AFM used for a selection of the resultant samples, with table 4.0.1 describing the 2D-3D transition time. The AFM scans of “A” and “B” were performed over $2\ \mu\text{m}$ squares, where as “C” and “D” required larger scans to provide statistically meaningful quantities of QDs: over $5\ \mu\text{m}$ and $10\ \mu\text{m}$ squares respectively. The 2D-3D transition time was measured by observing the RHEED reconstruction of the growing InAs layer, whereupon a marked change occurs when the 2D pseudomorphic wetting layer makes the transition to 3D islands. This transition occurs at 1.7 ML, and therefore the InAs growth rates can be calculated using these times.

Sample Reference	2D-3D time (mm:ss)	Calculated Growth Rate (\AA s^{-1})
A	2:02	0.045
B	2:51	0.032
C	7:55	0.011
D	16:30	0.0055

Table 4.0.1: Table describing the 2D-3D growth times according to the labels in the AFM images shown in figure 4.0.1.

Although the density of the QDs is clearly reduced, it is uncertain whether or not the dots are evenly distributed enabling spatial addressing of individual dots, or if they group together. If the dots show a tendency to form groups, isolation of individual QDs is made no easier, thus rendering the difficult low-growth-rate QDs redundant. It is also uncertain whether or not the behaviour of the QD growth is affected with reduced growth rate, other than the density.

To further aid the determination of the effect of the growth rate on the growth of QDs, the AFM scans shown in figure 4.0.1 were subject to statistical analysis, describing the likelihood of encountering a QD from the point of view of another QD, within a particular locus. The data analysis was performed by Gavin Bell from the University of Warwick¹.

Figure 4.0.2 shows the Voronoi tessellation of the samples represented in figure 4.0.1. The values above each plot represent the 2D-3D transition time, e.g.: 2m02 represents a 2D-3D transition time of two minutes two seconds. The final images labelled "Poisson" and "Regular" demonstrate the expected variation if the QDs grew in a perfect Poisson distribution, or standard distribution. These plots demonstrate that the slower the growth rate, the larger the domain size, showing that QDs do not appear to group. It may also be noted that the data appears to represent a Poisson distribution rather than a standard distribution, indicating a spontaneous island formation, rather than formation dependent on neighbouring islands.

Figure 4.0.3 uses the data from the Voronoi tessellations in figure 4.0.2 and describes the probability of encountering a neighbouring island vs. the normalised distance. The solid lines represent the probability for a regular (red) and Poisson (black) distribution, with the distribution of QDs on a surface showing a closer approximation to the Poisson distribution, with the

¹ Department of Physics, University of Warwick, Coventry, CV4 7AL

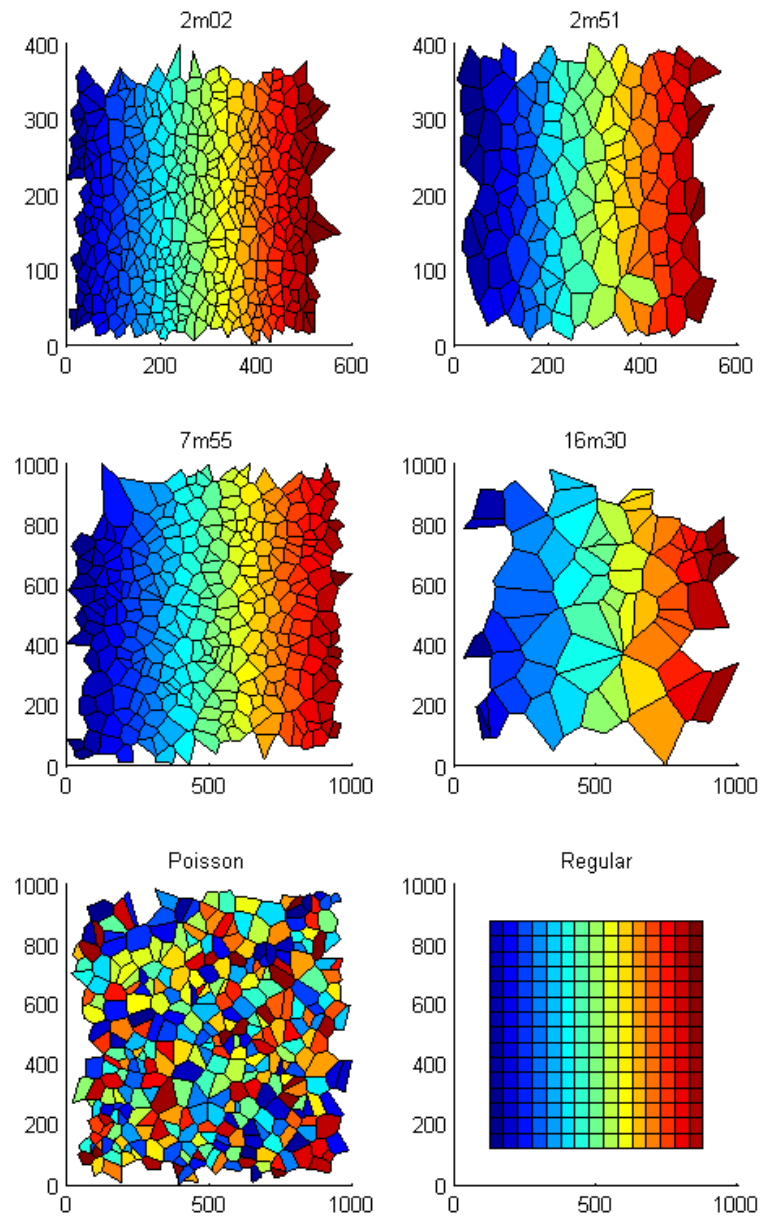


Figure 4.0.2: Voronoi Tesselation of Varying Density QD Samples. The colours are used as a method of aiding visual clarity. The times as noted are the 2D-3D transition time for each sample, with the lower plots describing perfectly Poisson and standard distribution respectively.

times representing the 2D-3D transition time. A regular distribution would indicate a tendency for the dots to maximise their separation, indicating an interaction between the quantum dots. Poisson distribution shows that the

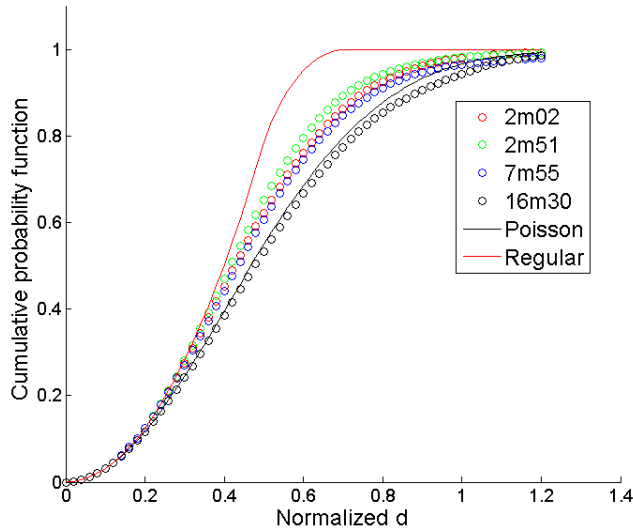


Figure 4.0.3: Probability of Encountering a Neighbouring QD Compared with the Normalised Distance, d .

formation of quantum dots is rather more random, and that there is seemingly no interaction between the individual dots. Indeed, Cullis et al [6] note that the 2D-3D transition is based on the segregation of elemental indium to the surface of the wetting layer, with a critical surface concentration of indium being required before 3D island formation occurs. The same study details the formation of islands thermodynamically: the free energy of the adatoms' clustering and forming "unstable growth nuclei", which expand until the adatoms' free energy reaches a maximum and consequently stable islands form, reducing the free energy. In other words, the formation of the 3D islands is based rather more on the adatoms rather than interaction between the islands themselves.

This analysis shows that low growth rates can be used to isolate single dots over the length scales required for viable quantum information (QI) devices, and the statistics presented here don't indicate a tendency of QDs to form clusters. However to obtain the lowest growth rates (for the largest area devices), we have to use extremely low growth rates (15 min to 20 min 2D-3D time) and this might also result in other issues with the QD emission quality. As an example, the extended growth time for the QDs may allow additional incorporation of impurities near the QDs. These impurities may result in localised charged states near the QDs that will cause an increase

in the homogeneous broadening of single QD emission lines and a corresponding reduction in their quantum coherence properties. In addition, with such low growth rates, the repeatability from run-to-run is particularly difficult due to the measurement of indium flux being comparable with respect to the background measurement. This results in samples of varying quality and emission characteristics. In the next section we use a rotation stop to provide an alternative method to achieve a controllable low density by spatial selection, which avoids the need for the very low growth rates.

4.1 Rotation-Stop Growth Method

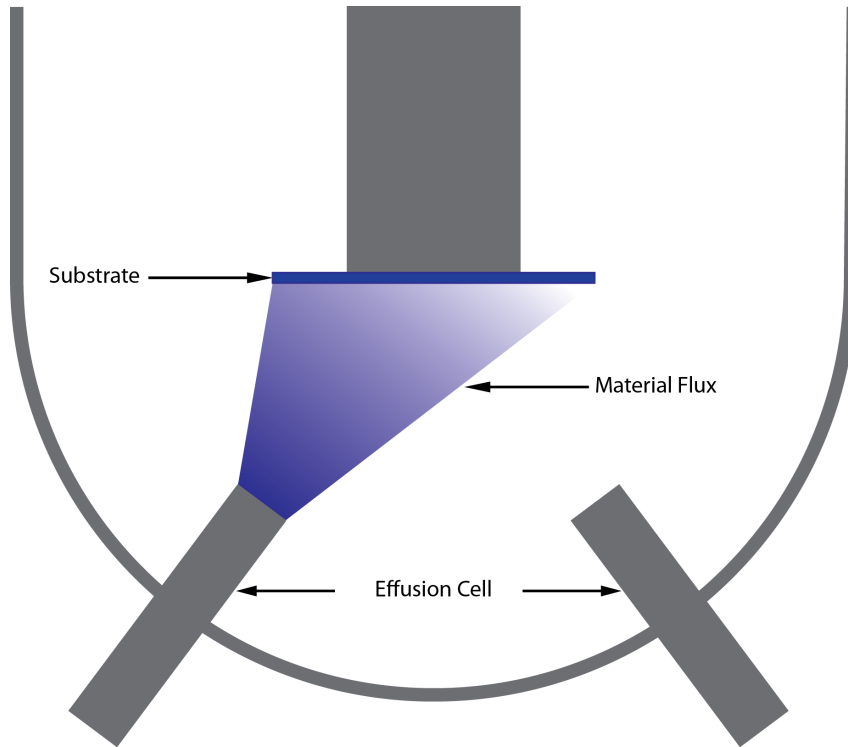


Figure 4.1.1: Basic Schematic of an MBE Reactor Showing an Exaggerated Graphical Representation of the Uneven Distribution of Flux Across a Substrate

The geometry of an MBE reactor means that, for uniform 2D planar growth, the substrate must be rotated, as the impinging molecular beams are angled towards the substrate, causing an uneven growth rate across the substrate surface. The As flux also varies across the wafer, but the variation of QD density corresponds with the position of the indium cell, with the effect of the As seemingly negligible.

4.1.1 Short-Wavelength Rotation-Stop Quantum Dots

Initial attempts to alter the quantum dot density by the rotation stop method used a GaAs capped QD sample, and a relatively low growth rate of 0.07 \AA s^{-1} , with an indium flush to control the wavelength.

Figure 4.1.2 gives a broad overview of the QD density on the wafer, with the total indium deposited increasing from positions A to E. The PL map-

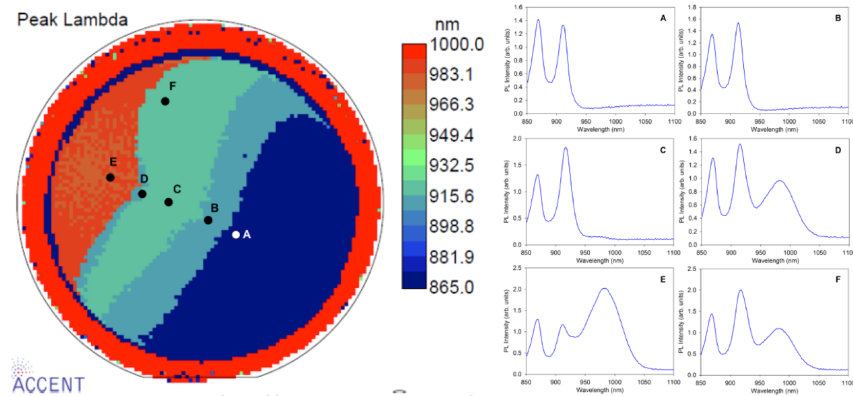


Figure 4.1.2: Room Temperature PL Map and Accompanying PL on In-flush sample

ping is done on an automated stage with x-y control, allowing a full wafer scan, with each point on the map in figure 4.1.2 referring to a parameter (in this case the wavelength) of the PL spectra taken at that point. This is shown by the QDs emitting at around 990 nm, and no such emission exists in a significant capacity until point D, with the prominent peaks in the PL being caused by emission from the GaAs (~ 870 nm) and InAs wetting layer (~ 910 nm) until this point on the wafer. The data shown in figure 4.1.2 were measured using a Si CCD detector. As such, the detector's response above 1000 nm is significantly reduced. The measurement taken was not corrected for the detector's response as the primary purpose for the measurement was to determine the peak wavelength of the QDs, rather than an accurate comparison of their intensities. Until the emergence of the QDs, the WL emits as a narrow pseudomorphic InAs QW, the QDs emergence providing a lower energy for the carriers to relax and recombine to. This image only provides a rough spatial analysis of the PL variance across the wafer, with no quantifiable description as to the potential to isolate individual quantum dots. However, this is useful to identify regions of the wafer to examine in order to isolate single QD emission.

In order to properly determine the suitability of the sample, and which area of the wafer is best suited to single QD purposes, the wafer was divided into labelled "chips" and each "chip", unprocessed, was subjected to low temperature (< 10 K) micro PL measurements. Micro PL operates in the same manner as PL, with the addition of extra focusing lenses to reduce the

excitation laser spot size. All micro PL work was done by Richard Phillips' group at Cambridge's Cavendish Laboratory².

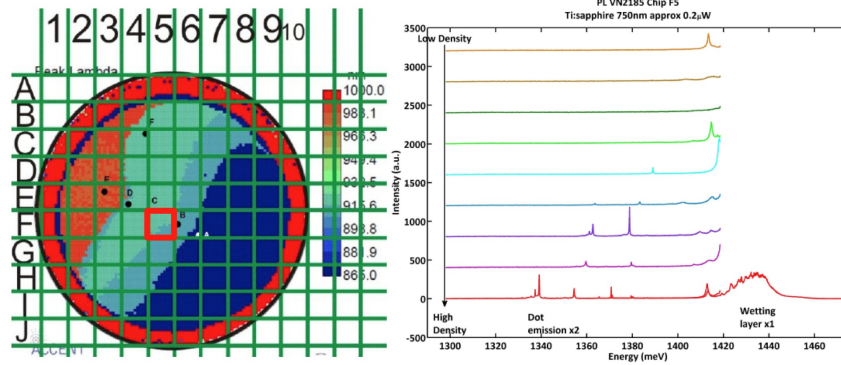


Figure 4.1.3: μ PL of chip F5 (as labelled)

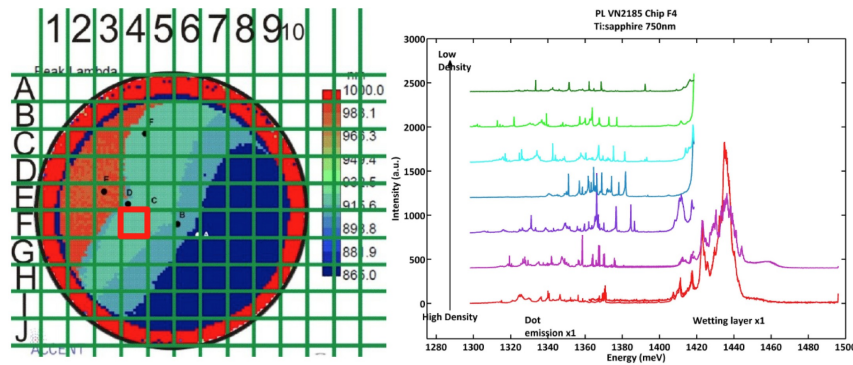


Figure 4.1.4: μ PL of chip F4 (as labelled)

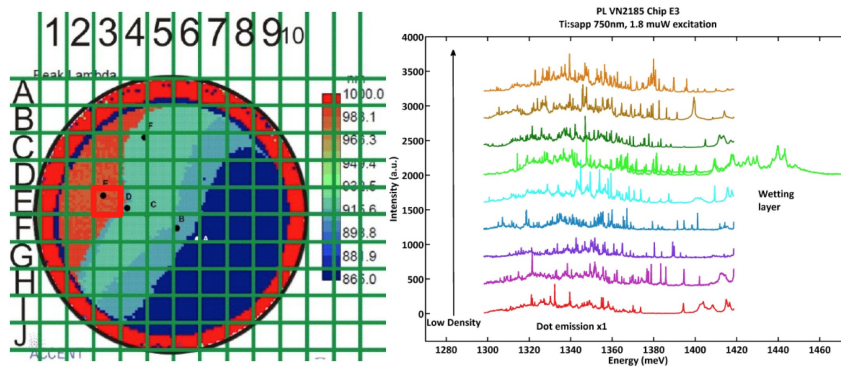


Figure 4.1.5: μ PL of chip E3 (as labelled)

The measurement in figure 4.1.3 shows the best “chip” found on the wafer, labelled F5 according to the superimposed grid. The individual μ PL spectra

² Peter Brereton, Megan Stanley and Richard Phillips; Atomic, Mesoscopic and Optical Physics Group, Department of Physics, Cavendish Laboratory, University of Cambridge, UK

show a few, well-separated transitions in this low-density area, with the neighbouring F6 chip (not shown) only emitting from the wetting layer. Note that the single dot PL does not give a direct representation of the number of QDs being examined: single QDs can contain multiple excitonic states, which are discussed further in section 4.2.1.

The chip in figure 4.1.4 is closer to the wetting layer-quantum dot boundary as it appears on the map. There is a higher density of quantum dots, but there are still resolvable individual narrow QD transitions, with possible localised states in the wetting layer.

The chip in figure 4.1.5 is well into the QD side of the WL-QD boundary, but even with the higher density of QDs, individual QD transitions are visible and remain resolvable, though this section is considerably more difficult to use than the extremely low density chip in figure 4.1.3 as QDs have to be spectrally resolved instead of simply spatially resolving them.

This sample only provides PL as a (non-intrusive) method of sample investigation: the number of QDs per unit area and the size and type of the QDs aren't quite as easily determined as with a dual PL-AFM structure, which is nearly identical in structure, but with an uncapped QD layer on the surface of the sample. This uncapped QD layer is grown in identical conditions as the optically-active QDs in the sample, with rapid cooling to "fix" the islands in place on the surface for easy examination by AFM. The following sample is not grown using the In-flush method, so the wavelength of the PL emission is longer compared to the previous sample, with the range of the InGaAs detector not reaching below 1000 nm, meaning that the wetting layer and GaAs emission will not be measured. There are likely to be small variations in the growth conditions between the PL and AFM layer, although broadly speaking the PL and AFM data should correlate.

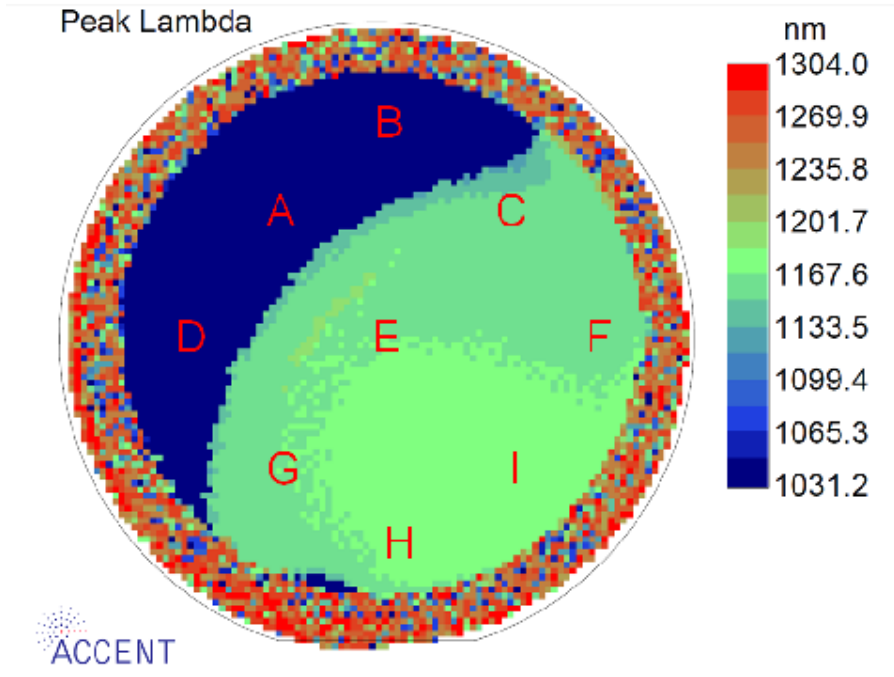


Figure 4.1.6: PL Map of GaAs Capped Rotation Stop QD PL/AFM Sample

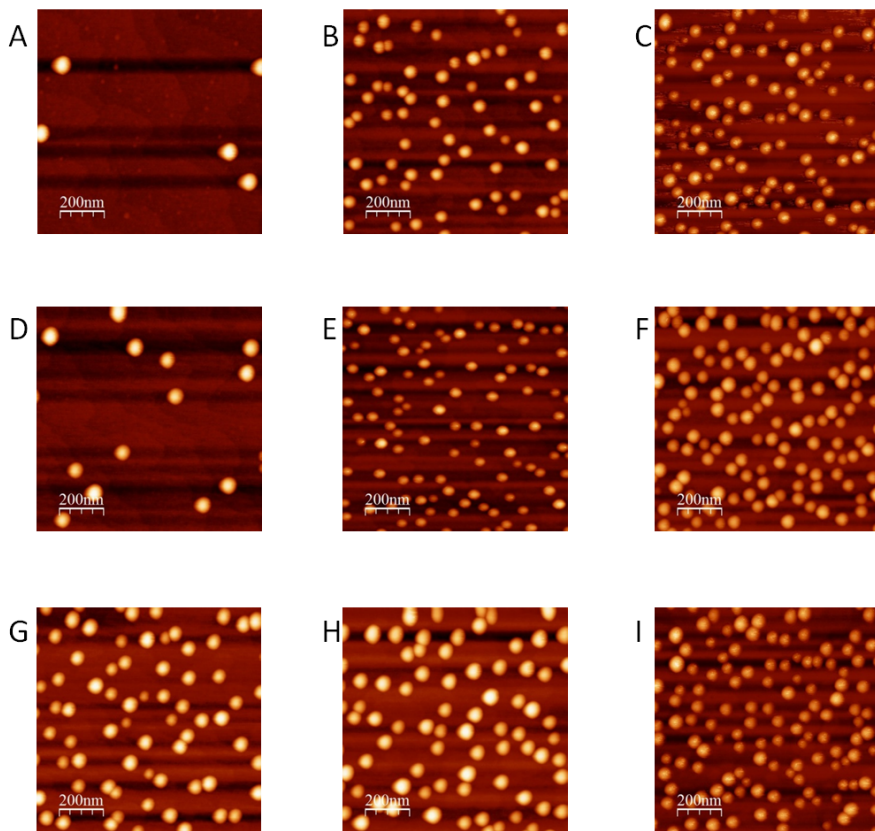


Figure 4.1.7: Corresponding AFM Scans, labelling as per 4.1.6

It was assumed, after analysing the PL map (figure 4.1.6), that there were no quantum dots at points A,B or D, due to a lack of emission at the desired wavelength at those particular points, but the AFM scan shows something that would otherwise not be detected- a few larger QDs (which may be undetectable at room temperature). When looking at the raw data of the AFM and noting the physical characteristics of the individual QDs (i.e. height and diameter), there is evidence of bimodal growth, suggesting a lack of maturity of the dots, or, more likely, a distribution of pyramids and domes. Unfortunately the resolution of the AFM images taken is too low to properly determine the faceting of the QDs. The measurement point B shows a large proportion of QDs considering the PL map showing little-to-no emission, this may be due to the AFM measurement lying closer to the transition point than estimated.

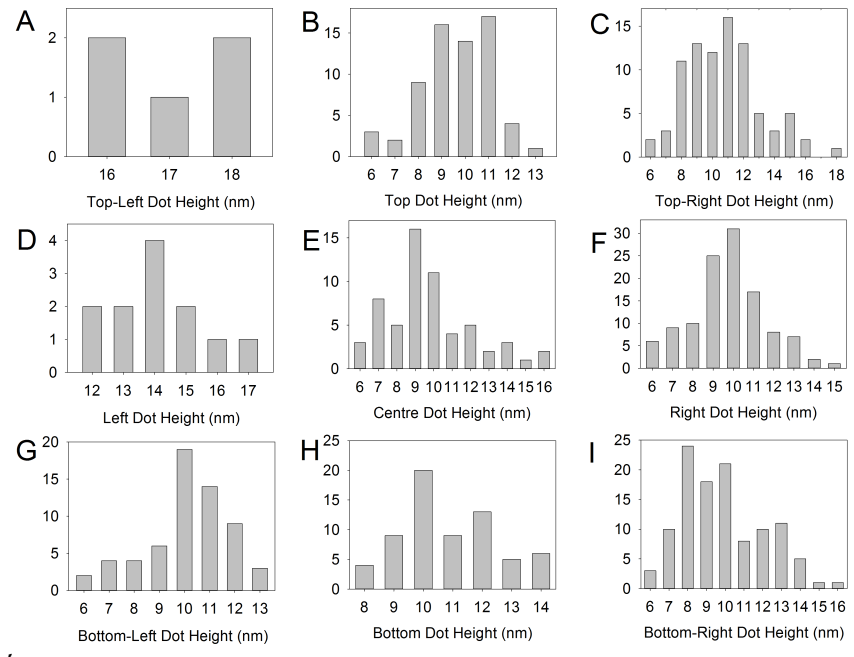


Figure 4.1.8: Statistics of the quantum dots in the respective AFM images from Figure 4.1.6

Comparing figure 4.1.8 with the earlier AFM analysis, it is clear that the rotation stop sample is rather more bimodal in the high-density areas, with a wider spread of QD heights, although 10/11 nm appears to be the most frequent height, with the lower density areas producing larger QDs. The PL layer uses the In-flush method to control the emission wavelength for

use with Si detectors; this means that the larger size of the low-density QDs is somewhat nullified- larger dots provide a deeper confining potential, allowing for longer wavelength emission.

4.1.2 Long-Wavelength Rotation-Stop Quantum Dots

Growing a DWELL structure (Section 3.2.3) and using the rotation stop method, there was a difference in the variation of QD density across the wafer: whilst the density of dots still varied, there was still a high density of quantum dots across the entire wafer, making it much more difficult to resolve individual dots. The physics of the quantum dots in these samples will be slightly different due to their deeper confining potentials, with more bound states, and a much larger energetic separation between the ground states in the quantum dots and that of the wetting layer. The latter is particularly useful as there is less background light from the tail of the wetting layer emission influencing the measurement of the quantum dot emission (compared to the short-wavelength samples).

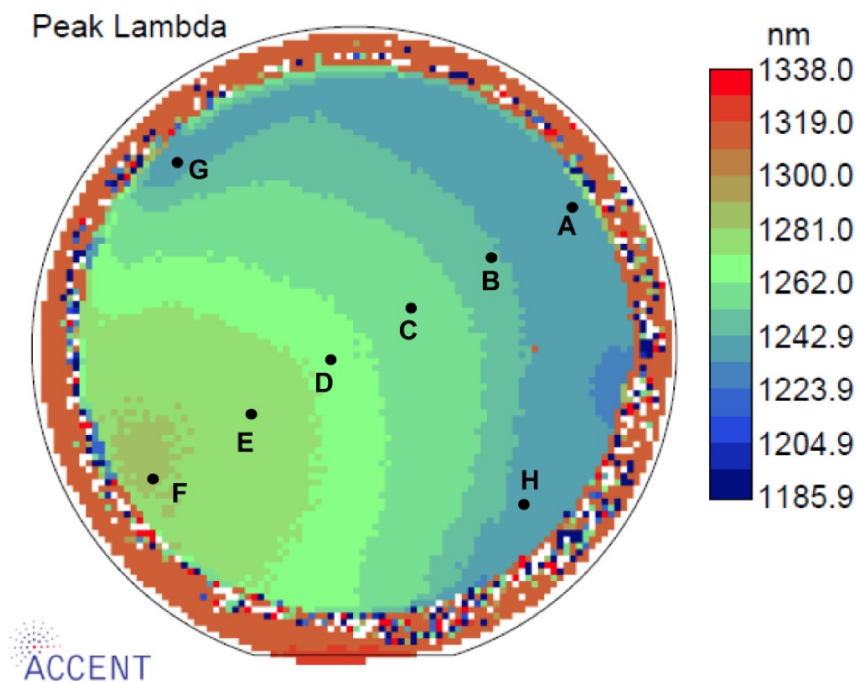


Figure 4.1.9: PL Map of DWELL Rotation Stop QD Sample

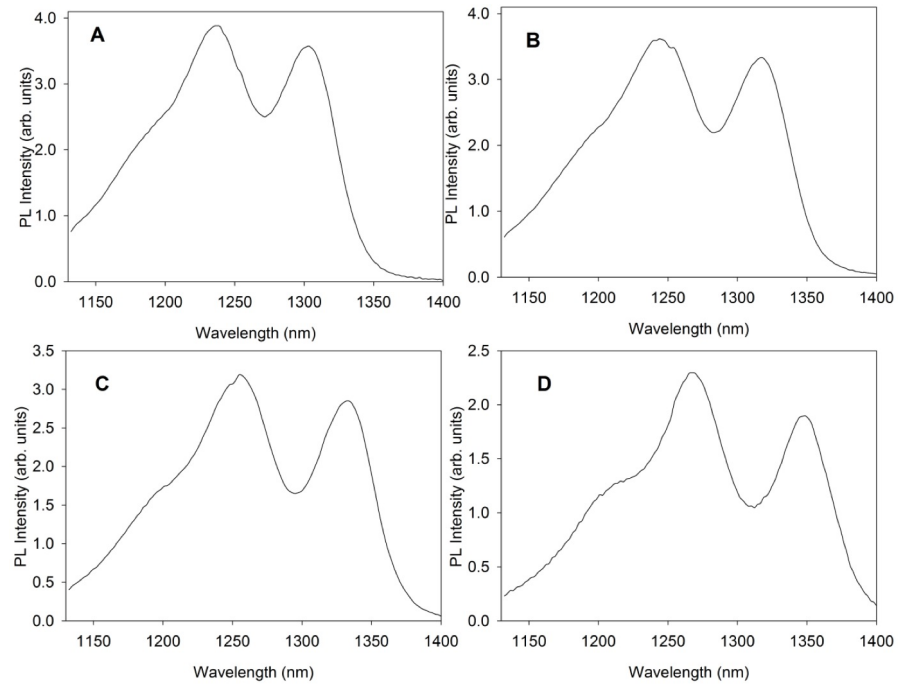


Figure 4.1.10: PL Spectra Labelled According to Fig. 4.1.9.

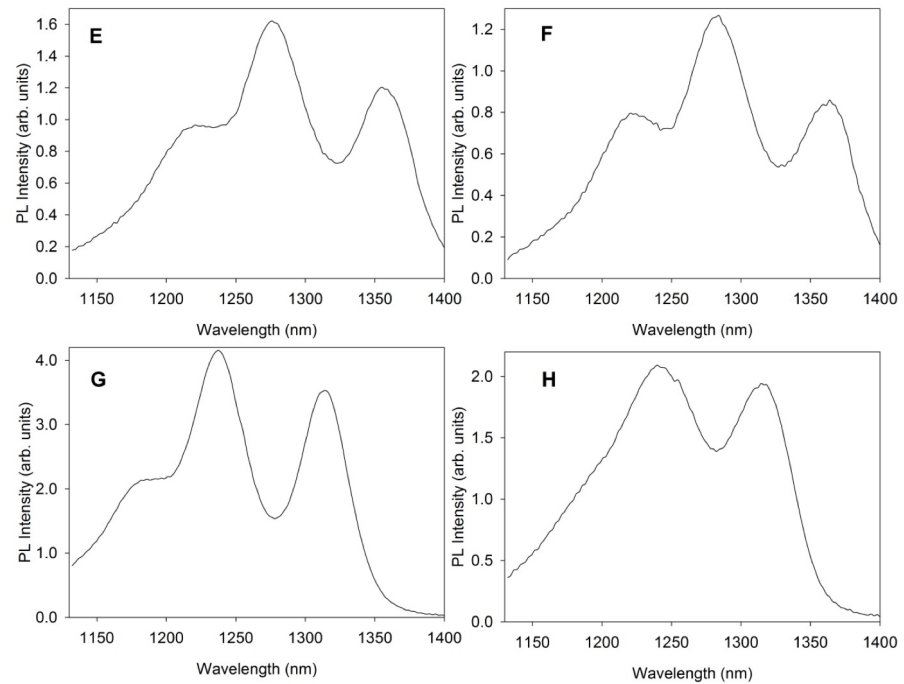


Figure 4.1.11: PL Spectra Labelled According to Fig. 4.1.9.

The proportion of state filling and the decreasing integrated PL intensity indicates that there is a gradient of decreasing QD density in the direction

A→F, with the lowest QD density and concomitantly the longest emission wavelength around point F. The appearance of quantum dot emission across the wafer is primarily due to the indium flux not being fully calibrated, meaning that the growth rate for the QW of the DWELL being of a slightly different composition than calculated prior to growth. bimodality is much more evident in these samples, with two clear peaks, present at 1200 nm and > 1300 nm, creating further problems for the spectral resolution of individual dots, most notably, an unwanted source of short wavelength light.

4.2 Applications for Low-Density Quantum Dots

4.2.1 Entangled Photon Sources at Telecoms Wavelengths

An area of particular interest for low density quantum dots is that of entangled photon sources: emitters of photons that are indistinguishable from one another in terms of their polarisation. Light emission in semiconductors comes from the recombination of excitons, which are electron-hole pairs coupled by mutual Coulomb attraction. For entangled photon sources, different types of excitons must be taken into account. The difference between the excitons being considered, is their composition (and therefore charge): Neutrally charged excitons have a balanced electron-hole pairing ratio, with X^0 having a single electron hole pair, and $2X^0$ being comprised of two electron hole pairs. Positively charged excitons have a surfeit of holes; X^{1+} being comprised of an electron-hole pair with an extra hole, with the negative equivalent being X^{1-} , an exciton with an extra electron in addition to the electron-hole pair, and X^{2-} having two extra electrons. Each of these excitons recombine at a similar wavelength, but are separated in energy thanks to Coulomb interactions.

The samples as grown for section 4.1.2 were charge-tunable devices in the form of Schottky diodes (figure 4.2.1), meaning that a gate voltage can be applied to the sample, allowing control of the carriers within the active region, and therefore the quantum dots, as described in [13]. As the sample did not achieve the QD density required, individual dots had to be spectrally resolved for the single-dot PL to be performed. All practical single-



Figure 4.2.1: Schottky device structure, as grown for Heriot-Watt.

dot work was performed by Luca Sapienza, Brian Gerardot and colleagues at Heriot Watt University³. Using confocal micro-PL, with a zirconia super-solid immersion lens (SIL) on the surface of the sample to increase collection efficiency as well as reducing the excitation spot size [9], it was possible to detect individual photons from individual quantum dots.

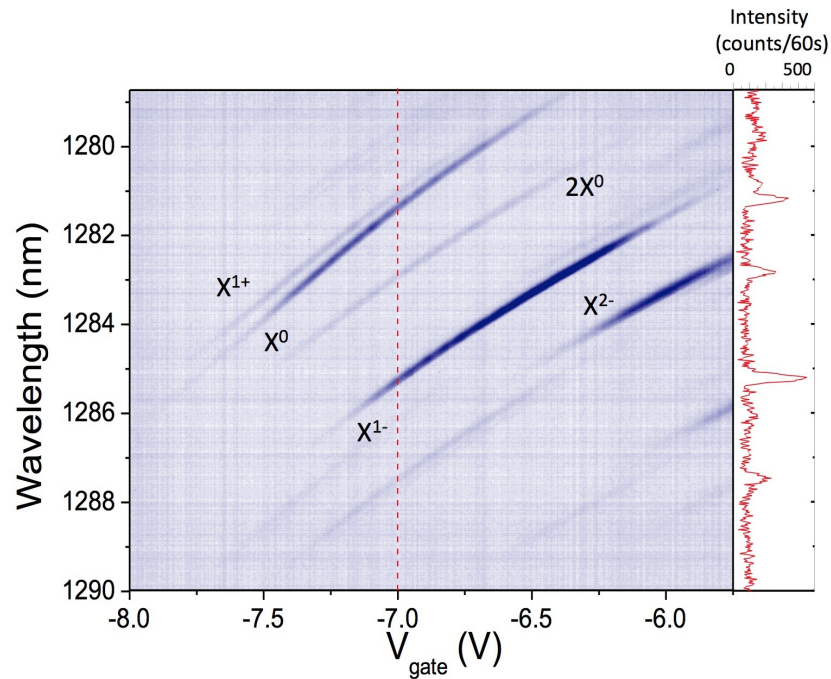
Figure 4.2.2: Single-Dot Emission vs. Gate Voltage (V_{gate}) across the Schottky Diode QD Sample

Figure 4.2.2 shows the variation in PL as the gate voltage is changed across the sample. The right hand PL trace shows the spectrum for a gate

³ Luca Sapienza, Ralph Malein, Christopher E. Kuklewicz, Peter E. Kremer and Brian Gerardot, Institute of Photonics and Quantum Sciences, SUPA, Heriot-Watt University, Edinburgh, United Kingdom

voltage of -7V , with the X^{1+} ($\sim 1281\text{ nm}$), X^0 ($\sim 1281.5\text{ nm}$), $2X^0$ ($\sim 1283\text{ nm}$), X^{1-} ($\sim 1285.5\text{ nm}$) and X^{2-} ($\sim 1287.5\text{ nm}$) peaks all identified. With all of these differing emissions from one quantum dot, spectral filtering is needed to yield a single-photon source- X^0 usually chosen to be filtered as it's always present, however, for entangled photon sources, both the biexciton ($2X^0$) and the exciton (X^0) are used.

4.2.2 Fine Structure Splitting (FSS)

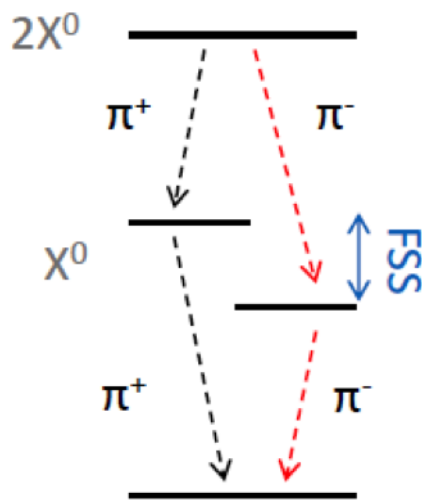


Figure 4.2.3: Biexciton Cascade: A Visual Representation of FSS

The choice of X^0 and $2X^0$ is due to the biexciton cascade that occurs (Figure 4.2.3). A biexciton cascade is the result of the two confined e-h pairs, the first of which emits a photon at the biexciton energy ($2X^0$), with the remaining exciton emitting at the exciton energy (X^0). An entangled photon source uses the fact that, under the right conditions, the polarisation of these

photons can be quantum mechanically entangled, meaning that the path of the biexciton as per figure 4.2.3 is undetectable. The difference between these two paths is known as the fine structure splitting (FSS), and for entanglement to occur, the FSS must be less than the linewidth of the emission from either recombination. Each path can be distinguished by the polarisation of the emitted light, which is detected by applying a polarisation filter between the measured sample and the detector, and rotating between 0 ($\pi+$) and 90 ($\pi-$) (figure 4.2.4).

Figure 4.2.4 shows the difference between $\pi+$ and $\pi-$ filtered emissions of the same quantum dot. There is a clear difference between the two, with the X^0 and $2X^0$ peaks differing in wavelength by approximately $1/10\text{ nm}$, although the X^{1-} peak showing very little variation. The difference in energy of the peaks represents the FSS, which is larger than desired, being larger

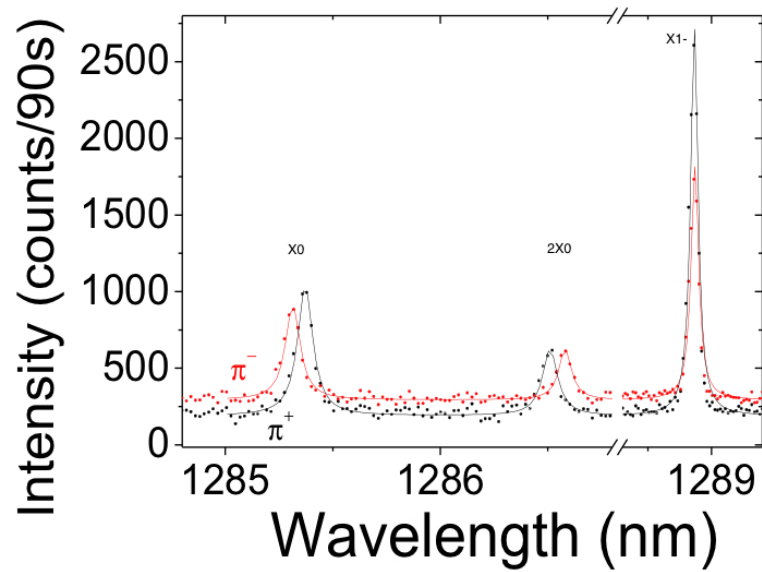


Figure 4.2.4: Polarised PL showing π^+ and π^- emissions.

than the linewidth of the biexciton and exciton peaks (at tens of μeV) but considerably less than expected for QDs at this wavelength, considering previous work with 1300 nm QDs[5, 11, 14].

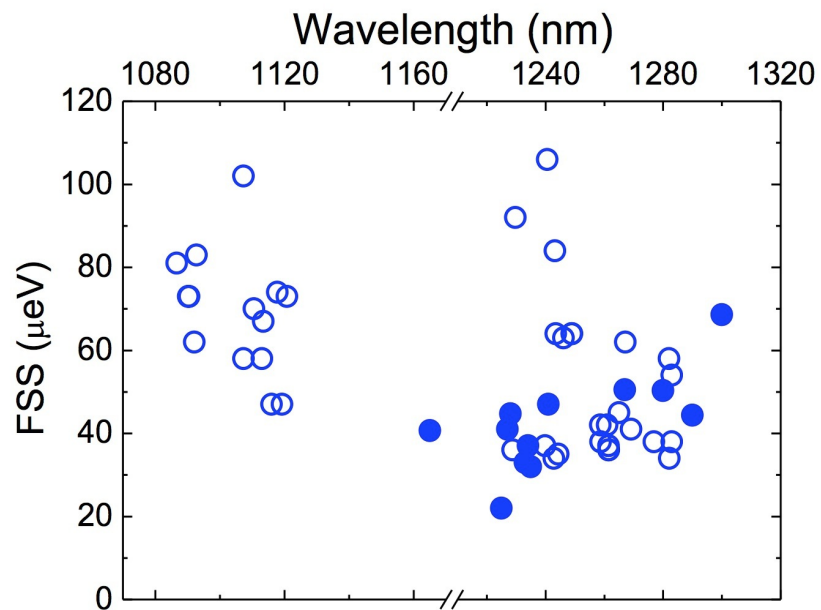


Figure 4.2.5: Comparison of the FSS of Measured QDs (Filled Circles grown by the University of Sheffield, empty circles grown by the semiconductor and dimensional metrology division at the National Institute of Standards and Technology (NIST))

Figure 4.2.5 shows the FSS and accompanying wavelength of a number of quantum dots, with the solid dots representing charge-tunable samples grown at the University of Sheffield, and the hollow dots representing bulk DWELL QDs grown by NIST⁴. As an average, the FSS of the dots from the University of Sheffield is approximately 40 μeV , with the lowest being at 22 μeV .

4.2.3 Minimising FSS at Telecom Wavelengths

Recent advances in detector technology have enabled the detection of single photons at longer wavelengths, allowing the measurement of FSS at telecom wavelengths (figure 4.2.4). The shape of the QD potential affects the FSS in a significant manner- if the potential is more symmetric, the FSS may be reduced, indicating that the shape of the QDs has a large bearing on the FSS[4, 7, 10]. Compared to the shorter wavelength QDs grown by NIST, there may be a homogeneity in the symmetry of the QDs due to the DWELL structure, which reduces the out-diffusion of indium from the InAs QDs into the InGaAs cap, and results in a more symmetric dot.

In order to alter the FSS of the QDs, an external strain field was used, applied by mounting the sample on a piezo stack, which alters the uniaxial strain according to the voltage applied.

Figure 4.2.6 shows the resulting change in PL for one quantum dot in the charge tunable structure as grown by Sheffield, when $\pm 300\text{ V}$ is applied to the piezo stack. It is clear that the wavelength undergoes a significant change, and the FSS is reduced- noted by the change in proximity in the two PL peaks. Figure 4.2.7 shows the corresponding polar plots for the quantum dot, at the same piezo voltages. It is interesting to note that the polarisation is the same for both situations, and is seen to be the same for the remainder of the measured quantum dots for the charge-tunable device, lending credence to the previous statement that the DWELL QDs exhibit similar symmetry, with the polarisation aligning along the [110] direction. This is also the optimum direction for minimising the FSS under strain tuning. There is no immediate explanation for this apparent preferential orientation, and

⁴ Nanostructure Fabrication and Metrology, 325 Broadway, Boulder, CO 80305-3328

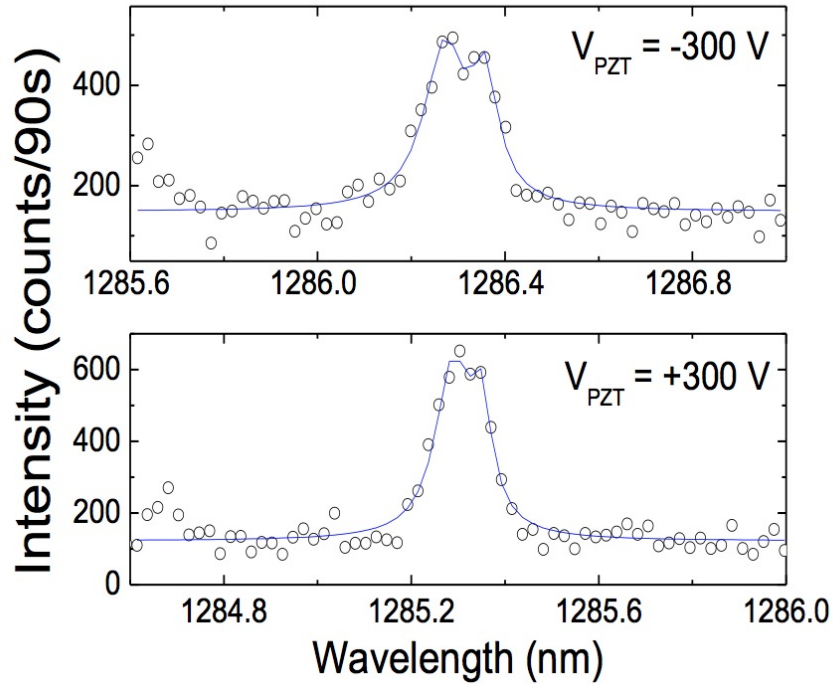


Figure 4.2.6: Figure showing an example of FSS tuning via external application of uniaxial strain

investigation into this is still ongoing, with consideration given to preferential indium migration, and the reduction of interdiffusion of indium into the capping material.

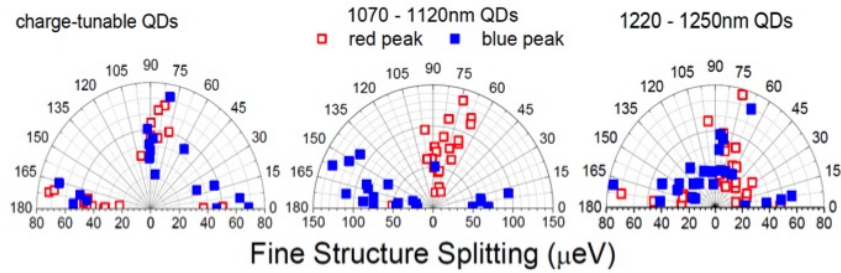


Figure 4.2.8: Polar plots showing FSS of different QD structures.

Figure 4.2.8 shows the polarisation from different samples, with the charge-tunable devices being grown by Sheffield, and the middle and right QDs being grown by NIST. The red and blue symbols represent the long ($2X^0$) and short (X^0) wavelength excitonic peaks respectively, with the angle measured being relative to the $[110]$ crystallographic axis. Again, the charge tunable QDs show a non-random alignment of polarisation, either along 0° or 90° .

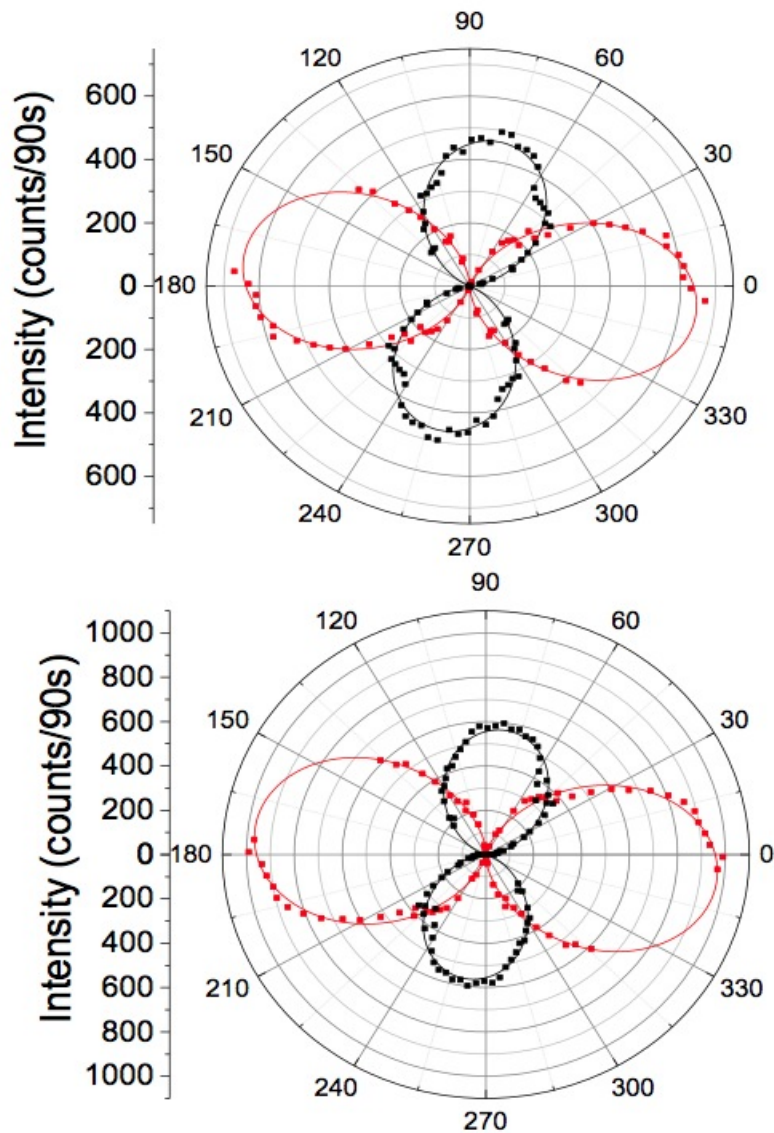


Figure 4.2.7: Figure showing corresponding polarisation plots of QD emissions as per figure 4.2.6.

This is somewhat mimicked by the central plot, with the distinction that the red and blue peaks are separated by their polarisation, with the blue peak aligning on 0° and the red peak on 90° . These non-random polarisation results indicate an anisotropy of the quantum dot being examined.

Figure 4.2.9 shows the tuning results from a number of different quantum dots. From this, we can surmise that each quantum dot reacts differently to

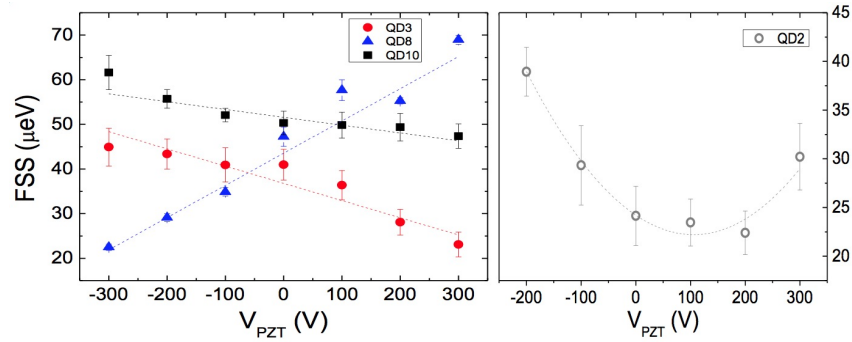


Figure 4.2.9: Multiple QD FSS Tuning

the tuning, with values varying from 8 μeV to 46 μeV . Sadly this isn't enough to eliminate the FSS for any of the dots measured, but shows potential for future samples. An interesting hypothesis could emerge from the data shown, however, with the left hand image showing a seemingly linear dependence in both a positive and negative gradient, but the right hand image showing a parabolic dependence through a minimum FSS. It is likely that the linear dependencies arise due to a lack of sufficient strain to tune the dots to their respective minima, something that is agreed upon in the literature[3, 12].

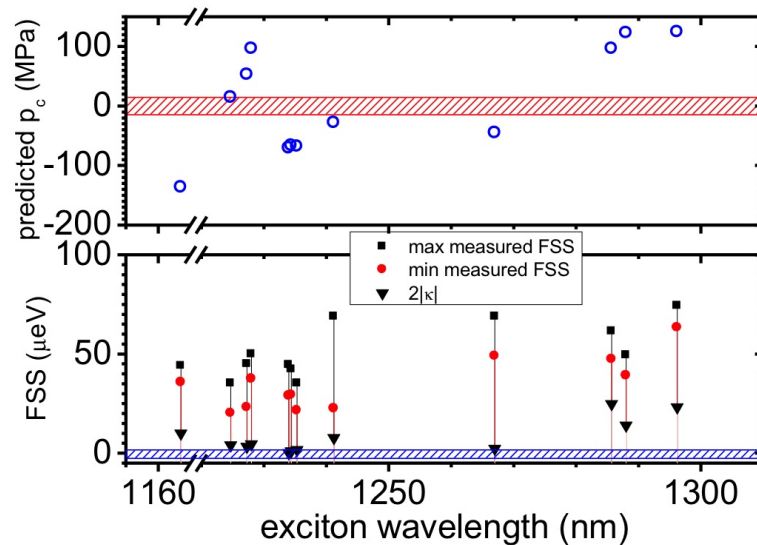
Figure 4.2.10: Graphs showing predicted critical stress, p_c , and required strain for minimum FSS of measured quantum dots.

Figure 4.2.10 shows predicted values for the critical stress values and the minimum FSS possible with applied stress for 12 quantum dots, based upon models from reference [7]. The red hatched area of the top graph shows the

attainable strain in the piezo stack, which shows that the current equipment cannot reduce the FSS as far as the theory predicts. The blue hatched area of the lower graph shows the desired FSS, something that 7 of the 12 measured QDs can reach if sufficient strain is applied, which shows promise for future entangled photon sources at telecom wavelengths.

4.3 Conclusion

Low density quantum dots presents a growth problem, with the required growth rate for single-dot spectroscopy being difficult to replicate on a run-to-run basis. This has been solved for small samples with the rotation stop growth method. Initial samples provided sufficient grading across the wafer for spacial resolving of individual QDs. These samples were GaAs capped, with lower wavelength emission being ideal for existing high-sensitivity silicon detectors. The challenge came when growing DWELL structures for telecommunication-wavelength applications, with recent advances in detector technology. Using a similar indium growth rate as the GaAs-capped samples, the grading across the wafer was considerably less pronounced, with dots being evident in large numbers even at the lowest-density part of the wafer. Even with this issue, single-dots were able to be spectrally resolved by Sapienza et al.[9] at Heriot Watt, showing that, contrary to previous measurements by other groups[5, 11, 14], individual dots at 1300 nm have low FSS, with fine tuning of the growth and experimental methods potentially paving the way for entangled-photon sources. Further growth tuning has provided a better grading across the wafer, with further FSS measurements outstanding from Heriot Watt. This shows that, with tailored growth processes, sufficiently low density QD samples can be grown for single dot measurements.

4.4 References

- [1] B Alloing, C Zinoni, V Zwiller, L H Li, C Monat, M Gobet, G Buchs, A Fiore, E Pelucchi, and E Kapon. Growth and characterization of single quantum dots emitting at 1300 nm. *Applied Physics Letters*, 86(10):101908, 2005.
- [2] W L Barnes, G Bjork, J M Gérard, P Jonsson, J A E Wasey, P T Worthing, and V Zwiller. Solid-state single photon sources: light collection strategies. *The European Physical Journal D - Atomic, Molecular and Optical Physics*, 18(2):197–210, February 2002.
- [3] A J Bennett, M A Pooley, R M Stevenson, M B Ward, R B Patel, A Boyer de la Giroday, N Sköld, I Farrer, C A Nicoll, D A Ritchie, and A J Shields. Electric-field-induced coherent coupling of the exciton states in a single quantum dot. *Nature Physics*, 6(12):947–950, October 2010.
- [4] Gabriel Bester, S Nair, and Alex Zunger. Pseudopotential calculation of the excitonic fine structure of million-atom self-assembled In_{1-x}Ga_xAs/GaAs quantum dots. *Physical Review B*, 67(16), 2003.
- [5] N Cade, H Gotoh, H Kamada, H Nakano, and H Okamoto. Fine structure and magneto-optics of exciton, trion, and charged biexciton states in single InAs quantum dots emitting at 1.3 μ m. *Physical Review B*, 73(11):115322, March 2006.
- [6] A G Cullis, D J Norris, M A Migliorato, and M Hopkinson. Surface elemental segregation and the Stranski–Krastanow epitaxial islanding transition. *Applied Surface Science*, 244(1-4):65–70, May 2005.
- [7] Ming Gong, Weiwei Zhang, Guang-Can Guo, and Lixin He. Exciton Polarization, Fine-Structure Splitting, and the Asymmetry of Quantum Dots under Uniaxial Stress. *Physical Review Letters*, 106(22):227401, May 2011.
- [8] P B Joyce, T J Krzyzewski, G R Bell, T S Jones, Surama Malik, D Childs, and Ray Murray. Effect of growth rate on the size, composition, and optical properties of InAs/GaAs quantum dots grown by molecular-beam epitaxy. *Physical Review B*, 62(16):10891–10895, 2000.

- [9] Luca Sapienza, Ralph N E Malein, Christopher E Kuklewicz, Peter E Kremer, Kartik Srinivasan, Andrew Griffiths, Edmund M Clarke, Ming Gong, Richard J Warburton, and Brian D Gerardot. Exciton fine-structure splitting of telecom-wavelength single quantum dots: Statistics and external strain tuning. *Physical Review B*, 88(15):155330, October 2013.
- [10] Ranber Singh and Gabriel Bester. Lower Bound for the Excitonic Fine Structure Splitting in Self-Assembled Quantum Dots. *Physical Review Letters*, 104(19), 2010.
- [11] A I Tartakovskii, R S Kolodka, H Y Liu, M A Migliorato, M Hopkinson, M N Makhonin, D J Mowbray, and M S Skolnick. Exciton fine structure splitting in dot-in-a-well structures. *Applied Physics Letters*, 88(13):131115, 2006.
- [12] R Trotta, E Zallo, C Ortix, P Atkinson, J D Plumhof, J van den Brink, A Rastelli, and O G Schmidt. Universal Recovery of the Energy-Level Degeneracy of Bright Excitons in InGaAs Quantum Dots without a Structure Symmetry. *Physical Review Letters*, 109(14):147401, October 2012.
- [13] Richard J Warburton, C Schäflein, Dirk Haft, F Bickel, A Lorke, Khaled Karrai, J M Garcia, W Schoenfeld, and Pierre M Petroff. Optical emission from a charge-tunable quantum ring. *Nature*, 405(6789):926–929, 2000.
- [14] M B Ward, P M Intallura, C M Natarajan, R H Hadfield, P Atkinson, Z L Yuan, S Miki, M Fujiwara, M Sasaki, Z Wang, B Baek, S W Nam, D A Ritchie, and A J Shields. Biexciton cascade in telecommunication wavelength quantum dots. *Journal of Physics: Conference Series*, 210:012036, March 2010.

SPIN POLARISED PLE ANALYSIS OF QUANTUM DOT OPTICAL SAMPLES

Quantum dots are being widely adopted in the field of “spintronics”, or spin transport electronics, which is, broadly, the exploitation of the spin of electrons in solid-state devices. If quantum dots are to be used in this manner, it is important to investigate the behaviour of spin in a typical quantum dot structure, particularly the spin relaxation mechanisms.

This experiment was inspired by the desire to analyse the behaviour of spin injection into QD samples. The previous chapter focused on quantum dot growth, and the applications for isolated dots, specifically looking at the carrier dynamics within a single QD. Whilst this chapter attempts to describe carrier behaviour in QD samples, it looks at QD ensembles, and the effect of carrier injection. QDs are looking extremely promising as candidates for quantum information processing (QIP), and, where the previous chapter looked at the FSS of QDs for quantum entanglement, this chapter aims to identify any spin loss mechanisms in a QD sample. This is due to the increased use of localised electron spins in semiconductors for qubits, that is, the spin-up or spin-down states of an electron can be used as encoding methods for the $|0\rangle$ and $|1\rangle$ states of a qubit. Retention of carrier spin within a semiconductor is, therefore, of great importance, and the focus of this chapter is to identify any common components in a QD sample that may cause loss of spin.

The previous chapter describes an anisotropy in the potential of single quantum dots, which affects the FSS. The FSS has also found to be linked

to the exciton spin relaxation rate in InAs/GaAs QDs [24], with the undesirable asymmetry in SAQDs causing both an increase in FSS and the mixing of bright excitons, which causes a reduction in spin-polarised-light emission.

5.1 Experimental Setup

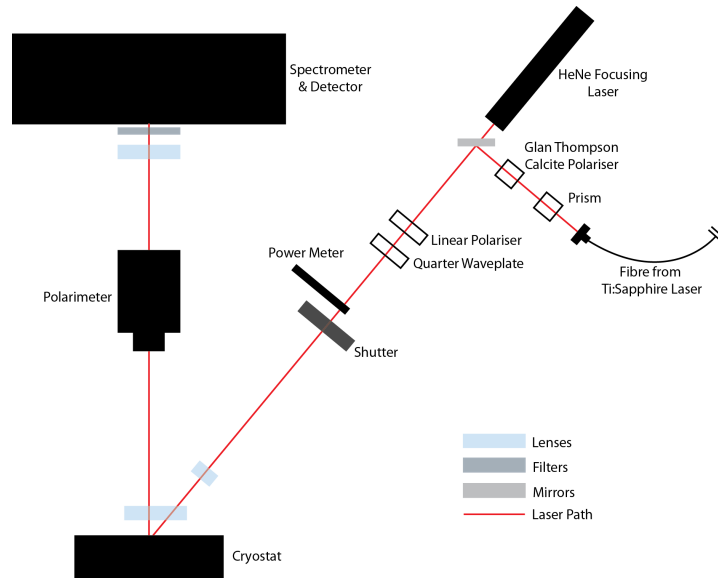


Figure 5.1.1: Spin PLE Equipment Schematic

PLE was briefly introduced in chapter 2, whereupon its similarity to PL was noted. Whilst this is largely true in terms of experimental set up, the data that is obtained can provide much more in-depth analysis of the optical properties of the semiconductor structure. As a measurement technique, it is often misunderstood; the intensity of the peak wavelength of an optical sample is quantified in relation to the wavelength of the optical excitation source. This differs in relation to an absorption spectrum, which details how well a sample absorbs different wavelengths of light, instead, PLE describes the effect of absorption at varying wavelengths in relation to the excitation of carriers at a certain energy and recombination at the emission energy of a sample.

The main challenge for PLE experiments can be in obtaining a suitable variable-wavelength source. The easiest method of achieving this is by using a white light source (such as a tungsten filament light) and an accompanying monochromator to filter the white light into a changeable monochromatic

source. This method suffers from a lack of true monochromaticity and often a low emission power, due to the light emitting at a high power across the optical spectrum. The alternative is a tuneable laser. This method manages to solve the problems of the white light source at the expense of the breadth of wavelengths for emission, with the wavelength being limited by the source laser and the mirror set available.

Another difference between PL and PLE is the lack of variation in the detection wavelength for the latter. To determine a suitable detection wavelength for each PLE experiment, a PL spectrum is first taken, and that the intensity of the emission peak can be measured. The different types of detector available play a large part in different methods of measuring emission intensity. Detectors measuring individual wavelength steps via a monochromator are fixed at the peak wavelength only, whereas array detectors such as that used in the following experiments are able to detect a range of wavelengths at once, and thus the average across a peak can be taken instead of the peak value.

Figure 5.1.1 shows the experimental set up for spin-based PLE. This measurement uses the same principles as PLE with the simple change of injecting circularly polarised ($\sigma+$) light, and detecting the degree of polarisation of the emitted light (ρ), defined as the proportion of an electromagnetic wave that is polarised i.e. for a fully polarised wave $\rho = 100\%$. In this way, it is possible to determine the areas of carrier generation and how much spin is lost through provision of carriers to the quantum dots for light emission, because exciting a sample with circularly polarised light transfers a spin to the excited carriers. All measurements are taken with the samples at 10 K, using a closed loop cryostat. The excitation source is a Ti:Sapphire laser with a mirror set allowing a wavelength range of 780 nm to 880 nm .

As changing the wavelength of the Ti:Sapphire excitation laser often means a changing power level, a Glan Thompson Calcite Polariser and power meter are used in collaboration to ensure an excitation source that is approximately constant- 1 mW being the target power in this case, with an error of $\pm 5\%$. The linear polariser and quarter waveplate are used in conjunction to ensure the light is entirely circularly polarised. The polarimeter allows for analysis of the Stokes parameters, which describe the nature of the polarisation of

the emitted light from a sample. The output from the polarimeter and detector are then combined to describe the average intensity and polarisation emitted from the sample at the peak of the PL, describing both of these qualities across the excitation spectrum.

As per Pryor and Flatté [20], we are measuring along the growth direction, which gives “near unity conversion of spin to photon polarisation and is the least sensitive to uncertainties in SAQD geometry”.

5.2 Theory

The primary objective of this measurement was to identify the most significant sources for spin relaxation in a QD sample. Using PLE in this manner is beneficial due to its ability to excite different parts of a sample by changing the excitation wavelength, with the accompanying polarisation showing whether or not exciting a spectral range (such as the GaAs bulk or wetting layer) retains more or less spin than expected.

5.2.1 Selection Rules

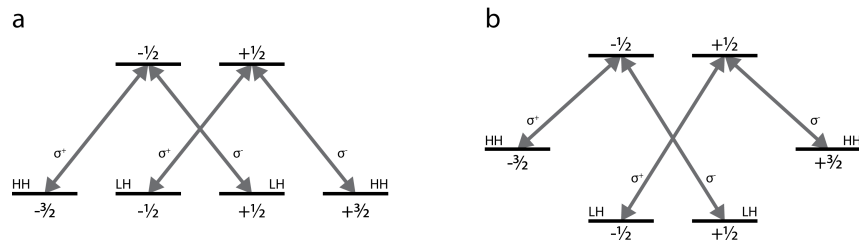


Figure 5.2.1: Selection rules in a) degenerate and b) non-degenerate systems

When considering spin loss in a system, it is important to determine whether the active region is degenerate or non-degenerate (Figure 5.2.1), noting the states involved when looking at the photoexcitation of carriers with circularly polarised light. The values associated with each state shown in figure 5.2.1 are the projection of angular momentum (J_z), calculated by using the sum of the quantum numbers s (spin) and l (orbital) of the associated carrier. In the conduction band (CB), electrons have quantum numbers $s = \pm 1/2$ and $l = 0$, therefore meaning that their angular momentum is $J_z(e_{CB}^-) = \pm 1/2$.

In the valence band (VB), electrons have quantum numbers $s = \pm 1/2$ and $l = 1$, so, for Heavy Holes (HH), $J_z(h_{HH}) = \pm 3/2$, as, in this case, $s = \pm 1/2$ and $l = \pm 1$, whereas for Light Holes (LH), $J_z(h_{LH}) = \pm 1/2$, with $s = \pm 1/2$ and $l = \mp 1$. The arrows in figure 5.2.1 show the transitions that can occur whilst conserving angular momentum ($\Delta J_z = \pm 1$ for $\sigma = \pm 1$).

In order for a recombination to retain the spin of an excitation photon with $\sigma = \pm 1$, the downward transition must be taken into consideration. If we consider an electron in the CB with $J_z = +1/2$, which has been excited by $\sigma+$ light, there are two potential routes for the electron to take when relaxing. If it relaxes into the heavy hole state, the spin will be retained- the outgoing photon will have the same spin as that of the incoming photon. However, if the electron relaxes into the light hole state, the spin is the opposite of the incoming photon, thus nullifying the spin.

In a degenerate system (figure 5.2.1a), there is a 3:1 ratio in the probability of a heavy hole transition compared to a light hole transition [21, 23]. Looking at the probability of spin polarisation generation for $\sigma+$ excitation, $\rho = \frac{(\sigma^+ - \sigma^-)}{(\sigma^+ + \sigma^-)} = \frac{(3-1)}{(3+1)} = 50\%$, meaning that there is a maximum 50% chance of spin retention in a degenerate system. Looking at a non-degenerate system (figure 5.2.1b), the heavy hole state is lifted, essentially splitting the HH and LH bands and enabling excitation from only one sub-band, namely the HH band. This leads to a maximum 100% spin retention from a non-degenerate sample: $\rho = \frac{(\sigma^+ - \sigma^-)}{(\sigma^+ + \sigma^-)} = \frac{(3-0)}{(3+0)} = 100\%$. These values are the maximum spin retention possible, with the reality being that, in any sample, there are going to be a number of spin loss mechanisms that will reduce that number.

In a solid state system, non-degeneracy is achieved through strain and/or quantum confinement, with a quantum dot system providing both of these properties, particularly in the heavily strained pseudomorphic wetting layer. Therefore, if exciting carriers through the wetting layer, one would expect a considerable increase in spin retention when compared to carriers excited from bulk, unstrained material.

PLE is not a straightforward absorption measurement, with the intensity measurement showing not the direct absorption, but the intensity of emission from a chosen optically active structure within a sample. In this

case, the ground-state emission from a quantum dot is used as the intensity measurement, with excitation ranging from just above the GaAs band-edge to above the HH state of the wetting layer. The ground state emission of the quantum dot [15, 17, 19, 20] is largely a heavy-hole transition due to the large confinement and strain fields involved in the self-assembly process, which means that a forced LH excitation will result in an emission from the quantum dot that is of the opposite polarisation to that of the excitation source. This is dependent on the direction of emission, as other authors [1–3, 45–47] have discussed the mixing of hole states in QDs, but [20] describes the growth direction as the most reliable source of HH recombination. It is important to note that carriers recombining in the quantum dots are excited elsewhere, so there is a period of time between excitation and recombination during which the electron spin can change (depending on spin loss mechanisms).

5.2.2 Spin Loss Mechanisms

Given the nature of the samples and the spectral range across which the samples will be excited, the spin loss mechanisms are complex. Decay times T_1 and T_2 are used to describe the loss of spin information, with each time being dependent on multiple variables. T_1 is the “longitudinal spin relaxation time” [29], which is the time that a spin ensemble takes to reach thermal equilibrium; T_2 is the spin decoherence time, which describes the time that it takes for coherent spin to change its phase after a scattering event.

Bulk and QW structures have different spin loss mechanisms compared to QDs. Two mechanisms are dominant in these domains, the D’Yakonov-Perel mechanism and the Elliot-Yafet mechanism, both of which are suppressed in QDs. The D’Yakonov-Perel mechanism describes a spin-splitting of electron states, which behaves as a \mathbf{k} -dependent effective magnetic field. The Elliot-Yafet mechanism describes spin loss due to a change of momentum due to scattering, usually thanks to phonons or impurities.

The mechanisms that dominate in bulk/QW systems are suppressed in QDs, with the dominant processes leading to spin loss being due to the electron-hole exchange interaction, and the hyperfine interaction. The spins

of electrons and holes can couple by the exchange interaction between electrons (and to a lesser extent, holes) and the atomic nuclei, leading to a mixing of the bright excitons, $|+1\rangle$ and $|-1\rangle$ (excitons which give circularly polarised emission). This mixing results in less distinct states defined by $\frac{1}{\sqrt{2}}(|+1\rangle \pm |-1\rangle)$, whose difference is the FSS, and are also linear polarised. This electron-hole exchange interaction mechanism is enhanced by the asymmetry of the dots, and the strong confinement, but can be lessened, similarly to the FSS, by application of an external magnetic field [4, 30]. Doping the QDs can also counteract this mechanism [5–11, 18]. High magnetic fields (> 4 T) have resulted in such a significant reduction in the effect of the electron-hole exchange interaction, T_1 has been reported as high as 1 ms [12, 14].

T_2 in QDs is largely dependent on the non-uniformity of the hyperfine interaction [13] within the QD, and, unaltered, is typically of the order of ns. Dynamical nuclear polarisation (DNP) uses circularly polarised light to “write” a polarisation to the electron spin in the QD, which, via the hyperfine interaction, can transfer the polarisation to the nuclear spin ensemble. The alignment of the nuclear spin ensemble increases the coherence time of the electron. This process has yielded an extension of T_2 approaching 1 μ s. The spin loss times were not measured in this experiment due to a lack of time-resolved PL equipment that is needed for such measurements.

With the spin loss mechanisms in both bulk and QDs, the polarisation retention in a QD system is not going to reach the theoretical maximum without particular conditions and a tailored growth structure. The structures used for this experiment are existing light emission structures, optimised not for spin retention, but for wavelength-specific emission. The idea behind this experiment is to see how these structures perform in terms of their spin retention; no doping has occurred in these samples, nor any magnetic fields applied. A circularly polarised light source is used in this experiment in order to determine the loss of spin through the structure in terms of the degree of polarised light that is emitted by the quantum dots, as defined by

$$P_{circ} = \frac{I(\sigma^+) - I(\sigma^-)}{I(\sigma^+) + I(\sigma^-)} \quad (5.2.1)$$

Where $I(\sigma^\pm)$ is the intensity of the light, with the σ^\pm denoting the polarisation. Decay times T_1 and T_2 are not calculated, as that would require time-resolved PL.

Expected luminescence lifetimes of carriers in QD samples are of the order of 1 ns [18], with spin lifetimes proving to be shorter in un-optimised QD samples [29], typically of the order of ps, although spin times have been reported up to 1 ns [34–37]. Assuming that the spin life time in the samples to be analysed is comparable to that of the luminescence lifetime, spin polarised light should be emitted.

5.2.3 Analysis of the Spin PLE Plot

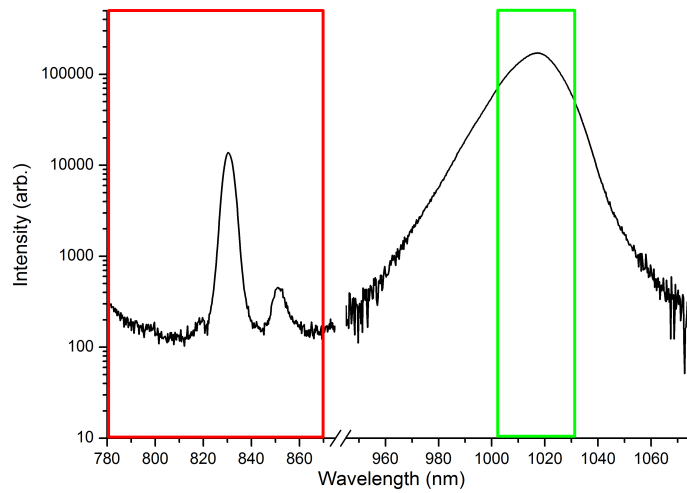


Figure 5.2.2: PL Spectrum showing the excitation (red) and detection (green) areas of this experiment: Note that the detection varies per the emission of the sample

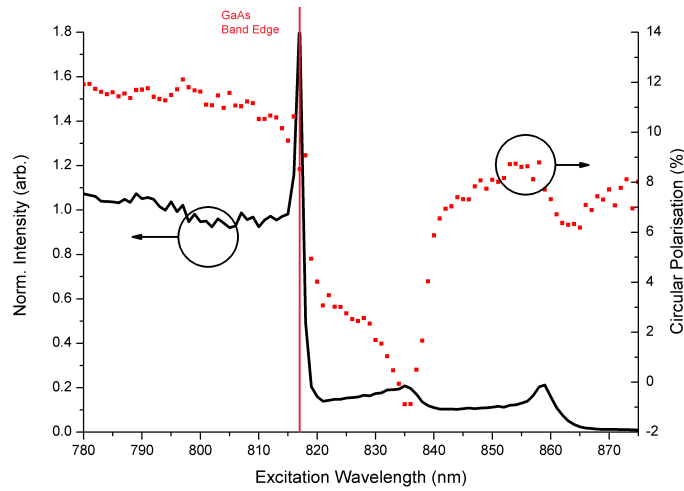


Figure 5.2.3: Example of the output of a typical spin PLE scan

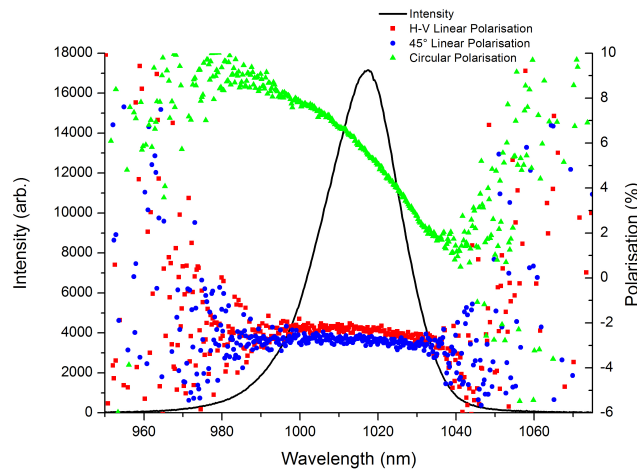


Figure 5.2.4: PL with polarisation.

Figure 5.2.2 shows, in the red rectangle, the range of excitation available being from 780 nm to 870 nm using this particular experimental setup, as described in section 5.1. The green rectangle is an example of the collection range for the PL intensity used in the PLE output measurement. This is the benefit of using an InGaAs array, as a snapshot of selected wavelengths are taken over a desired time, instead of the need for collection of individual wavelength measurements via a monochromator, with PLE usually sitting at a single wavelength as mentioned previously. As well as the PL being measured, the polarimeter allowed for a thorough measurement of the emitted light from the sample, by means of analysing the Stokes parameters, and

thus quantifying the horizontal-vertical (H-V), 45° and circular polarisation across the entire measured PL.

Figure 5.2.3 shows the typical output data from the spin PLE set up: an individual measurement is performed at nanometre steps of the excitation wavelength, with each measurement outputting the PL intensity and polarisation details averaged over a range of wavelengths dependent on the peak of the PL (an example of the measurement is shown in figure 5.2.4). Note that the sample as described in figure 5.2.2 is different to that in figure 5.2.3, because, in the former, there was a need for the emission from the WL and a nearby QW to be measured (described in section 5.3.4), but the PLE is more complex. The reason for the large spread in polarisation values outside the PL peak is the lack of measurable light being emitted, and is also why the averaged values taken for the PLE measurement does not encompass the entire PL spectrum. It may be noted that the two linear-based polarisation measurements are non-zero- this is due to a very slight misalignment, something that does not affect the circular polarisation, which, alongside the PL intensity, is the measurement of interest. The slope in the circular polarisation is indicative of Fine Structure Splitting in the quantum dots, with the overall polarisation from a quantum dot ensemble being affected by an imbalance in spin population from the σ^+ excitation [39].

Using the example in figure 5.2.3, the intensity peaks can be identified (with the aid of the polarisation). From left to right: The peak at 797 nm is assumed to be a shallow state from the AlGaAs barriers- the peak in polarisation rules out a LH peak and HH peak (due to the energetic position of the peak in polarisation relative to the respective PLE intensity peak compared to the HH peak), and the energy of the peak lends credence to this hypothesis, as it is higher than that of the GaAs band-edge. The next peak between 816 nm and 817 nm matches the GaAs bandedge energy at about 10 K- 1.52 eV. There is a considerable drop in PLE intensity after passing the GaAs band edge due to reduced absorption, but there are two definite peaks. The first, at ~835 nm, is the LH state. This is clear due to the abrupt dip in polarisation which coincides with the intensity peak, with the following rise in polarisation coinciding with the HH peak at ~859 nm.

	Example PLE	Lee et al						Gerard et al.
		1 ML		2 ML		3 ML		1.2 ML
C ₁ -HH ₁	1.443	1.468	1.468	1.415	1.391	1.390	1.365	1.450
C ₁ -LH ₁	1.485	1.477	1.491	1.461	1.456	1.444	1.434	1.485
Difference	0.042	0.009	0.023	0.046	0.065	0.054	0.069	0.035

Table 5.2.1: Energy Values for HH and LH states compared with Lee et al[22] and Gerard et al.[40] All values are in eV.

These values appear to agree with the literature on the subject, with Lee et al. [22] and Gerard et al. [40] growing highly strained InAs QWs and determining the energy of the different states. Table 5.2.1 shows the comparison with the literature and our example sample, although it must be noted that the literature used highly strained quantum wells, and our samples are looking at the wetting layer of a quantum dot sample, which is a much more complex structure given the strain relaxation due to the dots and the lack of certainty over the composition of the wetting layer, quantum dots and surrounding material. C₁ refers to the first state of the conduction band, HH₁ and LH₁ are the first sub-bands of the heavy and light holes respectively.

5.3 Practical Results

A variety of samples were analysed using spin PLE as a result of the combination of polarisation analysis and PLE being relatively untested. The spin PLE intensity data is normalised so that sets of samples can be compared on the same plot.

5.3.1 "Standard" QD Samples

2.4 ML InAs QDs
10Å GaAs (VN2117) 10Å 17% InGaAs (VN2116)
500Å GaAs
500Å 31% AlGaAs
90Å GaAs
60Å GaAs (VN2117) 60Å 17% InGaAs (VN2116)
2.4 ML InAs QDs
10Å GaAs (VN2117) 10Å 17% InGaAs (VN2116)
150Å GaAs
500Å 31% AlGaAs
2000Å GaAs Buffer
GaAs Substrate

Figure 5.3.1: Structure of "standard" QD samples, chosen for their excellent PL emission.

The first samples to be analysed were "standard" PL QD samples- one GaAs capped, the other InGaAs capped, although otherwise the same (Figure 5.3.1). These samples were picked to try and set a benchmark for the spin PLE measurement, as they are the most basic forms of QD sample grown in the NC. A potential problem could occur in that the GaAs surrounding the active QDs and between the AlGaAs barriers is only 30 nm, which may cause a considerably diminished absorption of carriers into the QDs, as well as potential interference from shallow states in the surrounding AlGaAs. Each of these samples was optimised for emission, so although the AlGaAs barriers may affect the PLE negatively, they were included to prevent carrier loss at elevated temperatures for room temperature characterisation in other experiments. The uncapped QDs on top of the sample were used for AFM analysis which is not included in this thesis. These samples were earmarked as excellent emitters, and therefore it was thought that they would be ideal candidates for the spin PLE experiment. The expectation from these samples was that a small amount of polarisation be retained by the bulk, with excitation into the heavy hole state of the wetting layer providing more polarisation out, as per the selection rules. The DWELL sample potentially provides an extra state for excited carriers to relax into, therefore meaning

that there is a higher probability for spin loss due to the deeper confining potential of the QDs, and the extra state provided by the surrounding QW.

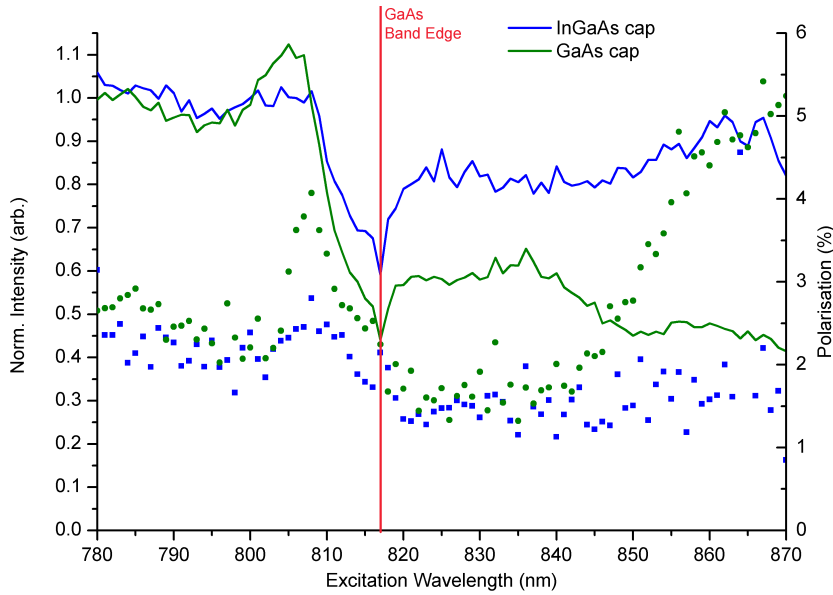


Figure 5.3.2: Spin PLE plot of the “standard” samples as described in figure 5.3.1. Solid line plot represents the normalised intensity of the PLE for each sample (left axis), with the scatter plot representing the polarisation value of the emission at the corresponding excitation wavelength (right axis). The corresponding wavelength to the GaAs band edge is labelled in red.

The PLE shown in figure 5.3.2 did not reveal much in the way of the spin retention of the quantum dots, other than the fact it is particularly low- only a maximum of 5% of the emitted light was circularly polarised, and that was in the GaAs capped sample. This is assumed to be because the measurement taken is using continuous wave (cw) PL (as opposed to time resolved PL), which means that the spin lifetime needs to be of a similar length to the luminescence lifetime, as mentioned in section 5.2.1. The PLE showed a curious in that the expected GaAs bulk band-edge exciton peak is superseded by what is assumed to be a state from the AlGaAs barrier- the 817 nm drop in intensity coincides with the expected wavelength of the GaAs band-edge, and there is a small variation in polarisation, compared to the rise in polarisation in the broad intensity peak seen at approximately 805 nm. This is assumed because the peak in intensity is above the GaAs band edge, meaning that any emission/absorption in this region is not confined by the InAs QDs/WL or the GaAs itself. Looking at the literature [16, 44], there is

no energy to correspond to the peak at the appropriate energy, nor for the respective peak in subsequent samples.

There are no obvious absorption peaks for the LH or HH bands, although there is a rise in the polarisation at the point where the HH is expected to be in the GaAs sample. It is interesting to note the apparent comparative lack of emitted spin polarised light from the InGaAs capped sample. The lower strain in the wetting layer compared with the GaAs capped samples, may cause the HH and LH states to behave differently energetically, with the states of the well being dominant, and also redshifted compared to the WL, potentially outside of the excitation range being used. There isn't a definitive peak for either LH or HH in terms of the PLE intensity for the DWELL sample, with only a polarisation peak at the same point as the shallow AlGaAs state, indicating that, in this case, the WL may not have been excited.

The assumed reason behind the lack of intensity when exciting bulk GaAs in these samples, is that there is a small amount of GaAs within the excitation region, i.e. between the AlGaAs barriers, particularly in the InGaAs capped sample. This is corroborated by the comparison between the compared intensity above and below the GaAs band edge for each sample- the InGaAs sample has little variation above and below the 817 nm mark, barring a large peak at ~ 805 nm. The GaAs capped sample has a larger difference between the two sections and a rather more pronounced peak at the 805 nm mark. It may be noted that there doesn't appear to be any distinctive intensity peaks representing the HH/LH states, and the low polarisation value across the measurement makes their energetic position difficult to determine.

This experiment confirmed that, with cw circularly polarised excitation, QDs do emit spin polarised light, meaning that the spin lifetime of carriers in these samples is comparable to that of the luminescence lifetime. This polarisation is similar for both samples over most of the excitation range, although the heavy hole state in the WL of the GaAs sample is evident by means of a rise in polarisation. This polarisation behaviour is as expected for the GaAs capped sample, with the InGaAs sample requiring more investigation, potentially with a larger excitation range.

As the excitation range of this equipment is limited and difficult to change, it was decided to continue the spin PLE investigation looking at GaAs capped samples, particularly as spin polarised light was emitted by a previously measured sample. As the excitation range covers the GaAs band-edge and WL states, it was decided to investigate the effect of increased indium deposition with the QDs themselves being truncated, reducing the effect of any large change in QD ground state, but allowing an increase in the QD base size.

5.3.2 Indium Coverage Samples

x ML InAs QDs
500Å GaAs
500Å 31% AlGaAs
125Å GaAs
25Å Low Temperature GaAs Cap
x ML InAs QDs
150Å GaAs
500Å 31% AlGaAs
2000Å GaAs Buffer
n+ GaAs Substrate

Figure 5.3.3: Structure of “In-coverage” sample set, with each sample’s In deposition time varying, resulting in an In coverage of x monolayers.

To ascertain the effect of varying the amount of indium being deposited, another sample set varied the In coverage (also with a set In-flush cap height of 2.5 nm), as shown in figure 5.3.3. Similar to the QD samples seen in section 5.3.1, there is only 15 nm GaAs between the AlGaAs and QDs, it is expected that this will have an effect on the PLE shape. x in this sample structure represents the variation in the amount of indium deposited, where $x = 1.75$ ML, 1.95 ML, 2.14 ML, 2.34 ML and 2.53 ML. These samples were initially used as an investigation of the effect of indium deposition in an attempt to describe the process of QD growth vs. In deposition. There was another sample in this set where $x = 1.53$ ML, but, as quantum dots typically form at $\theta_{InAs} > 1.7$ ML, the emission of the sample was from the emer-

gent wetting layer behaving as a thin QW, coinciding with the excitation wavelength range, meaning that it could not be analysed using this technique. These samples have been previously described in section 3.2.1, with AFM analysis of the QD heights showing little variation in terms of the number of dots, but rather the changing distribution of size in the ensemble. The cap height does somewhat limit the variation in electronic states (and therefore emission wavelength), but the base size variation remains as well as any change in wetting layer. As these samples have a similar amount of GaAs in the confining region (30 nm), it is expected that there will be a comparative lack of emission from the GaAs excitation, with emission due to excitation of shallow AlGaAs states expected to dominate as per the “standard” sample set.

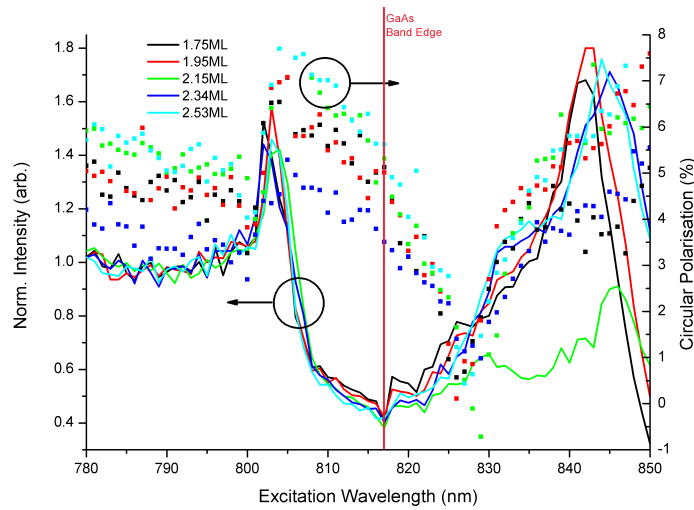


Figure 5.3.4: Spin PLE for Indium Coverage Samples (structure described in figure 5.3.3). Solid line plot represents the normalised intensity of the PLE for each sample (left axis), with the scatter plot representing the polarisation value of the emission at the corresponding excitation wavelength (right axis). Values listed refer to the amount of indium deposited on each sample in monolayers.

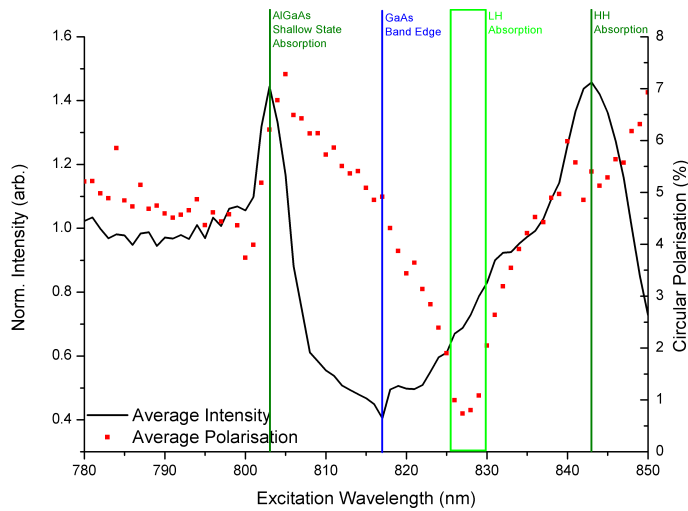


Figure 5.3.5: Plot showing the averaged values of both the normalised intensity and polarisation as shown in figure 5.3.4. This was done to highlight any trends and reduce the effect of noise when analysing the plot. Labelled on this graph are the assumed positions of each state excited across the excitation range, including the AlGaAs shallow state, GaAs band-edge exciton, LH (unable to clearly define) and HH.

As expected, these results resemble those seen in section 5.3.1, with a large peak from the AlGaAs shallow states at 803 nm (including a rise in polarisation) and a dip at the 817 nm GaAs band-edge exciton point. The difference between these samples and the “standard” QD samples comes in the form of a much higher polarisation value across the excitation range, allowing a clear dip in polarisation at the LH position, although again, there appears to be low definition in the intensity peaks when considering the position of LH and HH band absorption, save for the 2.15 ML sample, which has two clearly defined peaks at ~ 830 nm (LH) and ~ 845 nm (HH). Once again, a dip in intensity is seen at the energy of the GaAs band-edge exciton. This is assumed to be a result of minimal GaAs between the AlGaAs barriers and enclosing the optically active QDs- the dip at 817 nm maybe due to short carrier lifetime at the GaAs band-edge, in other words, the carriers excited at this point are not recombining in the QDs as desired, with a decrease in QD emission seen. This intensity dip at the GaAs band-edge also suggests an inefficient, non-radiative process when exciting at the corresponding energy-carriers are being excited but the efficiency of their transfer to the quantum dots is low compared with other samples and the WL states. That being said, the QDs are still emitting, and the polarisation increases at the GaAs band-edge, suggesting a fast carrier lifetime or longer spin lifetime.

The apparent increase in polarised emission could be attributed to sample-to-sample differences, as the range of maximum polarisation values measured varies from 5% to 8%, which means the standard sample is in this range. The LH excitation is made apparent in this set of samples, as shown by a drop in polarisation at ~ 827 nm across the range. This occurs because, as explained previously in section 5.2.1, optical transitions in QDs are largely heavy-hole based, and excitation into the LH would reverse the spin of the emission compared to the excitation. This potentially indicates that the carriers generated at the WL LH relax to the QDs fairly efficiently, as the spin of the carriers is reflected in the emission from the QDs.

As the behaviour of the intensity and polarisation is largely homogeneous across this set of samples, an averaged plot was used to better ascertain an approximation for the overall behaviour. Note that this does not reflect absolute values, but is used to discern trends from noise across the samples, enabling an estimate for the energy levels in the sample set, as is labelled in figure 5.3.5. Figure 5.3.5 shows a sharp rise for the shallow state of the AlGaAs barriers at 803 nm, a decline in polarisation approaching zero between the GaAs band-edge (817 nm) and the light hole (~ 827 nm), with a subsequent rise for the heavy hole. This indicates that the deposition of material after the pseudomorphic wetting layer has little effect on the loss of spin when exciting into the GaAs bulk or WL, potentially pointing towards the wetting layer being a feature of fixed dimensions- the same for each of these samples, or at least towards the theory of a confining layer[38], dimensions in this case limited by the height of the cap (which is limited to 2.5 nm).

The lower absorption from the GaAs bulk is again attributed to the comparative lack of material between the AlGaAs barriers, with any excited carriers from GaAs outside of the barriers not contributing to the emission in a significant manner. The GaAs within the active region may also be disordered due to being surrounded by the aforementioned AlGaAs and containing the highly strained QDs. The GaAs cap itself will be of lower quality due to the low substrate temperature during the growth, leading to 27.5 nm out of 30 nm being grown at the correct temperature, and the large strain field potentially affecting the remaining material. Tomič et al. [42] note that

strain templating of bilayer dots extends up to 10 nm into the cap layer, with the effect completely negated at 50 nm [43]. Significant effects remain up to 20 nm however [25, 27, 28, 41–43], albeit reduced, and given that the AlGaAs layer is only 15 nm from the QDs, both the GaAs cap and AlGaAs barriers could be affected by the strain field of the QDs.

Using the averaged plot, it may be useful to see if there are any parallels between this sample set and the previous GaAs capped sample. Figure 5.3.6 shows the PLE data for the standard samples and the averaged PLE data for the coverage samples. One clear parallel is the dip in intensity at 817 nm; the GaAs band-edge and at the increase in polarisation at longer wavelengths (attributed to HH excitation). There is also a rise in polarisation at the low energy side of the AlGaAs shallow state intensity peak, and subsequent dip. The measurement of the coverage samples was affected by overlap of the emission wavelength and the excitation, hence why the excitation range stops at 850 nm.

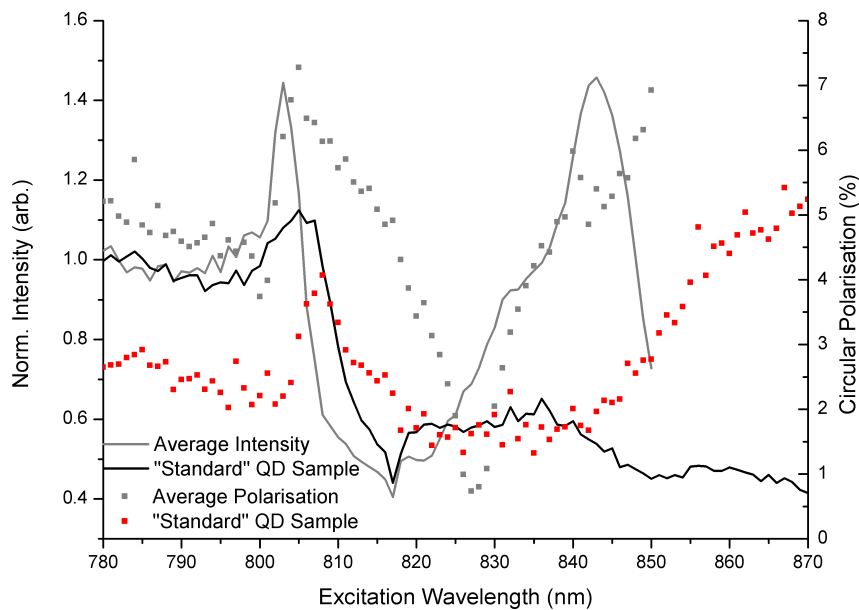


Figure 5.3.6: The averaged plot as seen in figure 5.3.5 (grey) compared to the GaAs capped sample discussed in section 5.3.1 (black/red).

It remains to be seen whether the ground state energy of the QDs has an effect on the spin polarisation, with the difference in behaviour in the previous samples being potentially multi-faceted, in particular, with the lower strain and intermediate states caused by the enclosing QW coming into

play. As mentioned in section 3.2.1, the easiest method of changing a QD's wavelength is to alter the cap height. This should help indicate whether or not the change in behaviour was as a result of QD-based parameters.

5.3.3 In-Flush QD Samples

2.4ML InAs QDs
650Å GaAs
y Å Low Temperature Variable GaAs Cap
2.4ML InAs QDs
650Å GaAs
1000Å 35% AlGaAs
3000Å GaAs Buffer
GaAs Substrate

Figure 5.3.7: Structure of “In-flush” sample set, with each sample's GaAs cap represented by the variable y nm.

The sample structure as shown in (Figure 5.3.7) refers to a set of In-flush samples grown under identical conditions, only varying the wavelength of the emitted light by altering the cap: y in this case is the variation in height of the low temperature GaAs cap, with the five samples spanning the values $y = 2.5$ nm, 3 nm, 3.5 nm, 4.5 nm and 5.3 nm. These samples were shown earlier in the thesis as an example of the effect of the In-flush method on PL emission in section 3.2.2, and are also mentioned in appendix A, showing a change in emission from 950 nm to 1150 nm (a change in emission energy of ~ 65 meV). The PL as shown in section 3.2.2 indicates a change in the electronic levels in the QD samples, with the samples with a lower cap height having a shallower confining potential, and a higher ground state energy. These samples were analysed to see if there is any change in the spin retention compared to this change in the electronic levels of the dot: does changing the ground state by this ~ 65 meV affect the overall polarisation? This should help determine whether or not spin loss occurs before or during the carrier capture as opposed to in the QDs themselves.

Figure 5.3.8 shows the results from the samples in the varying indium flush set, although no data was gathered for the 2.6 nm cap due to the

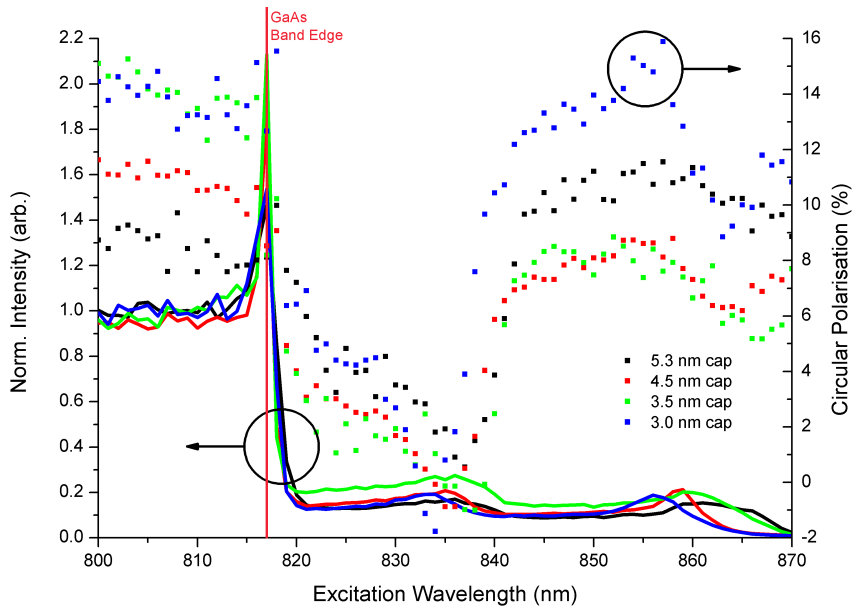


Figure 5.3.8: Varied In-Flush QD PLE data. Samples described in figure 5.3.7. Solid line plot represents the normalised intensity of the PLE for each sample (left axis), with the scatter plot representing the polarisation value of the emission at the corresponding excitation wavelength (right axis).

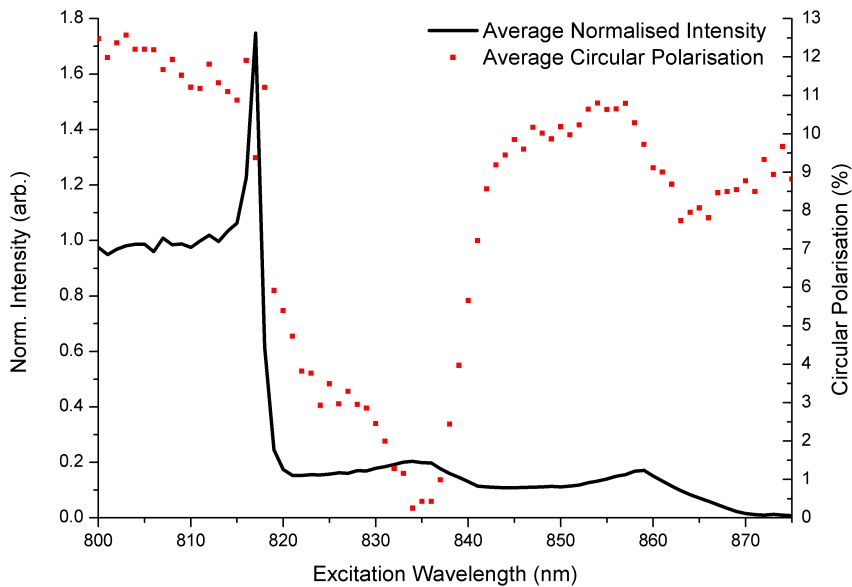


Figure 5.3.9: Plot showing the averaged values of both the normalised intensity and polarisation as shown in figure 5.3.8. This was done to highlight any trends and reduce the effect of noise when analysing the plot.

QD emission coinciding with laser scatter from the excitation source. The GaAs band-edge exciton is more prominent on this set of samples, with a clear intensity peak at 817 nm ($= 1.52$ eV). Other than the very clear GaAs

band-edge exciton peak, there are two clear peaks at ~ 835 nm and $\gtrsim 855$ nm (greater variation on this peak), which, as stated in section 5.2.3 are assumed to be LH and HH peaks respectively. It may be noted that the polarisation levels are considerably higher than the previous samples, with the main difference in these samples being the lack of upper AlGaAs barrier, which potentially changes the carrier lifetime; and a larger amount of GaAs in the excitation region.

It may also be noted that, as with previous samples, the polarisation of the HH excitation and the polarisation from the GaAs bulk excitation do not behave in the manner expected according to the selection rules (as mentioned in section 5.2.1), the initial spin injection from the HH is expected to be twice as high as that from bulk material, with the 4.5 nm and 3.5 nm cap height samples showing a decrease in polarisation when exciting into the HH. The polarisation emitted from this sample is considerably higher than that of the previous samples. This is assumed to be because of the lack of upper-AlGaAs barrier, meaning that the excitation region is not limited, and there is less influence from AlGaAs shallow states as were seen in the previous sample sets. This is certainly true regarding the intensity plot, with a clearly defined peak at the GaAs band-edge exciton energy, and less intensity at lower energy due to comparatively less material volume for excitation beyond the GaAs band-edge. There does not appear to be a shallow state from the lower AlGaAs barrier, with neither the intensity nor the polarisation indicating anything at a higher energy than the band-edge. As far as sample-to-sample variation is concerned, there does not appear to be a correlation with the polarisation of the emission and the cap height, although there is a range of polarisation across the samples- the highest polarisation at 15% from the HH state in the 3.0 nm sample and the GaAs bulk in the 3.5 nm sample. This would indicate that varying the energy levels of the QDs does not alter the spin relaxation when exciting into the GaAs bulk and WL states, in fact the greater effect seems to be due to the amount of material in the excitation range, as well as the proximity of the AlGaAs barriers, as there is seemingly no influence from the AlGaAs barriers in these samples, unless it is outside of the excitation range used.

The difference between the In flush samples and the previous two sets of samples shows that a significant effect is made by the amount of material in the excitation/optically active region of the sample makes a significant difference to the intensity, with AlGaAs shallow states from the surrounding barriers affecting the emission above the GaAs band edge, and the overall polarisation. The In-flush samples intensity from excitation above the GaAs band edge is ~ 5 times greater than that of excitation of the WL, up to ~ 9 if the large peak at the band-edge is taken into account. This is in stark contrast to that of the previous samples, where the intensity above and below the GaAs band-edge is very similar, with a dip at 817 nm. The similarity between these sets of samples is primarily in the dimension of the active structures, namely the WL and QDs. Using the coverage samples as a comparison, the main difference is the volume of GaAs available for excitation around the active region. As the In-flush samples have 65 nm of material below and above the QDs, one can assume that crystal disorder and strain has reached the limit of its influence, meaning that the absorption and carrier generation in the GaAs bulk will be much improved.

As the samples do not appear to show great variation in terms of the shape of polarisation and intensity plots, it was decided to average each of the plots (figure 5.3.9) to aid the identification of trends in the data as opposed to absolute values (particularly as the polarisation of both the bulk and HH vary), with peaks and troughs being confirmed instead of being dismissed as noise. As mentioned previously, the polarisation at the HH state appears to be equal to, if not lower than, the polarisation from the bulk GaAs, though the LH state is confirmed, with a dip in polarisation coinciding with an intensity peak. This agrees with analysis from the previous sample set, that excitation resonant with the LH state is inefficient in terms of spin retention, with the polarisation value dipping to zero.

The past two sample sets appear to show that QD and WL parameters do not affect the spin dynamics in a QD system, with the surrounding material having more of a bearing on the PLE emission. As a result, it was decided to insert a structure (in this case a QW) into the excitation region, with a resonance within the excitation wavelength range, varying the distance between the QW and the QDs.

5.3.4 *Coupled QD/QW Samples*

300Å GaAs
500Å 35% AlGaAs
410Å GaAs
40Å Low Temperature GaAs Cap
2.4 ML InAs QDs
z Å GaAs Spacer
80Å 4% InGaAs QW
250Å GaAs
500Å 35% AlGaAs
2000Å GaAs Buffer
GaAs Substrate

Figure 5.3.10: Structure of “coupled QD/QW” sample set, with each sample’s QD/QW separation varying by z nanometres.

The last sample set measured in this experiment is described in figure 5.3.10, with optically active regions containing both a quantum well and quantum dot. The variance between these samples is the distance between the confined structures, z , where $z = 3$ nm, 6 nm, 9 nm, 12 nm and 20 nm. The 4% InGaAs composition of the QW was decided upon as its emission wavelength at low temperature (~ 10 K) is within the excitation range of the PLE set up, at 830 nm. These samples were grown prior to initial PLE analysis, therefore the potential overlap of the QW with the WL LH states was not anticipated. The decreasing distance between the QW and QDs should enhance excitation transfer between the two, with spacer values below 10 nm expected to show coupling of the QD and QW, with Heitz et al stating that the efficiency of carrier transfer between two coupled quantum structures increases exponentially as the distance decreases [26].

Figure 5.3.11 shows the spin PLE data from samples described in figure 5.3.10. What is immediately obvious is increased variation of emission and polarisation between samples compared with previous spin PLE sets. Similar to what has been seen in other samples, there is a similarity between the polarisation from the GaAs bulk and HH, with a small peak representing what is assumed to be an AlGaAs shallow state at 803 nm, and a subsequent peak at 817 nm representing the GaAs band-edge exciton. There is a reduc-

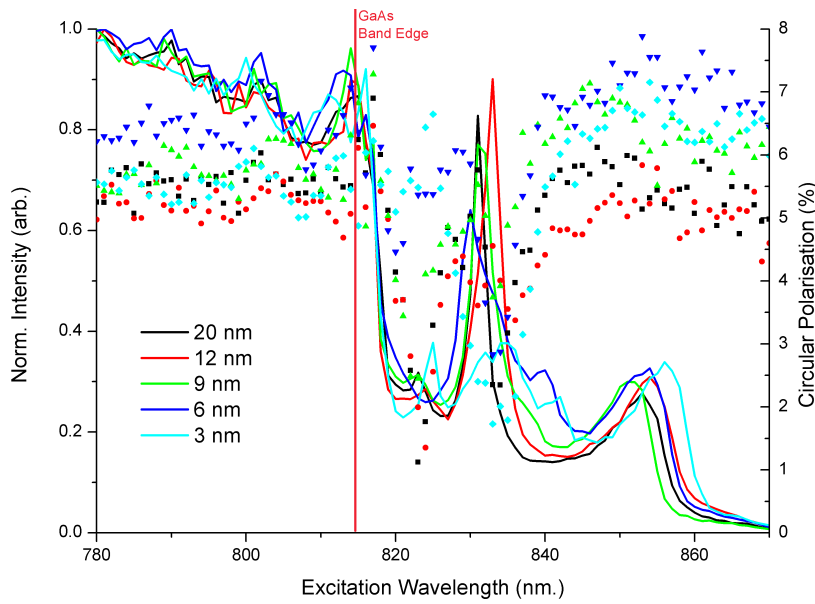


Figure 5.3.11: Coupled QD/QW sample set PLE data. Samples described in figure 5.3.10. Solid line plot represents the normalised intensity of the PLE for each sample (left axis), with the scatter plot representing the polarisation value of the emission at the corresponding excitation wavelength (right axis).

tion in polarisation, but it appears that there is an overlap between the LH state of the WL and the 4% InGaAs QW in the structure, which, when excited, nullifies the effect of the LH state having little to no polarisation. As the distance between the QW and QDs decreases, the effect of coupling is apparent, with the QW's intensity peak broadening, and the polarisation showing an increase and variation with respect to the excitation wavelength.

In order to try and clean the overall image up, as well as to properly define features in the PLE, it was decided to average the plots, as shown in figure 5.3.12. This allows better definition of the intensity peaks- with further confirmation across the samples that there is a peak in both intensity and polarisation at 803 nm, followed by a clearly defined GaAs band-edge exciton peak at 817 nm (again both in polarisation and intensity). This goes to show the influence of AlGaAs barriers on either side of the active region, at a reduced distance compared to the In-flush samples, but at a larger distance compared to the In-coverage and previous GaAs capped sample. This data also seems to confirm that more GaAs in the region constrained by the AlGaAs barriers produces more intense QD emission when exciting above the GaAs band-edge. The difference between this and previous

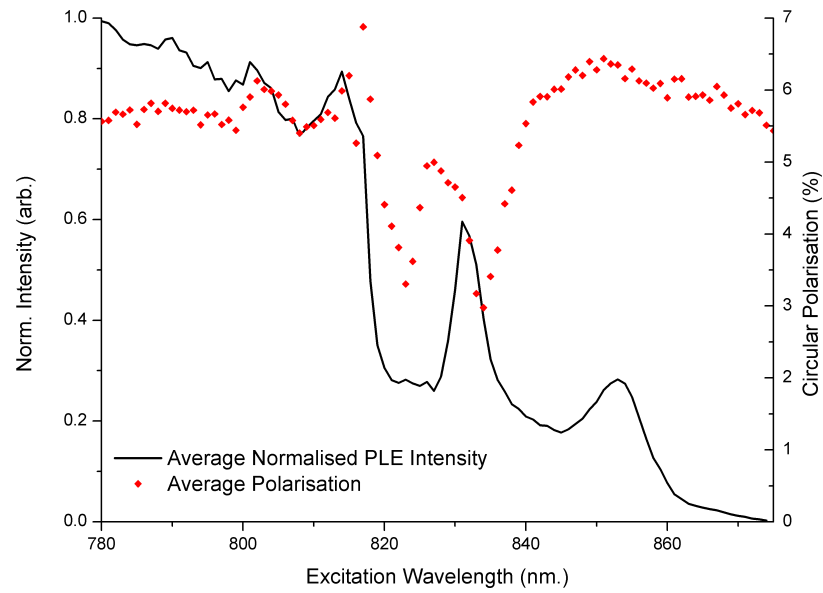


Figure 5.3.12: Plot showing the averaged normalised PLE intensity and the averaged polarisation.

samples is primarily caused by the overlap of the QW and LH peak. The averaged data shows that this confused peak is broadened, with the polarisation varying from sample to sample, meaning that the averaged sample struggles to provide an overview as it has done in previous sample sets. The QW in the structure overlaps with the LH peak, with the polarisation appearing to drop either side of the QW peak, but having an increase that coincides with the comparatively more intense QW peak. The HH peak at ~ 855 nm remains similar to previous samples, with the behaviour rather more uniform, and the trend able to be sufficiently described by the averaged data. The variation in the data at the LH/QW energy needs further analysis. As a result, each sample's plot will be compared with the average data. The intensity values for each are normalised to the maximum intensity above the GaAs band-edge.

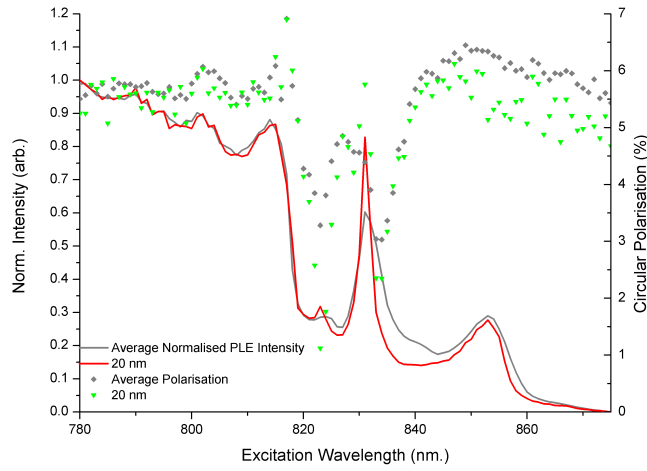


Figure 5.3.13: Averaged PLE data compared to 20 nm spaced QW/QD sample

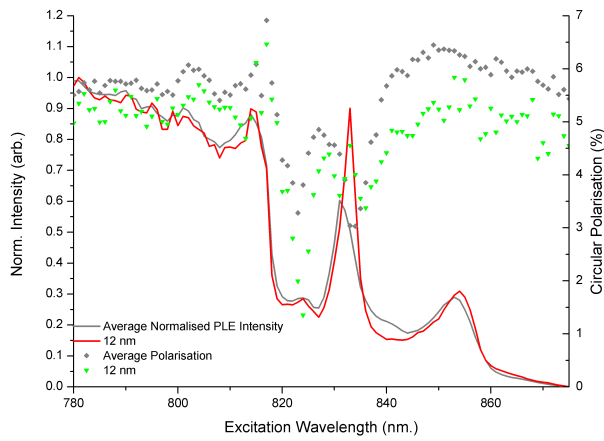


Figure 5.3.14: Averaged PLE data compared to 12 nm spaced QW/QD sample

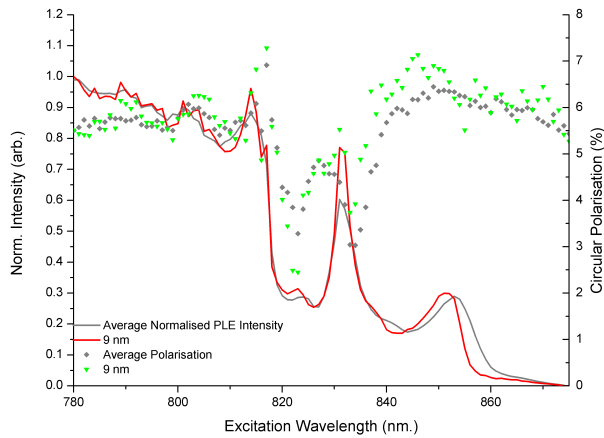


Figure 5.3.15: Averaged PLE data compared to 9 nm spaced QW/QD sample

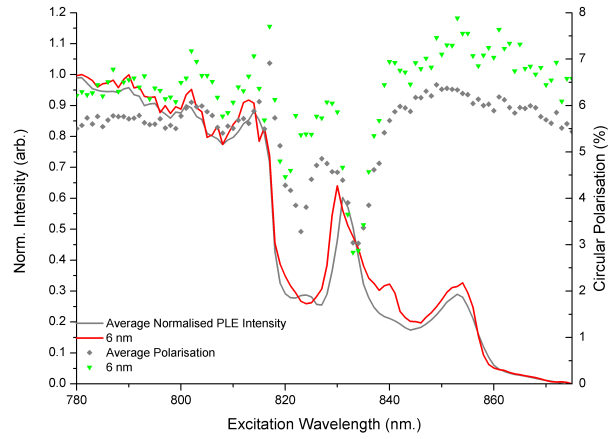


Figure 5.3.16: Averaged PLE data compared to 6 nm spaced QW/QD sample

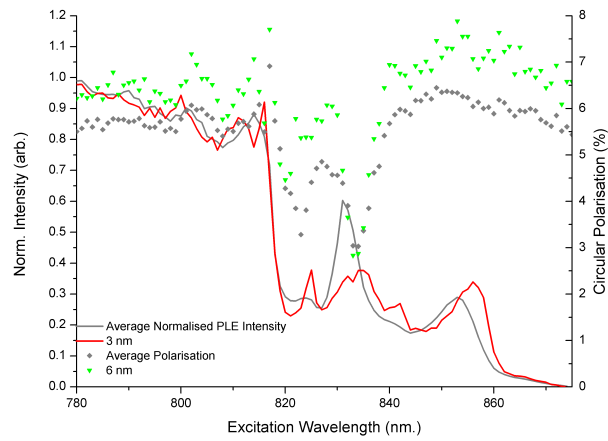


Figure 5.3.17: Averaged PLE data compared to 3 nm spaced QW/QD sample

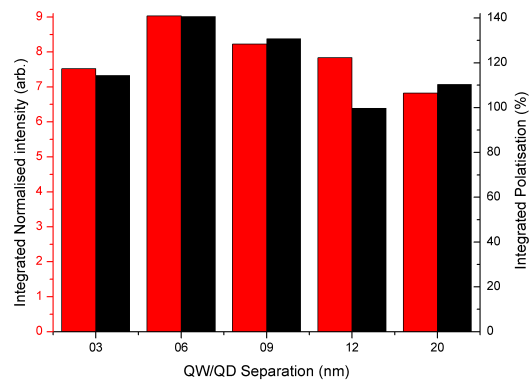


Figure 5.3.18: Chart describing the integrated normalised intensity (red, left axis) and integrated polarisation over the QW/LH excitation range, from 820 nm to 845 nm in an attempt to quantify the change from sample to sample.

Noting the progression through the samples, there is a number of constant features, such as the intensity and polarisation peaks at 803 nm (AlGaAs localised state), 817 nm (GaAs band-edge exciton) and at approximately 855 nm (HH), the main difference between each figure is the behaviour of the LH/QW states. This corroborates with the statement made previously, in that the intensity behaviour of the QD and WL appear to be constant from sample to sample, the main difference comes when changing external material, be it the amount of GaAs in the confined region, the proximity of AlGaAs barriers or, in this case, the introduction of a QW.

If we start with the 20 nm separation sample in figure 5.3.13, there is a small peak in intensity coinciding with a drop in polarisation at 822 nm- potentially indicating the presence of a LH state. The large sharp intensity peak at 831 nm represents the QW, with a corresponding increase in polarisation, which would not occur if this was a LH state. If this experiment were performed at a higher temperature, one would assume that the intensity of the QW peak is indicative of the QW acting as an uncoupled carrier reservoir, with its confining potential being particularly small, thus allowing relatively easy carrier escape and recapture between the QW and QDs. Due to the lack of thermal energy of the carriers at 10 K, it is highly unlikely that this is the case, even if the difference in energy is small ($\Delta E(E_g^{GaAs} - E_{QW}) = 26$ meV). The reason for the sharp peak in intensity at this point is assumed to be down to a resonance between the QW and the LH state of the WL, with the QW significantly affecting the behaviour of the polarisation compared to the LH, which would usually reduce the polarisation. The overall polarisation is slightly below the average in this sample, with the integrated well and PL intensity in the LH/QW region proving to be below the average value as well, despite the intensity peak large.

The 12 nm separation sample in figure 5.3.14 shows an increase in the width and height of the QW peak, with a decrease in height, but increase in width. The polarisation drops overall in comparison to the previous sample, as is shown with the integrated plot in figure 5.3.18. The widening of the QW peak may signify the beginning of coupling to the QDs in the structure, the reasoning behind the drop in polarisation is uncertain. Even with light

coupling, it remains uncertain why the intensity at the resonance of the QW is so strong.

The 9 nm separation sample (figure 5.3.15) shows a decrease and broadening in the QW peak, but an overall increase in the intensity, as is shown by the integrated normalised intensity in figure 5.3.18. A small peak coinciding with a drop in polarisation remains on the left hand side of the QW peak, indicating the presence of the LH, although the drop in polarisation isn't as pronounced, and both the overall intensity and polarisation has in fact increased, as per the integrated intensity plot in figure 5.3.18.

The 6 nm separation sample is described in figure 5.3.16, and shows an overall increase in polarisation and intensity, potentially showing this as the most efficient coupling of the QW and QD. The peak due to the QW is very distorted in the 6 nm sample, extremely broad and with a lower intensity compared with the 9 nm separation sample, with an apparent lack of LH peak or drop in polarisation. There is a drop in polarisation on the right-hand-side of the low-energy peak, maybe showing a curious coalescence of the LH and QW peaks. A hitherto unseen peak emerges at 840 nm, with a small bump in polarisation to match: the reason behind this is uncertain, beyond an effect of the LH and QW states being resonant. As the energy of the QW is resonant with the WL, it may be that the WL is coupling not with the QDs, but instead with the WL. The efficiency of this process is uncertain, although polarisation does not drop to zero at the LH energy as with previous samples, suggesting that the inclusion of a QW at this energy helps retain more spin across the measured range.

The 3 nm separation sample (figure 5.3.17) shows an apparent suppression of the QW peak, with a number of small, broad peaks in its stead. The drop in polarisation attributed to the LH matches the previous sample at around 832 nm, with the broadest of the new peaks coinciding with this drop. A peak otherwise assumed to be the LH in terms of wavelength shows no corresponding dip in polarisation at 827 nm. The peak at 840 nm seen in the 6 nm sample reappears, with a similar jump in polarisation. The integrated values for this sample shows an overall drop in both polarisation and intensity, potentially showing a reduction in the efficiency of the coupling in

this particular sample, the maximum otherwise reached in the sample with 6 nm separation.

Figure 5.3.18 shows the integrated PLE intensity and polarisation over the range of excitation of the QW. Looking at the PLE intensity, the quantum well reduces in intensity, and broadens its peak as its proximity to the QDs increases. This is potentially due to an increase in tunnelling rate, which would imply an increase in the coupling between the QW and QDs (or WL), with the wavefunction decaying from the QW to QD, but not going to zero in between the two- hence the overall increase in intensity when looking at the integrated values. Looking at the 20 nm and 12 nm samples, it would seem that the QW is acting rather as a carrier reservoir instead of coupling with the QDs- a strong, narrow, almost-Lorentzian peak in the PLE, with it the carriers appearing to find their way to the QDs, potentially due to resonance with the LH state in the WL. The reduction in efficiency, both in polarisation and intensity, when the QW/QD separation is at 3 nm may be due to hybridisation of the QW/QD states.

In an attempt to better describe the QW and WL, long exposure PL was taken across the excitation range of the PLE, with a fixed excitation wavelength. The reason for the long exposure is the comparative lack of emission from the QW and WL, with the majority of optical emission happening at the QDs. This shows that carrier transfer between the QW and QDs is efficient, and in the direction of the QDs. Figure 5.3.19 shows a lack of variation across the range of samples in terms of wavelength or FWHM, with the intensity varying slightly. This shows that the well and wetting layer are both consistent in terms of composition and size in each sample.

Figures 5.3.20 and 5.3.21 show the same data normalised to the peak of the QW and WL respectively. This was to confirm that both the WL and QW behaved in a similar manner throughout the sample set. The two extreme samples (20 nm and 3 nm) appear to have slight variation, but are still broadly similar, with each showing slight variation.

This sample set confirmed observations in previous samples, that the major effects on spin in QD samples is primarily external. This is logical given the extremely short capture time in QDs- spin loss occurs primarily between excitation and capture of carriers.

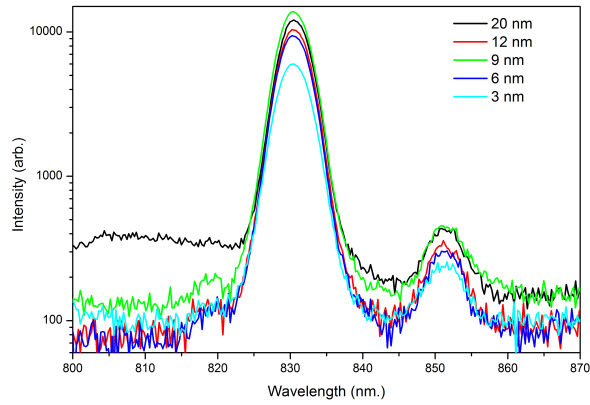


Figure 5.3.19: Long exposure PL showing WL and QW of coupled samples

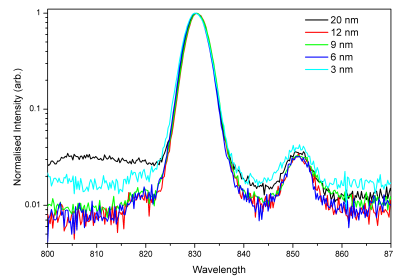


Figure 5.3.20: Figure 5.3.19 normalised to the QW emission

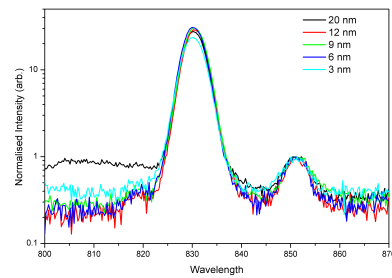


Figure 5.3.21: Figure 5.3.19 normalised to the WL emission

5.4 Conclusion

The PLE analysis appears to have determined that the spin retention within an optical device is not dependent on the dot size when injecting at the GaAs bulk and WL levels. Instead, the primary effect appears to be due to external structures and their proximity to the QDs, either AlGaAs barriers or InGaAs QWs. Indeed, varying the indium levels in two different ways did not seem to significantly alter the spin retention from sample to sample- the main difference between the In-flush and In-coverage samples was the comparative intensity when injecting the WL and GaAs bulk, which is thought to be an effect of the AlGaAs barriers and the comparative amount and order of GaAs in the active region. A lack of “upper” AlGaAs barriers in the In-flush samples appear to have yielded a higher overall spin retention than the other samples, all of which had AlGaAs surrounding the active region: this needs further work to confirm.

Each sample set bar the In-flush set presents evidence of an intensity and polarisation peak above the GaAs band-edge exciton, particularly in the samples with a smaller GaAs proportion in the active region. The reason for the assumption that this peak is related to the surrounding AlGaAs is based on the fact that it is above the GaAs band-edge, and the similar energy differences compared to the AlGaAs barrier energy (table 5.4.1).

Sample Set	AlGaAs Comp ⁿ	E _g (AlGaAs)	Unknown State Energy	AlGaAs/State Energy Difference	GaAs/State Energy Difference
Standard Samples	0.31	1911	1536	375	18
In Coverage Samples	0.31	1911	1544	367	26
Coupled Samples	0.35	1967	1550	417	32

Table 5.4.1: Table comparing the unknown state energy to the GaAs and AlGaAs band gap energy.

There is no evidence that the DX centre is involved, with papers [31–33] discussing DX centres listing associated transition energies that have different levels compared to that measured in our samples- with ours measuring ~ 370 meV and ~ 410 meV, the literature lists values both above and below. The 30 nm of GaAs between AlGaAs barriers has also been dismissed as being a QW, with QW solvers showing an energy with an almost infinitesimally small energy difference compared to GaAs bulk at the same temperature- 1.5193 eV compared with 1.5173 eV for bulk GaAs at 25 K. The temperature of the samples was assumed to be offset from the temperature as measured by the cryostat due to the energy value of the GaAs bandedge. Process of elimination has led to the attribution of this unknown energy state to a localised state in the AlGaAs, given that the polarisation appears to increase, similar to the uncoupled QW seen in the QW/QD samples. Given that the QWs act as a source of localised carriers within the active region, this statement is not without reason, especially as the polarisation appears to behave in a similar manner. That being said, clearly more research needs to be done to properly determine the source of this absorption peak.

The apparent lack of spin retention when injecting into an energy that is resonant with the HH of the WL is an unusual result that has emerged from this experiment, and appears to be consistent across the entire range of samples. The reasoning behind this is uncertain, and needs further investigation, perhaps with a view to modelling the carrier dynamics in a QD system, something already of interest.

The “coupled” sample set appear to show an overlapping of the QW and WL states, with the QW appearing to absorb at the same energy as the LH. This could be further investigated by growing similar samples including a QW with a deeper confining potential. This could cause the behaviour of carriers to change in the samples with a larger separation, given that the shallow 4% InGaAs wells appeared to act as a carrier reservoir, due to its resonance with the WL LH state. It is also unclear as to whether the behaviour of the carriers would change in the coupled, closer QW/QD structures would change with a deeper QW, particularly if the QW was resonant with the QDs. The main aspect of this part of the experiment that needs to be cleared up is the behaviour of the QW as the proximity changes, which is made difficult in this case due to the QW’s energy lying in the same area as the WL. Ideally, clear energetic separation of the two would allow analysis of both the polarisation and PLE intensity for each feature.

In essence, this work has shown that undoped QDs yield spin polarised light using a continuous wave σ^+ light source indicating a comparative spin and luminescence lifetime, with further investigation needed into the effect of material composition in the structure surrounding QDs.

5.5 References

- [1] G. Narvaez and A. Zunger, "Nominally forbidden transitions in the interband optical spectrum of quantum dots," *Physical Review B*, vol. 74, no. 4, p. 045316, Jul. 2006. [Online]. Available: <http://link.aps.org/doi/10.1103/PhysRevB.74.045316>
- [2] J. Dreiser, M. Atatüre, C. Galland, T. Müller, A. Badolato, and A. Imamoglu, "Optical investigations of quantum dot spin dynamics as a function of external electric and magnetic fields," *Physical Review B*, vol. 77, no. 7, p. 075317, Feb. 2008. [Online]. Available: <http://link.aps.org/doi/10.1103/PhysRevB.77.075317>
- [3] X. Xu, Y. Wu, B. Q. Sun, Q. Huang, J. Cheng, D. G. Steel, A. S. Bracker, D. Gammon, C. Emary, and L. J. Sham, "Fast Spin State Initialization in a Singly Charged InAs-GaAs Quantum Dot by Optical Cooling," *Physical Review Letters*, vol. 99, no. 9, p. 097401, Aug. 2007. [Online]. Available: <http://link.aps.org/doi/10.1103/PhysRevLett.99.097401>
- [4] M. Paillard, X. Marie, P. Renucci, T. Amand, A. Jbeli, and J. M. Gérard, "Spin Relaxation Quenching in Semiconductor Quantum Dots," *Physical Review Letters*, vol. 86, no. 8, pp. 1634–1637, Feb. 2001. [Online]. Available: <http://link.aps.org/doi/10.1103/PhysRevLett.86.1634>
- [5] K. Gündoğdu, K. C. Hall, T. F. Boggess, D. G. Deppe, and O. B. Shchekin, "Efficient electron spin detection with positively charged quantum dots," *Applied Physics Letters*, vol. 84, no. 15, p. 2793, 2004. [Online]. Available: <http://scitation.aip.org/content/aip/journal/apl/84/15/10.1063/1.1695637>
- [6] Y. D. Jang, T. J. Badcock, D. J. Mowbray, M. S. Skolnick, J. Park, D. Lee, H. Y. Liu, M. Hopkinson, R. A. Hogg, and A. D. Andreev, "Enhanced nonradiative Auger recombination in p-type modulation doped InAs/GaAs quantum dots," *Applied Physics Letters*, vol. 93, no. 10, p. 101903, 2008. [Online]. Available: <http://scitation.aip.org/content/aip/journal/apl/93/10/10.1063/1.2975961>

- [7] J. Siegert, S. Marcinkevičius, and Q. X. Zhao, "Carrier dynamics in modulation-doped InAs/GaAs quantum dots," *Physical Review B*, vol. 72, no. 8, p. 085316, Aug. 2005. [Online]. Available: <http://link.aps.org/doi/10.1103/PhysRevB.72.085316>
- [8] X. M. Wen, L. V. Dao, J. A. Davis, P. Hannaford, S. Mokkaḡpati, H. H. Tan, and C. Jagadish, "Carrier dynamics in p-type InGaAs/GaAs quantum dots," *Journal of Materials Science: Materials in Electronics*, vol. 18, no. S1, pp. 363–365, Apr. 2007. [Online]. Available: <http://link.springer.com/10.1007/s10854-007-9241-5>
- [9] K. Gündođdu, K. C. Hall, T. F. Boggess, D. G. Deppe, and O. B. Shchekin, "Ultrafast electron capture into p-modulation-doped quantum dots," *Applied Physics Letters*, vol. 85, no. 20, p. 4570, 2004. [Online]. Available: <http://scitation.aip.org/content/aip/journal/apl/85/20/10.1063/1.1815371>
- [10] K. Gündođdu, K. C. Hall, E. J. Koerperick, C. E. Pryor, M. E. Flatté, T. F. Boggess, O. B. Shchekin, and D. G. Deppe, "Electron and hole spin dynamics in semiconductor quantum dots," *Applied Physics Letters*, vol. 86, no. 11, p. 113111, 2005. [Online]. Available: <http://scitation.aip.org/content/aip/journal/apl/86/11/10.1063/1.1857067>
- [11] S. Marcinkevičius, J. Siegert, and Q. X. Zhao, "Carrier spin dynamics in modulation-doped InAs/GaAs quantum dots," *Journal of Applied Physics*, vol. 100, no. 5, p. 054310, 2006. [Online]. Available: <http://scitation.aip.org/content/aip/journal/jap/100/5/10.1063/1.2337776>
- [12] J. M. Elzerman, R. Hanson, L. van Beveren, B. Witkamp, L. Vandersypen, and L. P. Kouwenhoven, "Single-shot read-out of an individual electron spin in a quantum dot," *Nature*, vol. 430, no. 6998, pp. 431–435, 2004. [Online]. Available: <http://gateway.webofknowledge.com/gateway/Gateway.cgi?GWVersion=2&SrcAuth=mekentosj&SrcApp=Papers&DestLinkType=FullRecord&DestApp=WOS&KeyUT=000222801400036>
- [13] A. Khaetskii, D. Loss, and L. Glazman, "Electron Spin Decoherence in Quantum Dots due to Interaction with Nuclei," *Physical Review*

- Letters*, vol. 88, no. 18, p. 186802, Apr. 2002. [Online]. Available: <http://link.aps.org/doi/10.1103/PhysRevLett.88.186802>
- [14] M. Kroutvar, Y. Ducommun, D. Heiss, M. Bichler, D. Schuh, G. Abstreiter, and J. J. Finley, "Optically programmable electron spin memory using semiconductor quantum dots," *Nature*, vol. 432, no. 7013, pp. 81–84, 2004. [Online]. Available: <http://gateway.webofknowledge.com/gateway/Gateway.cgi?GWVersion=2&SrcAuth=mekentosj&SrcApp=Papers&DestLinkType=FullRecord&DestApp=WOS&KeyUT=000224854900042>
- [15] S. Cortez, O. Krebs, P. Voisin, and J. M. Gérard, "Polarization of the interband optical dipole in InAs/GaAs self-organized quantum dots," *Physical Review B*, vol. 63, no. 23, p. 233306, May 2001. [Online]. Available: <http://link.aps.org/doi/10.1103/PhysRevB.63.233306>
- [16] S. Alaya, H. Maaref, and J. C. Bourgoin, "Luminescence of the DX center in AlGaAs," *Applied Physics Letters*, vol. 55, no. 14, p. 1406, 1989. [Online]. Available: <http://scitation.aip.org/content/aip/journal/apl/55/14/10.1063/1.101608>
- [17] D. Heiss, S. Schaeck, H. Huebl, M. Bichler, G. Abstreiter, J. J. Finley, D. Bulaev, and D. Loss, "Observation of extremely slow hole spin relaxation in self-assembled quantum dots," *Physical Review B*, vol. 76, no. 24, p. 241306, Dec. 2007. [Online]. Available: <http://link.aps.org/doi/10.1103/PhysRevB.76.241306>
- [18] E. Harbord, P. Spencer, E. M. Clarke, and R. Murray, "Radiative lifetimes in undoped and p-doped InAs/GaAs quantum dots," *Physical Review B*, vol. 80, no. 19, p. 195312, Nov. 2009. [Online]. Available: <http://link.aps.org/doi/10.1103/PhysRevB.80.195312>
- [19] O. Wolst, M. Schardt, M. Kahl, S. Malzer, and G. H. Döhler, "A combined investigation of lateral and vertical Stark effect in InAs self-assembled quantum dots in waveguide structures," *Physica E-Low-Dimensional Systems & Nanostructures*, vol. 13, no. 2, pp.

- 283–288, 2002. [Online]. Available: <http://www.sciencedirect.com/science/article/pii/S1386947701005380>
- [20] C. E. Pryor and M. E. Flatté, “Accuracy of Circular Polarization as a Measure of Spin Polarization in Quantum Dot Qubits,” *Physical Review Letters*, vol. 91, no. 25, p. 257901, Dec. 2003. [Online]. Available: <http://link.aps.org/doi/10.1103/PhysRevLett.91.257901>
- [21] C. Weisbuch and B. Vinter, *Quantum Semiconductor Structures*, ser. Fundamentals and Applications. Elsevier, 1991. [Online]. Available: http://books.google.co.uk/books?id=iCgWvw5ZpRQC&printsec=frontcover&dq=quantum+semiconductor+structures&hl=&cd=1&source=gbs_api
- [22] J. H. Lee, K. Y. Hsieh, and R. M. Kolbas, “Photoluminescence and stimulated emission from monolayer-thick pseudomorphic InAs single-quantum-well heterostructures,” *Physical Review B*, vol. 41, no. 11, p. 7678, 1990. [Online]. Available: <http://journals.aps.org/prb/abstract/10.1103/PhysRevB.41.7678>
- [23] E. Y. Tsymlal and I. Zutic, *Handbook of Spin Transport and Magnetism*. CRC Press, Aug. 2011. [Online]. Available: http://books.google.co.uk/books?id=MtNjrpcZ-iwC&printsec=frontcover&dq=handbook+of+spin+transport+and+magnetism&hl=&cd=1&source=gbs_api
- [24] X. M. Dou, B. Q. Sun, Y. H. Xiong, Z. C. Niu, H. Q. Ni, and Z. Y. Xu, “Fine structural splitting and exciton spin relaxation in single InAs quantum dots,” *Journal of Applied Physics*, vol. 105, no. 10, 2009. [Online]. Available: <http://gateway.webofknowledge.com/gateway/Gateway.cgi?GWVersion=2&SrcAuth=mekentosj&SrcApp=Papers&DestLinkType=FullRecord&DestApp=WOS&KeyUT=000266500100085>
- [25] Q. H. Xie, A. Madhukar, P. Chen, and N. P. Kobayashi, “Vertically Self-Organized InAs Quantum Box Islands on GaAs(100),” *Physical Review Letters*, vol. 75, no. 13, pp. 2542–2545, 1995. [Online]. Available: <http://gateway.webofknowledge.com/gateway/Gateway.cgi?GWVersion=2&SrcAuth=mekentosj&SrcApp=>

- Papers&DestLinkType=FullRecord&DestApp=WOS&KeyUT=A1995RV95000023
- [26] R. Heitz, A. Kalburge, Q. Xie, M. Grundmann, P. Chen, A. Hoffmann, A. Madhukar, and D. Bimberg, "Excited states and energy relaxation in stacked InAs/GaAs quantum dots," *Physical Review B*, vol. 57, no. 15, p. 9050, 1998. [Online]. Available: <http://journals.aps.org/prb/abstract/10.1103/PhysRevB.57.9050>
- [27] B. Lita, R. S. Goldman, J. D. Phillips, and P. K. Bhattacharya, "Nanometer-scale studies of vertical organization and evolution of stacked self-assembled InAs/GaAs quantum dots," *Applied Physics Letters*, vol. 74, no. 19, p. 2824, 1999. [Online]. Available: <http://scitation.aip.org/content/aip/journal/apl/74/19/10.1063/1.124026>
- [28] D. M. Bruls, P. M. Koenraad, H. W. M. Salemink, J. H. Wolter, M. Hopkinson, and M. S. Skolnick, "Stacked low-growth-rate InAs quantum dots studied at the atomic level by cross-sectional scanning tunneling microscopy," *Applied Physics Letters*, vol. 82, no. 21, p. 3758, 2003. [Online]. Available: <http://scitation.aip.org/content/aip/journal/apl/82/21/10.1063/1.1578709>
- [29] E. M. Clarke, E. Harbord, and R. Murray, "Carrier spin dynamics in self-assembled quantum dots," in *Optical Generation and Control of Quantum Coherence in Semiconductor Nanostructures*, G. Slavcheva and P. Roussignol, Eds. Springer Berlin Heidelberg, Jan. 2010, pp. 39–61. [Online]. Available: http://link.springer.com/chapter/10.1007/978-3-642-12491-4_4
- [30] M. Bayer, G. Ortner, O. Stern, A. Kuther, A. Gorbunov, A. Forchel, P. Hawrylak, S. Fafard, K. Hinzer, T. L. Reinecke, S. N. Walck, J. P. Reithmaier, F. Klopff, and F. Schäfer, "Fine structure of neutral and charged excitons in self-assembled In(Ga)As/(Al)GaAs quantum dots," *Physical Review B*, vol. 65, no. 19, p. 195315, May 2002. [Online]. Available: <http://link.aps.org/doi/10.1103/PhysRevB.65.195315>
- [31] P. M. Mooney, N. S. Caswell, and S. L. Wright, "The capture barrier of the DX center in Si-doped Al_xGa_{1-x}As," *Journal of Applied Physics*,

- vol. 62, no. 12, p. 4786, 1987. [Online]. Available: <http://scitation.aip.org/content/aip/journal/jap/62/12/10.1063/1.338981>
- [32] O. Kumagai, H. Kawai, Y. Mori, and K. Kaneko, "Chemical trends in the activation energies of DX centers," *Applied Physics Letters*, vol. 45, no. 12, p. 1322, 1984. [Online]. Available: <http://scitation.aip.org/content/aip/journal/apl/45/12/10.1063/1.95135>
- [33] P. M. Mooney, "Deep donor levels (DX centers) in III-V semiconductors," *Journal of Applied Physics*, vol. 67, no. 3, p. R1, 1990. [Online]. Available: <http://scitation.aip.org/content/aip/journal/jap/67/3/10.1063/1.345628>
- [34] G. Itskos, E. Harbord, S. K. Clowes, E. M. Clarke, L. F. Cohen, R. Murray, P. Van Dorpe, and W. Van Roy, "Oblique Hanle measurements of InAs/GaAs quantum dot spin-light emitting diodes," *Applied Physics Letters*, vol. 88, no. 2, p. 022113, 2006. [Online]. Available: <http://scitation.aip.org/content/aip/journal/apl/88/2/10.1063/1.2163074>
- [35] H. Gotoh, H. Ando, H. Kamada, A. Chavez-Pirson, and J. Temmyo, "Spin relaxation of excitons in zero-dimensional InGaAs quantum disks," *Applied Physics Letters*, vol. 72, no. 11, p. 1341, 1998. [Online]. Available: <http://scitation.aip.org/content/aip/journal/apl/72/11/10.1063/1.120988>
- [36] A. Tackeuchi, R. Ohtsubo, K. Yamaguchi, M. Murayama, T. Kitamura, T. Kuroda, and T. Takagahara, "Spin relaxation dynamics in highly uniform InAs quantum dots," *Applied Physics Letters*, vol. 84, no. 18, p. 3576, 2004. [Online]. Available: <http://scitation.aip.org/content/aip/journal/apl/84/18/10.1063/1.1737068>
- [37] R. J. Epstein, D. T. Fuchs, W. V. Schoenfeld, P. M. Petroff, and D. D. Awschalom, "Hanle effect measurements of spin lifetimes in InAs self-assembled quantum dots," *Applied Physics Letters*, vol. 78, no. 6, p. 733, 2001. [Online]. Available: <http://scitation.aip.org/content/aip/journal/apl/78/6/10.1063/1.1344565>

- [38] P. D. Sivers, S. Malik, G. McPherson, D. Childs, C. Roberts, R. Murray, and B. A. Joyce, "Scanning transmission-electron microscopy study of InAs/GaAs quantum dots," *Physical Review B*, vol. 58, no. 16, pp. 10 127–10 130, 1998. [Online]. Available: <http://journals.aps.org/prb/abstract/10.1103/PhysRevB.58.R10127>
- [39] M. W. Taylor, P. Spencer, E. M. Clarke, E. Harbord, and R. Murray, "Resolving Zeeman splitting in quantum dot ensembles," *Applied Physics Letters*, vol. 102, no. 17, p. 171909, 2013. [Online]. Available: <http://scitation.aip.org/content/aip/journal/apl/102/17/10.1063/1.4804267>
- [40] J. M. Gérard and J. Y. Marzin, "High quality ultrathin InAs/GaAs quantum wells grown by standard and low-temperature modulated-fluxes molecular beam epitaxy," *Applied Physics Letters*, vol. 53, no. 7, p. 568, 1988. [Online]. Available: <http://scitation.aip.org/content/aip/journal/apl/53/7/10.1063/1.99859>
- [41] I. Mukhametzhonov, R. Heitz, J. Zeng, P. Chen, and A. Madhukar, "Independent manipulation of density and size of stress-driven self-assembled quantum dots," *Applied Physics Letters*, vol. 73, no. 13, p. 1841, 1998. [Online]. Available: <http://scitation.aip.org/content/aip/journal/apl/73/13/10.1063/1.122300>
- [42] S. Tomic, P. Howe, N. M. Harrison, and T. S. Jones, "Theoretical analysis of strain and strain decay in InAs/GaAs(001) multilayer quantum dot growth," *Journal of Applied Physics*, vol. 99, no. 9, p. 093522, 2006. [Online]. Available: <http://scitation.aip.org/content/aip/journal/jap/99/9/10.1063/1.2190028>
- [43] P. Howe, "Competition between strain-induced and temperature-controlled nucleation of InAs/GaAs quantum dots," *Journal of Applied Physics*, vol. 95, no. 6, p. 2998, 2004. [Online]. Available: <http://scitation.aip.org/content/aip/journal/jap/95/6/10.1063/1.1645637>
- [44] S. Adachi, *Properties of Aluminium Gallium Arsenide*. IET, Jan. 1993. [Online]. Available: <http://books.google.co.uk/books?id=>

s7icD_5b670C&printsec=frontcover&dq=Properties+of+Aluminium+Gallium+Arsenide&hl=&cd=1&source=gbp_api

- [45] E. Ribeiro, F. Cerdeira, M. J. S. P. Brasil, T. Heinzl, K. Ensslin, G. Medeiros-Ribeiro, and P. M. Petroff, "An optical study of self-assembled In_xGa_{1-x}As/GaAs quantum dots embedded in a two-dimensional electron gas," *Journal of Applied Physics*, vol. 87, no. 11, p. 7994, 2000. [Online]. Available: <http://scitation.aip.org/content/aip/journal/jap/87/11/10.1063/1.373485>
- [46] A. Minnaert, A. Silov, W. van der Vleuten, J. Haverkort, and J. H. Wolter, "Fröhlich interaction in InAs/GaAs self-assembled quantum dots," *Physical Review B*, vol. 63, no. 7, p. 075303, Jan. 2001. [Online]. Available: <http://link.aps.org/doi/10.1103/PhysRevB.63.075303>
- [47] A. Koudinov, I. Akimov, Y. Kusrayev, and F. Henneberger, "Optical and magnetic anisotropies of the hole states in Stranski-Krastanov quantum dots," *Physical Review B*, vol. 70, no. 24, p. 241305, Dec. 2004. [Online]. Available: <http://link.aps.org/doi/10.1103/PhysRevB.70.241305>

CONCLUSION

In this thesis, I have demonstrated growth and characterisation of III-V quantum dot structures. In chapter 2 I describe the practical methods used throughout this thesis, whereupon I detail the important aspects of MBE and the facilities available at the EPSRC National Centre for III-V Technologies.

In chapter 3, I have presented results from basic quantum dot growth, detailing the different growth techniques required to reach different wavelengths, plus the effect of external processing on the optical emission of QD structures. Demonstration of a range of emission wavelengths from 850 nm to 1300 nm at room temperature is shown, with the post growth anneal providing a method to improve the characteristics of poor QD samples. In particular, significant improvement of bimodal QDs was seen, reducing the population of QDs to one “family”, and the FWHM from ~ 115 nm to ~ 20 nm.

In chapter 4, I describe growth of low-density QD samples, with different methods of attaining low-density samples, and the dependence on growth rate being analysed. The applications of two variants of the low-density rotation-stop growth samples are described, with successful isolation of individual QDs for novel applications, including the analysis of FSS at telecoms wavelength. This work showed that the rotation stop method can successfully yield low-density quantum dots for a range of wavelengths, with three samples grown and analysed. Cambridge University demonstrate the resolving of individual QDs in a sample emitting at ~ 950 nm. Analysis done by this author shows a discrepancy in the assumptions when using a room temperature PL map, with comparisons between a PL map and AFM scans on a rotation-stop sample. Long-wavelength rotation stop QD samples were demonstrated, with initial results showing promise when analysed by

colleagues in Heriot Watt. Further samples of long-wavelength rotation stop QDs showed a considerable improvement in QD density grading across the wafer, showing a better ability to spatially isolate individual quantum dots. This will enable better analysis of individual longer wavelength QDs, and with this, potential improvement of the FSS in longer wavelength samples with a view to entangled telecom-wavelength emission.

Chapter 5 demonstrates the modification of an existing measurement to describe the spin loss mechanisms in optically active QD samples. The spin PLE measurements taken demonstrate that dots not tailor-made for spin applications still retain spin information, with a degree of polarisation up to 14 % detected. The efficiency of a coupled QW/QD system is also described, showing that there is a limit to the proximity of the QW, as a reduction in spin retention and emission intensity is seen in a sample with 3 nm separation between the two. The work done in this chapter shows that there is a link to the quality and type of material surrounding quantum dots and the spin retention, as opposed to the properties of the quantum dots themselves. The less material in the confining region between AlGaAs barriers, the less PLE intensity is seen when exciting above the GaAs band-edge, a result of the disordering of the GaAs by the high strain-field of the QDs. Similarly, the proximity of AlGaAs barriers to the QDs affects the PLE emission, with shallow states in the AlGaAs becoming evident in each sample with surrounding AlGaAs. This exhibits itself in the form of polarisation and intensity peaks above the GaAs band-edge, with the samples with less GaAs between the barriers showing a greater PLE intensity from this shallow AlGaAs state. The effect of a QW within the confining region is uncertain due to the samples used containing a QW resonant with the LH state in the WL. The QW did appear to increase the degree of polarisation of the emitted light, but the resonance with the LH made for confusing analysis. It did lend credence to the hypothesis of external material affecting the excitation of QDs, with the WL and GaAs bulk showing similar characteristics throughout this sample set.

6.1 Further Work

Chapter 3 describes a number of mature growth processes in the targeting of various wavelengths. However, the initial stages of the post-growth anneal appear to be relatively unexplored, particularly looking at the curing of the crystal and the effect of the strain field of QDs. Similarly, the transition from crystal curing to Fickian interdiffusion behaviour requires extra investigation and modelling.

Unfortunately the analysis of single long-wavelength QDs is time consuming, and although an improvement in the gradient of the QD density was seen in chapter 4, the analysis from colleagues at Heriot Watt remains outstanding. The properties of these QDs in a charge tunable structure with an increased strain-tuning range should hopefully yield promisingly low FSS values.

Regarding the spin PLE analysis from chapter 5, further work has been identified in a number of areas. In order to quantify the effect of InGaAs capping, an extended range PLE experiment could be used, applying similar polarisation analysis. The effects of the shallow state of nearby AlGaAs barriers could be investigated by both altering the composition of the barriers and the proximity in separate sample sets. This should confirm the origin of the assumed shallow state, and determine the optimal arrangement of barriers in such samples. As the QW-QD sample analysis was hampered by the QW being resonant with the WL LH state, an alternative QW composition would make for an ideal future experiment, with further spacial analysis required due to uncertainty regarding the reason behind the intensity of the PLE emission when exciting into the QW despite there being 20 nm of separation between the two structures. A further sample set investigating the effect of InGaAs composition of a coupled QW would enable analysis into the effect of the resonance with the WL state.

Part II

APPENDIX

APPENDIX:

POLARISATION OF IN-FLUSH QDS

Inspiration for the spin PLE experiment came from an experiment designed to determine the effect of cap heights on the edge-emission of QD samples. This experiment used the same In flush samples as were used in chapter 5 (see figure A.o.1), where $x = 2.5 \text{ nm}, 3 \text{ nm}, 3.5 \text{ nm}, 4.5 \text{ nm}$ and 5.3 nm

2.4ML InAs QDs
650Å GaAs
$y \text{ Å}$ Low Temperature Variable GaAs Cap
2.4ML InAs QDs
650Å GaAs
1000Å 35% AlGaAs
3000Å GaAs Buffer
GaAs Substrate

Figure A.o.1: In-flush sample structure

It was assumed that the change in cap height would alter the TE:TM ratio of the edge-emitted light, with light emitted from the side of QDs typically exhibiting stronger TE characteristics. This is due to the typical shape of quantum dots, assumed to be a lens shape, with a base up to 80 nm in diameter, and a capped height of up to 5 nm. Note that the latter value is influenced significantly by the capping material, with the value of 5 nm referring to QDs capped by GaAs. This ratio of base-width to height is approximately 16:1, increasing to 32:1 for the smallest cap height in the In flush sample set. With this in mind, it was assumed that there would be a

significant change in the TE:TM ratio when measuring the aforementioned samples.

The edge PL measurements were performed at 4K in a liquid helium-cooled cryostat. The small target area of the sample meant that a microscope lens was needed to focus the excitation source and emission. A polarimeter was employed to analyse the Stokes parameters of the light emission, in a similar manner to that of the spin PLE measurement, as mentioned in chapter 5.

This experiment was unfortunately limited by both time and resources, as the work was done at Imperial College's optics laboratory in London over the course of the week. The measurement itself was extremely difficult to master, as a result of focusing the excitation beam on the edge of the sample in question, with 3 days of measurements proven erroneous after misalignment. Misalignment caused the measurement to yield a TM-dominant emission as a result of reflected light from the sample edge, instead of just the emission from the QDs. The polarisation results showed identical polarisation measurements at their emission peak as a result (e.g. figure A.0.2).

The output of the polarisation PL measurement showed a plot of integrated intensity vs. polarisation angle, with the typical output being sinusoidal. This data was discarded after each run, and is therefore not displayed in this thesis. The display of this data after each run enabled proper alignment of later samples however, as it was discovered that position of the peaks and troughs of the sinusoid related to the correct focus on the sample. If the peaks (troughs) aligned with 45° (90°), then the sample was not focused correctly, and would yield a similar polarisation output to that seen in figure A.0.2.

Due to this misalignment, only two samples were measured successfully: the 2.5 nm and 5.3 nm capped samples. These samples were measured as having a maximum TE:TM ratio of 3.44:1 to 3.17:1 respectively. The ratio was calculated using the degree of polarisation (DOP) from the experimental results in figures A.0.3 and A.0.4 using $\text{DOP} (\%) = \frac{TE-TM}{TE+TM}$.

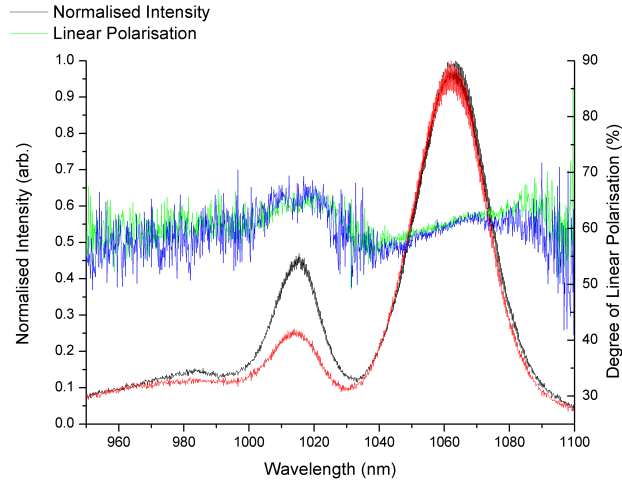


Figure A.o.2: Example of misaligned edge PL measurement.

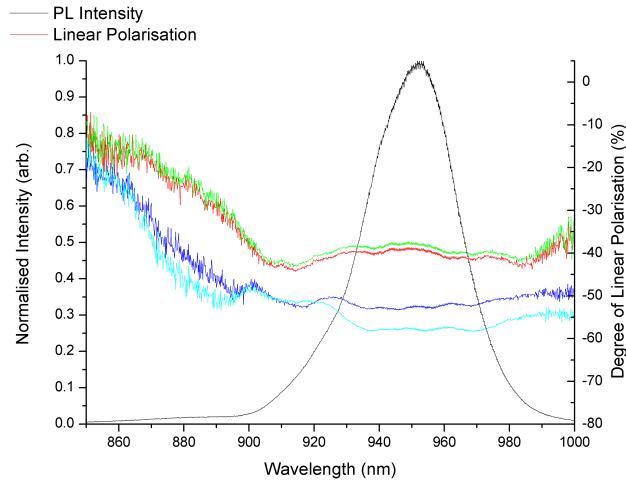


Figure A.o.3: Edge PL polarisation measurement from 2.5 nm capped sample.

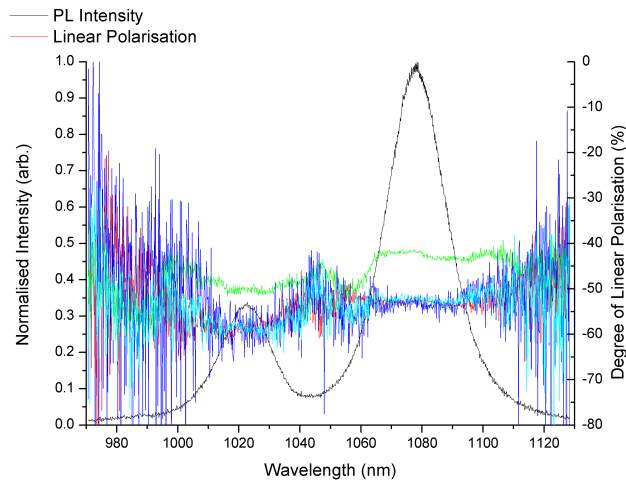


Figure A.o.4: Edge PL polarisation measurement from 5.3 nm capped sample.

Unfortunately, as can be seen from figures [A.0.3](#) and [A.0.4](#), the range of values attained from the measurement is not only similar, but wide, with the DOP ranging from $\sim 40\%$ to $\sim 55\%$ in both cases.

A.1 Conclusion

As a result of the wide range of error, and the small difference between the two samples, it is difficult to draw a definitive conclusion from these results. It is uncertain whether or not this is down to measurement error or variation between different points on the sample for each measurement, with further investigation needed, including an accurate and repeatable procedure for the edge PL measurement.